Progress towards arrays of qubits using diamond

by

Colin J. Stephen

Thesis

Submitted to the University of Warwick

for the degree of

Doctor of Philosophy

Department of Physics

July 2019

Contents

List of Figures

List of Tables

Publications

[1] Y. C. Chen, P. S. Salter, S. Knauer, L. Weng, A. C. Frangeskou, C. J. Stephen, S. N. Ishmael, P. R. Dolan, S. Johnson, B. L. Green, G. W. Morley, M. E. Newton, J. G. Rarity, M. J. Booth, and J. M. Smith, "Laser writing of coherent colour centres in diamond", Nat. Photonics **11**, 77–80 (2016).

[2] C. J. Stephen, B. L. Green, Y. N. D. Lekhai, L. Weng, P. Hill, S. Johnson, A. C. Frangeskou, P. L. Diggle, Y. C. Chen, M. J. Strain, E. Gu, M. E. Newton, J. M. Smith, P. S. Salter, and G. W. Morley, "Deep Three-Dimensional Solid-State Qubit Arrays with Long-Lived Spin Coherence", Phys. Rev. Appl. **12**, 064005 (2019).

[3] Y. C. Chen, B. Griffiths, L. Weng, S. S. Nicley, S. N. Ishmael, Y. N. D. Lekhai, S. Johnson, C. J. Stephen, B. L. Green, G. W. Morley, M. E. Newton, M. J. Booth, P. S. Salter, and J. M. Smith, "Laser writing of individual nitrogen-vacancy defects in diamond with near-unity yield", Optica **6**, 662 (2019).

Presentations

[1] C. Stephen, P. Salter, Y. Lekhai, B. L. Green, L. Weng, S. Johnson, P. Hill, M. Booth, E. Gu, J. Smith, and G. Morley, "Laser written three dimensional arrays of coherent single NV- colour centres", (The 69th Diamond Conference, 2018).

Acknowledgments

I would like to acknowlege the great support I have been fortunate to receive from many colleagues throughout the tumult of the past few years. In particular I'd like to thank my supervisor Gavin Morley who has provided support and guidance through thick and thin in all aspects of the challenges of taking on a PhD as a mature student. Thank you also to Mark Newton for your expertise and encouragement. Thanks to Ben Green for always giving readily of his invaluable practical expertise as well as his support and encouragement. Many thanks also to Angelo Frangeskou, Guy Stimpson, Yashna Lekhai, Phil Diggle, Ben Breeze, Matt Dale, Claire Meara, Mareike Herrmann, David Greenwood, Sinead Mottishaw, Claudio Valotto, Chris Wedge, Enrick Nako, Mika Tamski, John Newland, Sam Cobb, Anis Rahman, Maik Icker, Patrick Salter, Sam Johnson, Paul Hill, Erdan Gu, Laiyi Weng, Larry Chen, Jason Smith, Soumen Mandal and others I may have regrettably omitted for their support, encouragement and advice both personal and technical.

In particular I would like to acknowledge the vast amount of collaborative work put in to developing the multi-experiment F$^\sharp$ code base and all the related tooling, training and design. Anton Tscholakov developed most of the core library, the PicoScope 5000 series driver amoungst others, the first complete experiment and set out much of the underlying structure. Jake Lishman also made signficant contributions - in particular adding pulse sequence support for the Keysight N5172B despite inherit limitations. Ben Green and other

members of the group also contributed at different stages, including working with Anton to develop the first working graphical user interface (GUI) for a confocal experiment using this system and contributing to design discussions.

I'd also like to thank Ben Green and Phil Diggle for their work on the Python based Qudi system, as well as the many contributors at University of Ulm for building and making available a working, comprehensive, modular confocal experiment platform.

I'd like to thank Ben Green, Angelou Frangeskou, Phil Diggle and the many others who have helped to build our optics labs up from a single bare room but in particular for their work constructing our main room temperature confocal microscope. Ben Breeze for his patience explaining practical use of EPR & Raman spectrometers and how to interpret the subtleties of their spectra.

Thank you to Jeanette Chattaway and all of the team in the departmental workshop for all their advice and efforts machining brass, titanium, aluminium and PTFE however demanding my designs. Thanks also to Mareike Herrmann for laser machining and acid cleaning. Thanks to Sam Cobb & Ben Green for advice & development work on photolithography and forming metal electrical contacts on diamond. Thanks to David Greenshields and our electronics workshop for the development of the pulse integrator and voltage scanners amoungst other projects and the support using their PCB etching apparatus. Thanks also to Simon Leigh for the use of the Engineering department's 3-d printing facility. Thanks also to Soumen Mandal, Ollie Williams and Laia Gines for their work milling and cleaning nanodiamonds from bulk material.

Finally, thank you to my family, my friends and my son William for their forebearance, patience and support through all the changes and challenges along the way.

Declarations

I declare that the work presented in this thesis is my own except where stated otherwise, and was carried out entirely at the University of Warwick, during the period of September 2014 to July 2018, under the supervision of Dr. Gavin Morley. The research reported here has not been submitted, either wholly or in part, in this or any other academic institution for admission to a higher degree. Some parts of the work reported and other work not reported in this thesis have been published, as listed below. It is anticipated that further parts of this work will be submitted for publication in due course.

Abstract

The nitrogen vacancy centre (NV^-) in diamond has promising properties for several applications in quantum computing and sensing. The works described in this thesis each contribute towards our ability to build systems using NV^-. One such aspiration is the capability to build scalable arrays of deterministically placed, high quality qubits which can be accessed optically. NV^- is a potential candidate however the best current method for entangling two NV^- centres requires that each one is in a separate cryostat which is not scalable. This work shows that single NV^- centres can be laser-written in arrays 6-30 µm deep inside of a diamond with spin coherence times that are an order of magnitude longer than previous laser-written NV^- centres and at least as long as naturally-occurring NV^-. This depth is suitable for integration with solid immersion lenses or optical cavities. Depth-dependent T_2 measurements reveal which depths avoid surface-induced decoherence. Tens of thousands of these NV^- could be written into one diamond plate. Additionally a fibre coupled, cryogenic, fluorescence confocal microscope has been developed to evaluate the possibilities for using scattered nanodiamonds for sensing at low temperatures.

Abbreviations

ADC	analogue to digital converter
AOM	acousto-optical modulator
APD	avalanche photodiode
API	application programming interface
CFM	confocal microscope
CLR	Common Language Runtime
CPW	co-planar waveguide
CCD	charge-coupled device
CVD	chemical vapour deposition
DEER	double electron–electron resonance
DTR	Data Terminal Ready
DU	discriminated union
DWF	Debye-Waller factor
EDAX	energy dispersive X-ray analysis
ENDOR	electron nuclear double resonance
EPR	electron paramagnetic resonance
ESR	electron spin resonance
FC	fibre coupled
FIB	focused ion beam
FPGA	field programmable gate array
FWHM	full width half maximum
GUI	graphical user interface
HPHT	high-pressure high-temperature
HBT	Hanbury-Brown-Twiss

ICP	inductively coupled plasma
IDE	integrated development environment
ISC	inter-system crossing
LT	low temperature
Q	resonator quality factor
QIP	quantum information processing
QKD	quantum key distribution
MFD	mode field diameter
MO	molecular orbital
NA	numerical aperture
NI	National Instruments
NIR	near-infrared
NMR	nuclear magnetic resonance
NQIT	the National Quantum Information Technology Hub
ODMR	optically detected magnetic resonance
o.u.	optical units
cwODMR	continuous wave optically detected magnetic resonance
pODMR	pulsed optically detected magnetic resonance
PCB	printed circuit board
PIC	PIC microcontroller family
PL	photo-luminescence spectroscopy
PM	polarisation maintaining
PLE	photo-luminescence excitation
PSB	phonon side band
PSF	point spread function
RF	radio frequency
SEM	scanning electron microscopy
SCPI	Standard Commands for Programmable Instruments
SIL	solid immersion lens
SLM	spatial light modulator
SMA	sub-miniature A
SMB	sub-miniature B
SMP	sub-miniature push-on

SNR	signal-to-noise ratio
SPAD	single photon avalanche photo-diode
SPE	single photon emitter
TCSPC	time-correlated single photon counting
TEM	transmission electron microscopy
UV	ultraviolet
VISA	Virtual Instrument Software Architecture
VVA	variable voltage attenuator
VHF	very high frequency (30 MHz to 300 MHz)
WPF	Windows Presentation Foundation
XAML	Extensible Application Markup Language
XML	Extensible Markup Language
ZFS	zero-field splitting
ZPL	zero phonon line

Chapter 1

Introduction

> The substance that possesses the greatest value, not only among the precious stones, but of all human possessions, is adamas; a mineral which, for a long time, was known to kings only, and to very few of them.[1]
>
> *Pliny the Elder*

Colour centres in diamond not only give gem stones attractive hues - they can allow us extraordinary access to probe the world at the quantum mechanical scale. Quantum mechanics and thermodynamics lectures for undergraduates may imagine arrays of individual, quantised spins as a thought experiment but in the twenty years since Joïg Wrachtrup and colleagues showed that single spin systems in diamond could be used to perform magnetic resonance experiments using confocal microscopy[2], the field has developed rapidly and we can now routinely manipulate individual spins in diamond using light and microwave pulses. Many groups are now working on ways to engineer colour centres[1] into synthetic diamond (and similar materials) for nano-scale sensing, quantum computing and fundamental physics experiments.

This thesis covers two bodies of work towards using NV^- as a component in scalable quantum computing systems. The first presents work on a cryogenic confocal microscope capable of investigating how single NV^- in nanodiamonds can be used to coherently sense the state of other nearby spins. The second is a comprehensive investigation of three-dimensional arrays of laser-written NV^- and laser written structures in diamond at room temperature which demonstrates that laser writing is a excellent technique for making high quality single NV^- where we need them to be.

---

[1] Colour centres are also known as point defects

1.1 Cryogenic confocal microscopy of nanodiamonds

This part of the presented work had the aim of establishing if it is possible to coherently read out the spin state of dopant atoms near the surface of a silicon substrate through single NV^- colour centres in nanodiamonds. Applications of NV^- as a probe for optical read out of the state of other spins for quantum computing have been proposed previously[3–7] as sell as for low-temperature quantum sensing at the microscopic scale[8]. If this were shown to be possible from nanodiamonds nestling closely to the surface, NV^- could provide an optical route to coherently read out the electron spin state of phosphorus dopant atoms deterministically placed with hydrogen lithography[9].

Although the NV^- works effectively for magnetometry at room temperature[10], many applications require cooling to cryogenic temperatures either to produce entangled states[11], to make use of the long quantum "memory" of other electron or nuclear spins[12–15] such as dopant atoms in silicon[16] or for single-shot read out schemes[8]. The building of a cryogenic confocal microscope to investigate the use of nanodiamonds[17–27] for optical read out of the electron spin state of dopant atoms in silicon at low temperatures is described in Chapter 3.

A number of technical developments were required to this end - more than initially anticipated. The layered challenges involved in this aim will be discussed in more detail in Chapter 3. Sustaining the exceptionally long quantum coherence times of electron spins in silicon and achieving the entangled measurements need for quantum computing applications required construction of the instrument around a stable, cryogenic, confocal microscope with an extensive list of requirements Section 3.1.

Sensing through surface scattered nanodiamonds Figure 1.1 is also com-

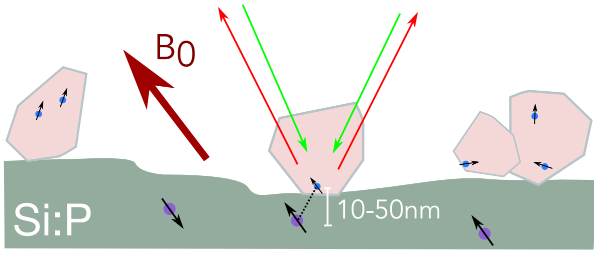

Figure 1.1: Nanodiamonds as single-spin NV$^-$ sensors on the surface of phosphorus doped silicon. This goal motivated the requirements of the system to be capable of long duration pODMR experiments at liquid helium temperatures with three-dimensional magnetic field control, efficient light collection, very low excitation light leakage, secondary RF excitation and some means to find and characterise nanodiamonds in-situ.

plicated by the need to apply a magnetic field orientated to the crystallographic axis of symmetry of each nanodiamond Section 3.7 - each of which is in an arbitrary orientation. Sensitivity to leakage of energetic optical photons mandated development of a fast, higher-exclusion optical switch to control optical excitation pulses Section 3.4. Running complex experiments on a home-built confocal microscope required development of software and automation to efficiently locate sites with appropriate properties Section 3.5. Whether or not any sites have the required properties, a statistically significant number of sites need to be characterised - which also necessitated indexing the position of nanodiamonds for comparison with non-optical techniques such as scanning electron microscopy (SEM) Section 3.9.

Significant progress was made on the cryognic instrument development despite unforeseen difficulties but a second strand of work at room temperature was started in parallel studying laser-written single NV$^-$ centres in collaboration with Patrick Salter and Jason Smith in Oxford in order to ensure results were available in the time available.

1.2 Laser-written single NV^- arrays

Following on from some minor work assisting on the laser-written single NV^- centre work by Larry Chen[28] I developed an interest in finding out what limited the yield of single NV^- produced, where they formed, how accurately they could be positioned, whether their spacing mattered and what limited their coherence time. I also wondered how these induced NV^- could be combined with laser written wires[29] to make devices. To answer these questions, in collaboration with Jason Smith's group and the National Quantum Information Technology Hub (NQIT), I designed and measured a number of laser-written structures in diamond. These included large, three-dimensional arrays of NV^- at varying depths over a wide area of an electronic grade diamond[30].

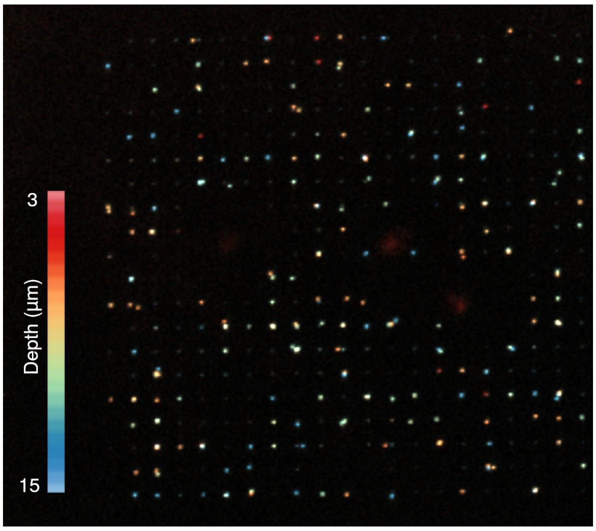

Figure 1.2: Stacked confocal image of a 3-d array of NV^- (array H). Colour is used to indicate the depth of the fluorescent site. Details of the creation of this image are covered in Chapter 4.

Using the technique of laser writing NV^- pioneered by Booth, Salter, Chen & Smith - described in Section 2.4 - this work will show that the laser writing technique[31–35] can produce the highest quality of NV^- in deterministic locations and at a range of depths beneath the surface of diamond[28, 36]. The experimental procedures for this work are described in Section 4.3 with results presented in Section 4.4 and in publication[30] Figure 1.2.

By studying a larger number of sites written with the same pulse energy across different regions of diamond I aimed to answer some of the questions I had raised about the variations in the initial work[28], using statistics to better understand how to control laser writing of single NV^- in diamond. The results of this work - presented in Chapter 4 - include the longest quantum coherence times measured in man-made single NV^- centres without isotopic purification or dynamic decoupling. Laser writing is shown to be capable of producing high quality, stable single colour centres in synthetic diamonds with properties as good as those of naturally formed NV^-.

1.3 Background to this work

These pieces of work have a common basis in the study of diamond over the last sixty years, in the development of electron spin manipulation with microwaves that developed over the same period into electron paramagnetic resonance (EPR), and of confocal microscope (CFM). Discussion of this underlying work and the principles involved is presented in Chapter 2.

1.4 Electrodes and future work

A summary of the results and achievements can be found in Chapter 5 including some discussion of other related pieces of work included the development of the experimental equipment Section 3.4.1, Section 3.7, software Section 3.5 and automation Section 5.1 which enabled many of the measurements in this work and other experiments in our lab. Finally, some ongoing work towards integrating laser-written colour centres with laser-written electrodes is discussed in Section 5.3.1.

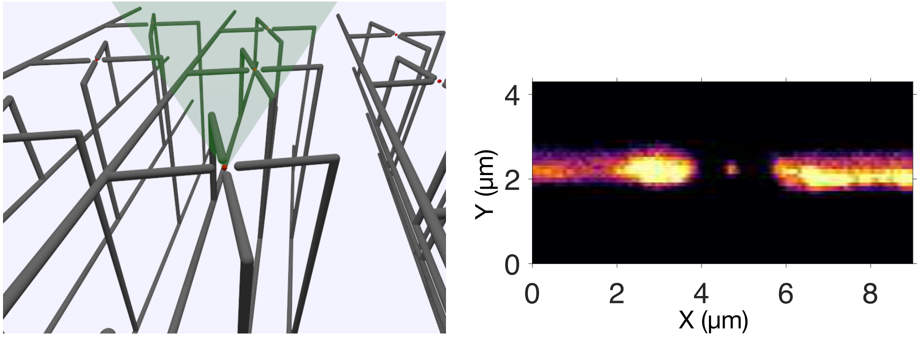

Figure 1.3: Laser written wires with single NV^{-}. *(left)* A 3-d model of some of the laser written electrode structures created *(right)* A fabricated, laser-written single NV^{-} between a pair of laser-written electrodes inside a diamond.

Regrettably this work Figure 1.3 was not completed as the diamond was lost during clean room processing however preparations had been made to test the conductivity of laser-written electrodes at different temperatures and frequencies and to apply large magnitude ($\mathrm{MV\,m^{-1}}$) electric fields to individual colour centres created between electrodes a few micrometres apart, deep within diamond. More ambitiously still, this same diamond contained structures and complementary lithography which aimed to demonstrate the supporting control structures needed for addressable, tunable, integrated arrays of laser-written NV^{-}. These included a interwoven structures to deliver three dimensional strain compensation using Stark shift fields[37], microwave/RF excitation delivery and three-dimensional magnetic field adjustment. A scheme is outlined in Section 5.3.1 where these techniques could be combined to form an integrated array of NV^{-} based qubits.

Diamond has fascinated as the quintessential gem stone for a over a thousand years, since the days of trade along the Silk Road. Prized for glinting, sparkling and seemingly trapping light. Hardest of materials. Most extreme. A rare, impervious treasure which could not be synthesised by alchemy or immitated. It is nothing short of alchemy that we can now both synthesise this extreme material by high-pressure high-temperature (HPHT) and chemical vapour deposition (CVD) techniques and adapt its properties for applications which could not have been imagined by Pliny when he wrote of diamond by its ancient name, *adamas*[1].

Chapter 2

Theory & background

2.1 Diamond & the NV$^-$ colour centre

2.1.1 Properties of diamond

Diamond is an extraordinary allotrope of a common but exceptional element - carbon. With atomic number 6, carbon is one of the atomically lightest elements and yet it can form up to four covalent bonds through its half occupied outer 2s^2 and 2p^2 orbitals. With these orbitals hybridised in the sp^2 configuration, three bonds with a bond angle of 120° can make two-dimensional planar structures - as found in the layered allotrope: graphite. Carbon's outer shell can also be hybridised in the sp^3 configuration with four covalent bonds distributing themselves with a bond angle of 109.5° in a three-dimensional tetragonal geometry Figure 2.1. This is the form of the covalent bonds in the diamond lattice. Each atom in this lattice bonds to four neighbours making diamond one of the hardest, stiffest and most extreme materials.

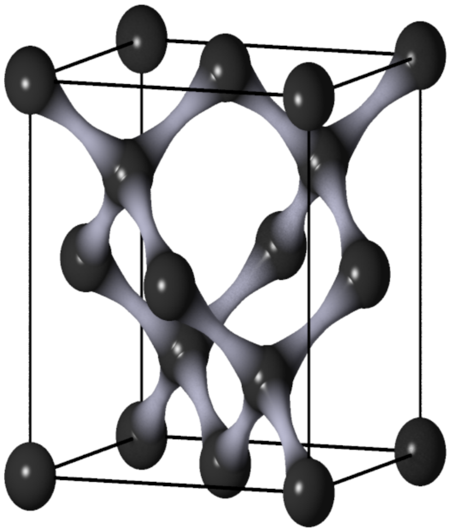

Figure 2.1: The conventional unit cell of the diamond lattice.

To develop a sense of the symmetries of defects in diamond it is instructive to look at projections along the [100], [110] and [111] directions Figure 2.2.

Typically CVD grown plates of diamond have a (100) orientated top face and either {110} or {010} orientated sides so the four key symmetry axes, with three-fold rotational symmetry $[111]$, $[1\bar{1}\bar{1}]$, $[\bar{1}1\bar{1}]$ and $[\bar{1}\bar{1}1]$ can be found at 45° to the top face.

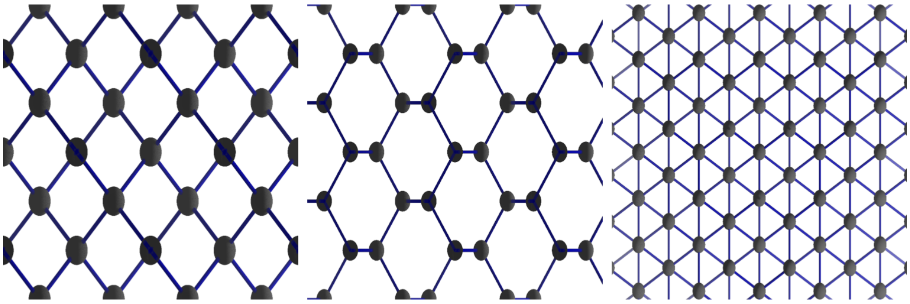

Figure 2.2: The crystallographic structure of diamond projected orthographically along the [100], [110] and [111] directions.

Diamond is an insulator. It has some similarities with silicon, however it has an exceptionally wide electronic band gap of 5.5 eV (compared to the 1.1 eV band gap of silicon), requiring ultraviolet (UV) light to excite electrons from the valance to the conduction band. This is the reason for diamond's exceptional optical transmission. The characteristic macroscopic vibrational modes of the lattice can be observed in Raman spectroscopy. Inelastic scattering involving one phonon results in the characteristic bright diamond Raman line at a shift of 1332 cm^{-1}. A second order Raman feature is commonly seen with approximately twice this shift.

2.1.2 Synthetic diamond growth

Diamond is formed naturally at great depths under conditions of high pressure and temperature Figure 2.3. All of the early work on diamond was conducted on natural diamonds.

Diamond can now be grown synthetically using two processes. In 1954

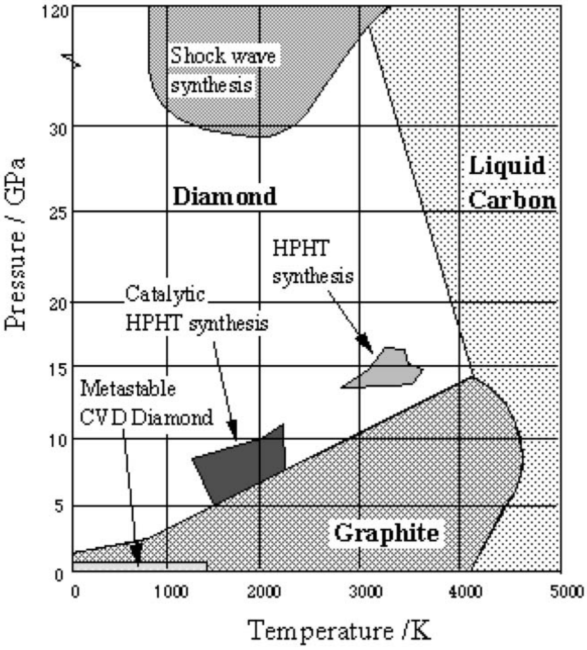

Figure 2.3: Phase diagram for carbon annotated with the HPHT and CVD growth regimes[38, 39]. Diamond is the stable form for carbon at the very high pressures present deep in the Earth's crust or in an HPHT hydraulic press. The CVD process instead synthesises diamond layer by layer from a plasma in a metastable regime.

Howard Tracy Hall succeeded in synthesising diamond[40] at the General Electric Research Laboratory using the HPHT process with a novel belt press generating ultra-high pressures (10 GPa) at high temperatures (1600 °C). Whilst these pressures are less than those in the Earth's mantle, the HPHT process uses metallic solvent-catalysts such as iron, nickel or cobalt which accelerate the process from millions of years to hours.

In the CVD process, a plasma is formed under carefully controlled conditions from a mix of gases, including methane, in a high power microwave reactor. The plasma is brought into contact with a diamond seed crystal on a temperature controlled platten and atoms from the plasma are incorporated on the surface layer by layer in a process of step-flow growth. Diamond is grown an atomic layer at a time. It is possible to change the gas mix to change the properties of the diamond being grown and to overgrow the surface of a diamond. Isotopically enriched gases can be used to grow diamond with ^{12}C (with no unpaired nuclear spin) rather than a natural abundance of 1.1% ^{13}C with nuclear spin $^1/_2$.

Typically HPHT diamonds have less internal strain than those grown using the CVD method however they will typically incorporate impurities from the growth medium and have more pronounced crystallographic growth sectors. CVD diamond typically incorporate more internal strain from dislocations introduced in the step-flow growth process. Nitrogen is commonly included to increase the growth rate by initiating new layers of growth. Several different grades are produced for different markets by the main commercial manufacturer, Element Six (E6). For research into using colour centres as quantum devices Element Six produce an "electronic grade" material which has exceptionally low nitrogen concentrations - under 5 ppb.

2.1.3 Colour centres in diamond

The colour seen in some diamonds is due to the presence of colour centres (also known as crystallographic point defects) in the crystal lattice. These can introduce localised energy levels in the band gap within the overall electronic and vibrational context of the diamond lattice[41] which can be identified both optically[42] and through EPR[43]. Colour centres may be due to substitution of a carbon atom by another atom, an interstitial atom squeezed in between sites, vacancies where a carbon atom is missing or complexes of these things Figure 2.4.

A vast number of colour centres have been identified in diamond[42] however only a few have played a role in this work which will now be discussed

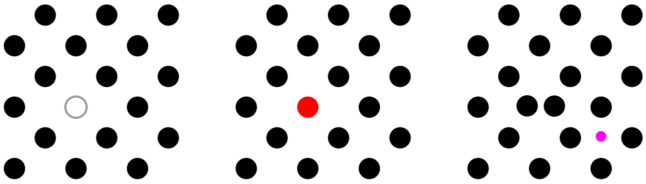

Figure 2.4: An illustration of the main crystallographic point defect (colour centre) types in diamond. A vacancy site (left), a substitutional site (centre) and an interstitial site.

briefly to establish the terms used. Substitutional nitrogen ($\mathrm{N_s^0}$) is commonly found in diamond as grown[43]. The nitrogen atom has an extra electron which remains unpaired so this colour centre is paramagnetic and in EPR spectra of diamond this common feature is often known as a P1 centre[43]. Diamonds with high concentrations of $\mathrm{N_s^0}$ are yellow[44]. Radiation damage to the lattice can dislodge carbon atoms to form vacancy sites[45, 46]. Diamonds with a high concentration of neutral vacancies can appear grey. Annealing diamond at high temperatures can make colour centres mobile or can decompose some complexes[47, 48]. By careful choice of temperature, activation of these processes and their rates can be controlled[45, 46, 48, 49]. Some defects may aggregate to form more stable complexes which may pair spins and negate their paramagnetic properties. Colour centres also change their properties depending on their charge state and can change charge state by trapping or losing an electron - particularly if the electron can be excited into the conduction band. The colour centre of particular interest in this work is the negative charge state of the nitrogen-vacancy complex ($\mathrm{NV^-}$)[50, 51] Figure 2.5.

2.1.4 The nitrogen-vacancy complex

The nitrogen-vacancy complex[51, 52] has two commonly seen charge states. In the $\mathrm{NV_0}$ charge state a single unpaired electron is bound to the complex. $\mathrm{NV_0}$ is optically active with a zero phonon line (ZPL) at 575 nm and is paramagnetic however it does not exhibit optically detected magnetic resonance (ODMR). NV^- has a additional electron so that it has a ground and excited triplet state with a ZPL at 637.7 nm. Even with no magnetic field, the $m_s = \pm 1$ states have a higher energy with a zero-field splitting of 2.87 GHz. In the presence of a magnetic field the energies of the $m_s = \pm 1$ states diverge which can be seen in EPR as Zeeman splitting.

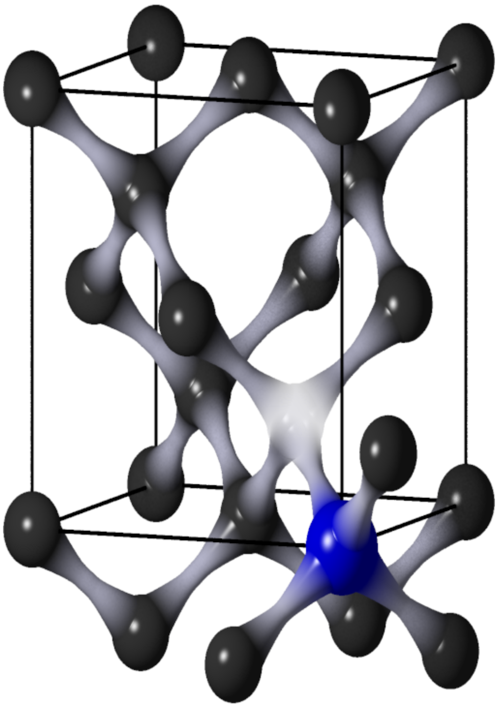

Figure 2.5: Illustration of the nitrogen-vacancy system - a substitutional nitrogen atom adjacent to a vacancy. The system behaves differently for different charge states. The nitrogen donates an electron to form the locally charge neutral NV_0 colour centre. Trapping an additional electron forms the NV^- colour centre, a spin 1 system. Heat and light can drive changes to the charge state.

The NV^- colour centre in diamond has been of particular interest as it has spin-state selective optical relaxation paths which can be used to perform ODMR[53–55] Figure 2.6. From the triplet ground states $^3A_2$ NV^- can be optically excited into the ^3E triplet excited states in a spin conserving transition. The lifetimes of both the $m_s = 0$ and $m_s = \pm 1$ excited states are around 10 ns[51] (which leads to a total emission rate from a single NV^- of around 100 photons per microsecond). However, NV^- also has a singlet state and inter-system crossing (ISC) transitions exist from the triplet excited states[56] into a singlet state. Crucially, the probability of crossing into the singlet state from the $m_s = \pm 1$ excited states is much higher than from $m_s = 0$. The singlet ground state ^1A has a much longer lifetime of 300 ns to 400 ns[51], eventually transitioning back to the triplet ground state by a non-radiative process (mainly) or by infra-red emission. This “trapping” leads to spin-selective dimming of the emission of NV^- when the spin state is $m_s = \pm 1$. The ISC from the singlet to the triplet state ground state also has a crucial property - the rate of transition to the $m_s = 0$ ground state is much higher than to $m_s = \pm 1$. The inter-system crossings through the singlet state give NV^- both optical spin contrast and rapid optical spin polarisation[50] into the $m_s = 0$ ground state.

The negatively charge state NV^- has three-fold rotational symmetry about the [111] N-V axis. Typically CVD plates are orientated with a (100) surface so that all of the [111] orientations have a component perpendicular to the optical path and optical transitions Figure 2.6 are driven through the N-V dipole. This introduces a dependence on the angle of polarisation of linearly polarised excitation light with a $2:1$ contrast.

2.1.5 The phonon side band (PSB) and zero-phonon line (ZPL)

Localised colour centres exist in the diamond lattice and are affected by the lattice’s vibronic modes. These effects can be viewed semi-classically as generating energy sub-levels above the excited and ground states by the absorption or emission of a number of phonons Figure 2.7. Relaxation from these states is

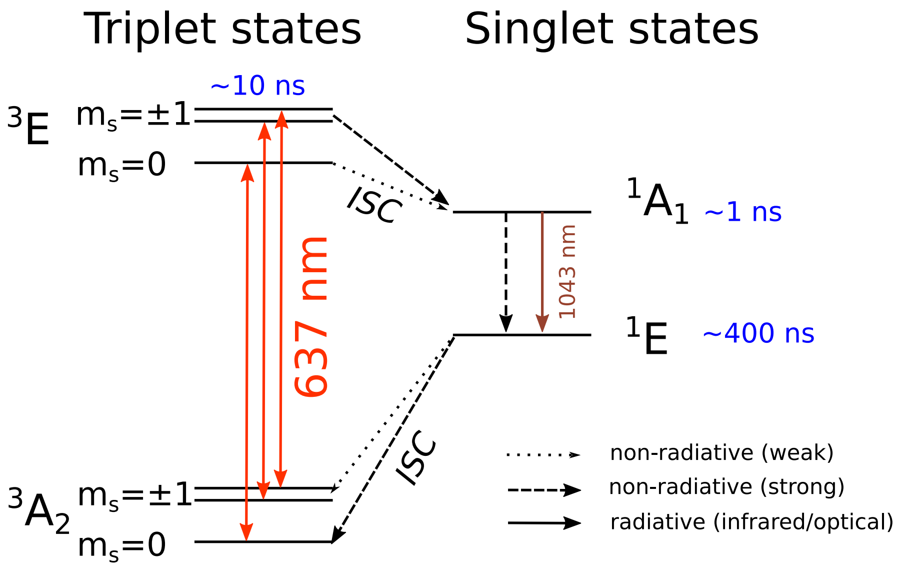

Figure 2.6: The optical transitions of NV$^-$. The ISC between the triplet and singlet states gives rise to both the spin-dependent contrast in fluorescence and the optical spin polarisation effect. Approximate lifetimes of the excited states are shown in blue[51] - the key is that relaxation from the $m_s = \pm 1$ excited state through ISC is more likely than from $m_s = 0$. The long lifetime of the singlet state suppresses fluorescence giving optical spin contrast. Optical spin polarisation occurs as the singlet state will decay preferrentially to the $m_s = 0$ ground triplet state. The ZPL of the ^{3}E $\rightarrow$ ^{3}A$_2$ transition is at 637.7 nm, however NV$^-$ also has a significant PSB.

much faster than the lifetime of the "undecorated" energy levels however they play an important part in the spectroscopy of colour centres. Colour centres with different symmetry properties are affected differently by the longitudinal and transverse vibrations of the lattice and NV$^-$ is strongly affected by lattice phonons. These phonon interactions affect both the emission and absorption spectrum, symmetrically about the ZPL, and so the NV$^-$ colour centre most efficiently absorbs green light before relaxing through a rapid non-radiative phonon process into the ^3E excited state. From the excited state NV$^-$ emits red light over a characteristic phonon broadened emission spectrum centred around 680 nm Figure 2.8. The small ZPL feature can be seen at 637.7 nm however the majority of the fluorescence emission of NV^- can be detected in the PSB as more of these phonon mediated transitions are available than direct ZPL transitions.

The fraction of the total emission in the ZPL compared to ZPL and PSB is often termed the Debye-Waller factor (DWF) and this can be related indirectly to the lattice temperature through models including the strength of the electron-phonon interaction of the point defect (the Huang-Rhys factor), the phonon density of states and the occupation of those phonon modes as a function of temperature from Bose-Einstein statistics [41, 44, 57, 58]. However, the relative scale for this temperature dependence of the DWF is naturally to the Debye temperature which is more than 2000 K for the stiff lattice of diamond so the variation at low temperature is modest.

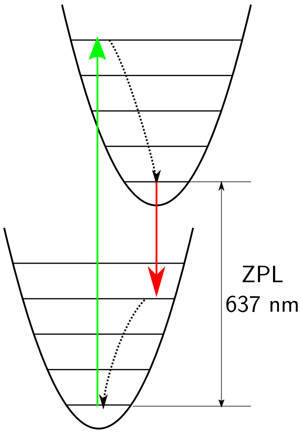

Figure 2.7: The semi-classical Franck-Condon mode: vibronic modes of the lattice are added to the energy of the optical transitions as quantised phonon excitations. These allow transitions between a range of sub-states mirroring the population of phonons which are reflected in a characteristic PSB envelope in both the excitation and emission spectra. The ZPL corresponds to the fundamental transition between the vibrational ground states.

The Debye-Waller factor of NV^- can be affected to some degree by environmental changes other than temperature. In nanodiamonds, it has been found that the choice of substrate has a dramatic effect[59] with the Debye-Waller factor varying between 10% on silicon with an oxidised surface to < 1% on glass at 3.5 K. More significant enhancement of the ZPL can potentially be achieved by using the Purcell enhancement effect of a high Q-factor, resonant optical cavity[60, 61] to restrict the emission modes of the colour centre to those of the cavity although this is technically challenging to integrate.

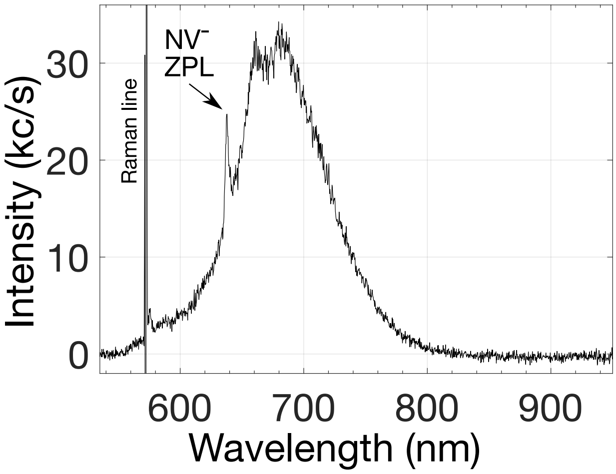

Figure 2.8: The emission spectrum of a single NV$^-$ colour centre excited with 532 nm light at room temperature. This experimental result will be discussed in more detail in Section 4.4.

The large shift between the optimal excitation wavelength and the fluoresence maximum can be convenient experimentally as a dichroic beam splitter is sufficient to separate the excitation light and fluorescence emission. Less conveniently, efficient light collection over the breadth of the emission spectrum of NV$^-$ PSB requires the use of more complex achromatic or apochromatic optics to compensate for chromatic dispersion. The PSB emission is more problematic for quantum entanglment experiments as lattice phonon interactions obliterate quantum information rendering these photons an unwanted byproduct in such experiments. What is more, the optical frequency of ZPL emission from different sites must be indistinguishable for quantum operations so that measurement cannot trivially determine which site was the source of emission.

Cooling to liquid helium temperatures narrows the ZPL emission linewidth which is essential for indistinguishable photon emission and entanglement operations. Cooling also transfers some emission from the PSB to the ZPL (although not as dramatically as one might wish - DWF is still only about around 4% at 77 K[60] in bulk diamond).

Strain in the lattice around NV^- sites is typically the main contributor to site-specific variation in the ZPL position (inhomogenous broadening) and these strain induced shifts can be measured with high resolution at cryogenic temperatures using photo-luminescence excitation (PLE) (resonant excitation with detection in the PSB) along with temporal variations in the emission spectrum (spectral diffusion). Diamond can be grown or treated to reduce internal strain which can help to minimise these shifts however this is difficult to achieve in the growth of low nitrogen, electronic grade CVD diamond.

2.1.6 ODMR of single NV^-

Astonishingly, if the concentration of NV^- centres is sufficiently low, individual single colour centres can be observed and their spin state manipulated. Detection of single centres using confocal microscopy was first demonstrated in work by Jörg Wrachtrup in 1997[2]. This work was continued at the University of Stuttgart, notably with Fedor Jelezko, to understand the spectrographic structure of NV^- [62] and to show that the spin state of individual colour centres could be read-out[63] and manipulated[64]. Other work showed the long ($T_2 \approx 60\,\mu s$) room temperature coherence time[65] and broadened the community working on single NV^- centres.

The observation of single NV$^-$ at room temperature by Jörg Wrachtrup et al in 1997 [2] was followed by low temperature measurements by Fedor Jelezko [62] including detailed spectroscopy of the ZPL using PLE[63]. Within ten years of the initial publication, manipulation and read out of single spins using pulsed ODMR was demonstrated [64, 66] and used to measure the spin coherence properties of single NV$^-$ colour centres. Progressively control of NV$^-$ centres has been refined with understanding of the effect of the concentration of ^{13}C nuclei[67, 68] and quantifying the requirements for alignment of the bias magnetic field[67] to maximise spin coherence lifetimes. They to both set and read out the spin state of individual electrons[]. NV$^-$ can now be used to make measurements of nearby ^{13}C nuclear spins[69] and protocols have been developed for single-shot readout[70], a prerequisite for entanglement experiments and to use those nearby spins to “store” quantum state[71–73] or create entangled quantum states. Microwave-free λ schemes have been developed to permit all optical spin control[74] (although these are not used here). The field has matured somewhat however the transition to commercial applications of NV$^-$ has not yet arrived and developments are required before those applications can emerge. This raises questions such as: What are the applications of NV$^-$? What properties need to be controlled or improved and how? What are the advantages of single NV$^-$ in these contexts?

2.1.7 Nanodiamonds

Nanodiamonds are less than 1 µm in size which changes the environment for colour centres compared to those in bulk diamond. An advantage is that fluorescence can more readily escape from a sub-wavelength nanodiamond than a bulk diamond with the “light box” effect of diamond’s high refractive index. However, the proximity of the surface and resultant internal strains are also likely to cause charge state instability and shifts in emission. Their size brings colour centres into close proximity with the environment outside the diamond which is ideal for short range sensing[75, 76] and NV$^-$ have been shown to have stable fluorescence in particles as small as 7 nm[17] however their fluorescence and spin properties are influenced by their supporting substrate[77, 78] and surface condition[79].

Nanodiamonds can be produced either directly, commonly by detonation, or from bulk diamond by e.g. mechanical milling. To produce nanodiamonds with reduced optical absorption, improved photo-stability and improved spin coherence properties the Morley group has worked with Oliver Williams and Soumen Mandal at Cardiff University to mechanically mill nanodiamonds from high grade CVD plates for use in optically levitated NV$^-$ work[22, 80, 81] and in the low temperature Attocube confocal microscope. In addition to high purity electronic CVD based nanodiamonds, high nitrogen ^{12}C isotopically purified nanodiamonds have produced which might have applications along the lines of Helena Knowles work on coherent spin clusters[82].

2.1.8 Quantum technology milestones with NV$^-$

Coupling of two single spins in a solid state system was shown[10] by coupling a single NV$^-$ to a nearby nitrogen atom. Proposals were put forward for how NV$^-$ could be used for quantum information processing (QIP)[83–85]. Further work at University of Stuttgart demonstrated optical readout and control using resonant excitation[74]. Very long ($T_2 = 1.8$ ms) coherence lifetimes in a solid-state system have been shown, using isotopically enriched CVD diamond[86] or an overgrown ^{12}C layer[87]. Combining cryogenic cooling, isotopic purification and decoupling from nearyby spins[88] this has been extended even further to

600 ms[89].

Ronald Hanson's group at QuTech in Delft have shown that single NV$^-$ can be entangled[76, 90–92] and have done so with single NV$^-$ centres separated by over a kilometer - showing that Bell's inequality holds with no loopholes and that the mysterious indeterminism of quantum states is inherent and non-local. They are progressing with work towards quantum networks[11, 93], controlled qubits[94] and entangled multi-qubit systems with NV$^-$ [15].

2.2 Electron Paramagnetic Resonance

Also known as electron spin resonance (ESR), EPR is a technique for probing the electronic environment of materials by probing the transitions between electron spin states in a magnetic field. As the term paramagnetic suggests, this can be thought of as observing properties of the bulk magnetisation. It can also be thought of on the microscopic scale as resonant manipulation of electron spins in a material.

One of the key developments in quantum mechanics was the discovery that electrons have a quantised property we now call spin[95]. Although the electron is a point particle it has intrinsic angular momentum, in much the same way as a particle has mass. It also has a corresponding instrinsic magnetic moment and both of these properties are quantised.

Experimentally, doublets of spectral lines can be seen in the emission spectra of alkali vapours such as sodium in a magnetic field. This was studied in 1896 by Kamerlingh Onnes, J.D. van der Waals and Pieter Zeeman. However the semi-classical model did not give a complete explanation for the anomalous Zeeman effect. In 1922 Stern & Gerlach observed deflection of a beam of neutral silver atoms by a divergent magnetic field[95]. The surprising result was that this produced two distinct populations suggesting that the magnetic moment of electrons was quantised. Wolfgang Pauli postulated in 1924 that this could be explained if in addition to orbital quantised properties (n,l,m) a bound electron had a fourth index with two values and introduced the idea of a *spinor*. Applying minimal coupling to a relativistic 4-vector form of the Schrödinger equation, Paul Dirac found that it was necessary for the electron (and incidentally the positron) basis states in a magnetic field to have symmetry of 2×2 matrices. The projection of the spin state into an observable property in a suitable basis (most conveniently parallel to an applied magnetic field) is quantised into two distinct populations rather than having a continuous range of values. We can express the projection of the spin states as an up $|\uparrow\rangle$ or down $|\downarrow\rangle$ with corresponding eigenvalues $m_s = \pm\frac{1}{2}$. In a magnetic field the energies of the aligned and anti-aligned free electron spin states diverge proportional to the magnetic field strength Figure 2.9. Transitions between these states driven by resonant photons.

The macroscopic probing of spin systems through magnetic resonance[96, 97] with unpaired electron spins through EPR[98–101], as described in Section 2.2.

At the scale of an individual spin the full dynamics of the interaction of spins with electromagnetic waves and their environment are best understood using quantum mechanics. However, in most applications of EPR, readout of the spin state of an individual electron is not feasible. For most analytical purposes EPR is used on samples containing a large number of unpaired electrons. The bulk magnetisation of a material is the sum of an uncountably large numbers of the magnetic moments of many electronic spins, (with a small contribution from nuclear spins).

The observed projections of spin states are not a complete description of the electron spin state at all times however. The complete quantum mechanical wavefunction describing their behaviour has a complex component - as predicted by Dirac's description. This spin state can be envisaged conceptually in complex space on a Bloch sphere - representing the magnetisation.

2.2.1 Continuous wave EPR

Electrons in materials are central to all their chemical properties. How molecules and solids bond and interact is almost entirely due to electrons. The molecular orbital (MO) in a material are filled by the bonding electrons contributed

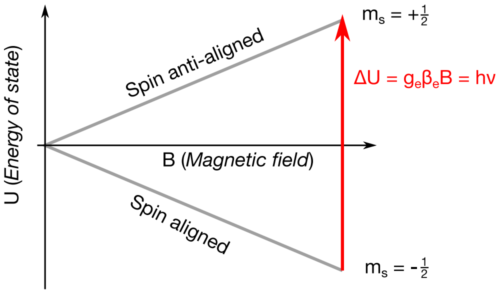

Figure 2.9: The energy difference between the aligned and anti-aligned states of an electron in a magnetic field in the absence of other fields.

by each atom, subject to Pauli exclusion, in the lowest energy configuration available. Chemists may approach this by applying Hund's rules. Often, two anti-symmetric electrons fill a MO yielding no net magnetisation. However, unpaired electrons will precess in any local magnetic field, static or time varying, and act as a phenomenal in situ sensor for chemical environments. This has been exploited since 1945[98–101] and the availability of powerful microwave sources to probe chemical environments to determine structures and chemical activity.

For a population of non-interacting spins, the occupancy of the $|\uparrow\rangle$ and $|\downarrow\rangle$ states in equilibrium is governed by Boltzmann statistics. These populations can be probed by applying a microwave field which flips some of the electrons. Relaxation processes will act to restore the thermodynamic equilibrium. In a conventional continuous wave EPR experiment, the resonant microwave intensity is set to a sufficient low intensity to ensure that relaxation processes can maintain close to the thermodynamic equilibrium population - operating well below saturation[1]. In this regime, the energy loss from the microwave field can be detected as a change in impedance. The normal experimental arrangement for this is to hold the sample in a tuned and matched,

---

[1] As opposed to more dynamic non-equilibrium regimes such as rapid passage or pulsed EPR

resonant microwave cavity with a fixed microwave frequencyFigure 2.10. The coupling of microwaves into the resonant cavity is tuned so that the reflected radiation is minimal. Experimentally, with most microwave sources and the geometric constraints of cavity resonators it is normally convenient to hold the microwave frequency fixed and instead sweep the magnetic field to measure resonances. In order to greatly improve the signal-to-noise ratio (SNR) the field is modulated (conventionally at 100 kHz) and measured as a derivative signal using the lock-in method Figure 2.11.

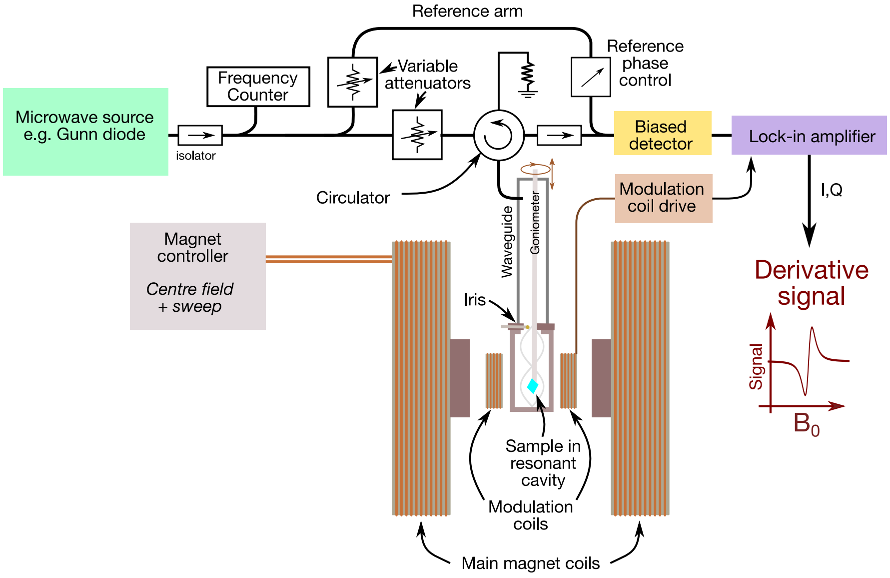

Figure 2.10: A conventional continuous wave EPR spectrometer with a cavity resonator.

The reference arm is used to bias the detector (typically a Schottky diode) in its most sensitive, linear regime (that is linear in power, and so proportional in response to the amplitude squared).

Typical a critically coupled cavity with a resonator quality factor (Q) of 300 at X band (∼9 GHz) would give a cavity resonance 30 MHz wide. Suppose the magnetic field is swept over the condition for the microwaves to be absorbed by the sample. A modulation depth corresponding to 10 MHz would show almost the full depth of response. As the modulation rapidly sweeps up and down the side of this resonance the impedance matching into the cavity fluctuates producing a reflected signal in phase with the modulation. Feeding the modulation and this signal into a lock-in amplifier produces a derivative signal of the sample resonance with magnetic field.

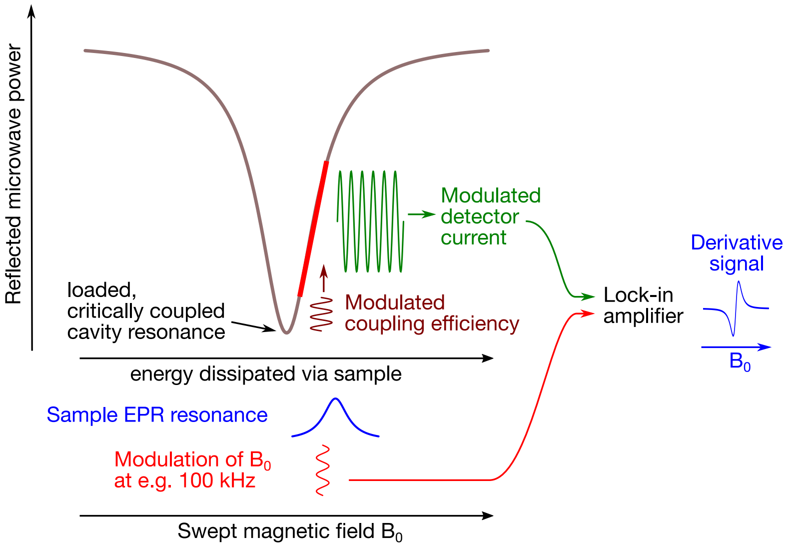

Figure 2.11: An illustration of the interaction of cavity and field modulation in a conventional EPR spectrometer. In most EPR spectrometers a cavity resonator and lock-in amplifier are used to greatly enhance the sample absorption signal from a modulated magnetic field sweep giving a derivative signal.

In conventional continuous wave EPR measurements are taken in equilibrium, which can be explained in terms of the ensemble magnetisation using the Bloch equations. Rapid passage and pulsed EPR are more dynamic, with a continually changing magnetisation, however they still by and large need a large number of contributing spins to forma a detectable population. In some particular cases however, such as using ODMR on NV$^-$, a single spin can be detected and read out. For such isolated, single spins a microscopic, quantum mechanical picture is more appropriate.

2.2.2 Spin Hamiltonian

The spin Hamiltonian is a reduced description of the energetics of a spin system in an environment as the sum of contributing terms. The spin dynamics of many systems can be modelled more clearly with this reduced description without constructing a complicated full Hamiltonian with every conceivable interaction. This approach is particularly effective for modelling the behaviour of point defects in crystals. Comprehensive descriptions of the spin dynamics of solid state systems[102, 103] and the nitrogen vacancy centre in particular[51] are available in the literature, however it is instructive to unpack the spin dynamics of NV^- somewhat in terms of the spin Hamiltonian.

The possible electron configurations for a point defect can be labelled based upon the occupancy of hybridised MO and symmetry. However in practice, once the symmetry group of the system is understood such underlying details can be set aside. It is sufficient to consider a point defect with particular symmetry characteristics as a spin system interacting with its environment. In general the interaction terms may be described as tensor products however experimentally aligning the field to the symmetry axis is often preferrable[67].

$$\mathcal{H}_0 = \mathcal{H}_{EZ} + \mathcal{H}_{ZFS} + \mathcal{H}_{HF} + \mathcal{H}_{NZ} + \mathcal{H}_{NQ} + \mathcal{H}_{NN} \tag{2.1}$$

These terms in the spin Hamiltonian Eqn. 2.1 represent the energy shifts due to:

$\mathcal{H}_{EZ}$ Electron Zeeman interaction - electrons' orientation in the magnetic field

$\mathcal{H}_{ZFS}$ Zero-field splitting - electrons interacting with each other at the same location

$\mathcal{H}_{HF}$ Hyperfine splitting - electron-nuclear coupling

$\mathcal{H}_{NZ}$ Nuclear Zeeman - nuclear spins' orientation in the magnetic field

$\mathcal{H}_{NQ}$ Nuclear quadrupole interaction

$\mathcal{H}_{NN}$ spin-spin interactions between pairs of nuclear spins

The most significant terms for the triplet states of the NV$^-$, $^3A_2$ & ^3E, are zero-field splitting and, in the presence of a magnetic field, the Zeeman splitting term. The triplet ground state is labelled $^3A_2$ for the irreducible representation A_2 under the $C_{3,v}$ symmetry operations. The ^3E state is the higher energy triplet excited state configuration. The letters A and E are the conventional "Mulliken Symbols" for these irreducible representations[104].

$$\mathcal{H}_{ZFS} = \tilde{\mathbf{S}}\mathbf{D}\mathbf{S} = \begin{bmatrix} \hat{S}_x^\dagger & \hat{S}_y^\dagger & \hat{S}_z^\dagger \end{bmatrix} \begin{bmatrix} 0 & D_1 & D_2 \\ D_1 & 0 & D_3 \\ D_2 & D_3 & 0 \end{bmatrix} \begin{bmatrix} \hat{S}_x \\ \hat{S}_y \\ \hat{S}_z \end{bmatrix} \tag{2.2}$$

In general, the zero-field splitting (ZFS) **D** tensor contribution can be described with three coefficients Eqn. 2.2 however in a particular spin system these contributions can be reduced. As the NV$^-$ defect has C$_{3v}$ symmetry (axial) the **D** tensor coefficients can be transformed into its principle axis system, effectively diagonalised, to give the simpler form:

$$\mathcal{H}_{ZFS} = D(S_z^2 - \tfrac{1}{3}S(S+1)) + E(S_x^2 - S_y^2) \approx D(S_z^2 - \tfrac{2}{3}) \tag{2.3}$$

reducing the three coefficients to two Eqn. 2.3. The D component is also much larger than the perpendicular E term and is responsible for the zero-field energy level splitting between the $m_s = 0$ and $m_s = \pm 1$ states. with the spin projection operator in the conventional Zeeman basis of the triplet state

$S_z = \hbar \begin{bmatrix} 1 & 0 & 0 \\ 0 & 0 & 0 \\ 0 & 0 & -1 \end{bmatrix}$ along the axis (usually the magnetic field is aligned to the symmetry axis of NV$^-$ experimentally also[2]). The spin projection operators are hermitian, so $S_i^\dagger = S_i$. At low temperature, in the absence of other fields, the ground state $m_s = 0$ and $m_s = \pm 1$ states of NV$^-$ are separated by the zero field splitting term with $D/h = 2.88$GHz.

When a magnetic field is applied the Zeeman term becomes signficant, splitting the $m_s = \pm 1$ terms. The Zeeman term can be described by:

$$\mathcal{H}_{EZ} = \frac{\beta_e}{\hbar} \tilde{B}_0 \mathbf{g} \mathbf{S} \tag{2.4}$$

where $\mathbf{g}$ is a rank 2 tensor in general Eqn. 2.4. In the case of NV$^-$ with C$_{3v}$ symmetry, $\mathbf{g}$ can be reduced to perpendicular and parallel components $g_\perp$, $g_\parallel$. Commonly the static magnetic field B_0 may be applied parallel to the symmetry axis of the NV$^-$ in which case the transverse component approaches zero and $\mathcal{H}_{EZ} \rightarrow \mu_B g_\parallel B_z . S_z$.

The hyperfine and nuclear quadrupole interactions are expected to be much smaller generally, although they will contribute[69]. Electron spin-spin and electron-nuclear spin interactions will be present as a time-varying or "AC" magnetic field. Some contributions to this magnetic environment will confound measurement and so effort is needed to minimise undesirable additional paramagnetic spins either at nearby surfaces[21, 48] or from paramagnetic point defects[52]. Such "spin clutter" can be controlled either by elimination[21, 48, 86, 87] or by "tuning out" using dynamic decoupling[88, 89, 106]. Specific components corresponding to other nearby spins can potentially be selected to couple to them using a number of techniques[8, 107, 108].

---

[2] The product space of two spin 1/2 states can be diagonalised and worked with in two blocks as the sum of a spin 1 space and a spin 0 space [105], hence the use of a reduced space of size 3.

2.2.3 Pulsed electron paramagnetic resonance

In pulsed EPR, rather than looking to detect the resonance conditions for energy losses through the sample a particular resonance is selected and microwaves are only applied for a finite time. Applied to an ensemble magnetisation, this time varying magnetic field (conventionally B_1)[3] would have the effect of applying a rotation about some axis in the rotating frame - a nutation in the laboratory frame. From a quantum mechanical perspective, the state evolves in a corresponding way by rotation in the rotating frame of the time-varying B_1 field, however in a Hilbert space comprised of the states involved. Projections of these rotations can be observed as Rabi oscillations.

2.2.4 The Bloch sphere representation

The Bloch sphere is a convenient way to visualise the manipulations of the quantum state of a two level system - such as the spin state of NV$^-$ in a microwave field resonant with a ground state spin transition. Following convention, these classical pure states are labelled "up" $|0\rangle$ Figure 2.12 & "down" $|1\rangle$ Figure 2.15 on the Bloch sphere. The surface of the sphere represents pure states in general. Those pure states that are not solely $|0\rangle$ or $|1\rangle$ represent complex superposition statesFigure 2.13. The particular spin states represented by $|0\rangle$ & $|1\rangle$ depend on the transition being driven. In the case of NV$^-$ the system could be initialised optically into the $m_s = 0$ as $|0\rangle$ and driven with resonant microwaves between the $m_s = 0$ and $m_s = +1$ ground level spin states, with the $m_s = +1$ state as $|1\rangle$.

The spin can be made to precess in the rotating frame by applying resonant microwaves Figure 2.13. The rate of precession is proportional to

---

[3] Perhaps due to the low magnetic susceptability of most EPR sample materials, B is more commonly used in the literature rather than the effective local field H although the later would be more correct. This also avoids some confusion with the Hamiltonian ($\mathcal{H}$).

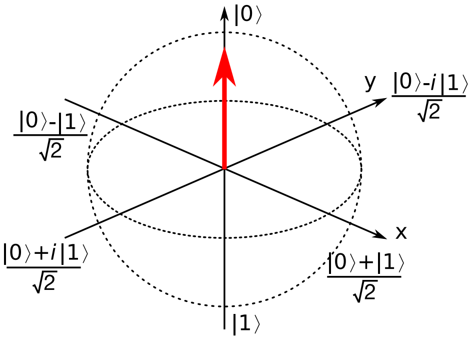

Figure 2.12: The Bloch sphere: a useful pictorial representation of the manipulations of a two level quantum system mapped onto a sphere with the initialised state, labelled $|0\rangle$, pointing up.

B_1, the magnetic field of the resonant microwaves in the rotating frame which is proportional to the square root of the microwave power. The microwave pulse duration controls the angle of rotation in the state space about an axis - conventionally designated the x axis - creating a superposition state. By applying microwaves 90° out of phase with the initial pulse the spin state can be rotated in state space about an orthogonal axis - conventionally labelled the y axis. This creates a similar superposition state with a different phase Figure 2.14. Such pulses are the building blocks of pulse sequences.

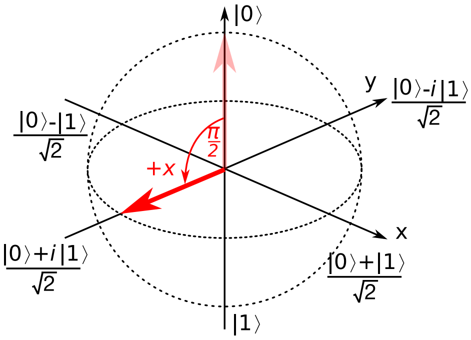

Figure 2.13: Bloch representation showing preparation of a superposition state. In the case illustrated, a ${}^{\pi}/_{2}$ pulse drives $|0\rangle \rightarrow \frac{1}{\sqrt{2}}\left(|1\rangle + i\,|0\rangle\right)$.

In a classical ensemble of spins, microwaves can be used to cause the magnetisation vector to precess in the rotating frame - oscillating between these pure states. The frequency of these oscillations - the Rabi frequency - is proportional to the strength of the magnetic field component of the resonant microwave field in the rotating frame. With a non-classical, quantum system such as a single NV$^-$ a classical magnetisation value will not suffice. The state of a single NV$^-$ can be expressed as linear combination of $|0\rangle$ & $|1\rangle$ with complex coefficients.

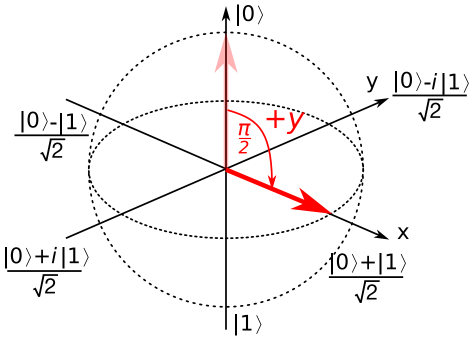

Figure 2.14: Bloch picture showing preparation of a superposition state orthogonal to the previous example. In the case illustrated, a $^{\pi}/_{2}$ pulse with orthogonal phase drives $|0\rangle \rightarrow \frac{1}{\sqrt{2}}(|0\rangle + |1\rangle)$.

Commonly, experiments start with preparation of a superposition state of $|0\rangle$ and $|1\rangle$ by applying a microwave pulse a quarter of a Rabi period long - a $^{\pi}/_{2}$ pulse Figure 2.13. Microwave phase is significant with the phase of the initial pulse in a sequence of pulses conventionally designated x and represented by a rotation about the x axis on the Bloch sphere Figure 2.13. Microwaves of orthogonal phase will induce rotations about the y axis in the rotating frame Figure 2.14. For the general case of statistical ensembles of spins, mixed states can be represented pictorially as lying within the sphere or more completely as a density matrix.

The spin state can be inverted by applying a pulse of longer duration. The length of pulse required for a particular microwave power and correspond-

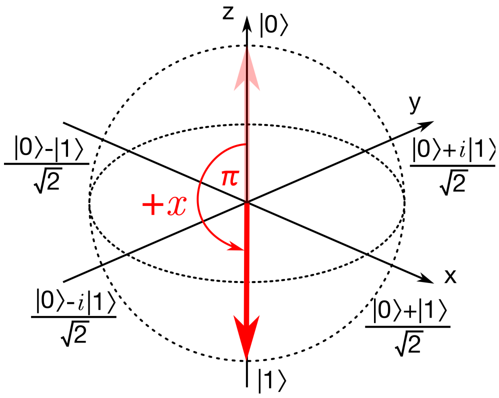

Figure 2.15: The spin state can be inverted by applying a longer duration π microwave pulse as illustrated here. This can be done using either phase of microwaves to rotate about the corresponding axis. For example from the initialised, spin-polarised state $|0\rangle$ the system can be driven fully to the $|1\rangle$ state.

ing field strength B_1, is typically referred to as the π-pulse length. As the pulse duration is extended further the rotation continues back through $|0\rangle$ and the frequency of these rotations, again dependent on the applied microwave power and B_1, is the Rabi frequency.

The labelling of states as in the two level Bloch description as $|0\rangle$ and $|1\rangle$ should not be confused with the spin projections $m_s = 0$, $m_s = +1$ and $m_s = -1$. The Bloch picture is used to describe the state of a two level system being driven by a resonant field - such as the ground state microwave transition between $m_s = 0$ and $m_s = -1$ or between $m_s = 0$ and $m_s = +1$.

2.3 Optically detected magnetic resonance

Astonishingly, it is possible to manipulate a single spin in certain systems and to read out - probabilistically - its spin state[64]. Repeated experiments and measurements performed on a single spin can be treated as sampling a statistical ensemble equivalent to a population of many such spins, assuming ergodicity.

In systems where the spin state can be read out via optical transitions this can allow spatial localisation of individual spins which are spaced more than a few hundred nanometres apart - enough to be optically resolved using CFM. With the caveat that only the population projection of the spin state can be read out optically, most of the pulsed EPR experiments developed for use on ensemble spins can be used on individual spins - although the interpretation may be different.

The NV^- colour centre in diamond is a great example of such systems demonstrating sensing and in particular magnetometry[109–113] down to the molecular scale with single NV^-.

2.3.1 Pulsed optically detected magnetic resonance

Using a combination of laser pulses and microwave pulses, pulsed EPR experiments can performed on single NV^- or an ensemble of NV^- and the spin projection of their final state can be measured optically using the spin state dependent contrast. In contrast to conventional pulsed EPR only the spin state projection is read out rather than a complex valued state in quadrature. This can be arranged by adding a final microwave pulse to project the measurement required into a real population. By integrating the initial fluorescence over many “shots” with the same timings and pulse parameters

Figure 2.16 the time averaged population of the final state can be measured (normalised by the integral of the spin-polarised emission). In the initial few hundred nanoseconds of illumination, the probability of emission of any photons is lower in the $m_s = \pm 1$ spin states and this is apparent as a suppression of fluoresence. Conversely, if the state at read out is $m_s = 0$ then fluoresence will be initially have a higher probability of emission. Over time the spin-polarising inter-system crossing path ensures that in either case the final state is $m_s = 0$ and the system is spin-polarised in preparation for this next "shot".

By alternating the final projection pulse of pulsed ODMR experiments to invert one read out phase common noise can be removed by looking at the difference between the two phases. The change in the initial fluorescence of these pure states - using data from the first, zero delay data point of an alternating Hahn echo experiment - is clearly visible at the start of the accumulated fluoresence signal. From the excited state, the "dark" $m_s = \pm 1$ spin state has a high rate of ISC into the singlet state. The excitation laser pulse excites the spin conserving optical transition from the ground to excited triplet states but in the $m_s = \pm 1$ case after few or no optical transition cycles the ISC transition "traps" the system for the lifetime of the singlet state before decaying through a spin-polarising mechanism into the $m_s = 0$ ground state. The rate of ISC from the $m_s = 0$ excited state is non-zero so from either state the emission rate settles to slightly less than the initial $m_s = 0$ state maximum fluorescence after ~250 ns.

The laser pulse is sustained for a few microseconds so that the steady-state fluorescence can be used for normalisation and to initialise the system for the next experimental "shot". Astonishingly in a few microseconds NV$^-$ can be fully spin polarised - extraordinary compared to the fractional thermodynamic Boltzmann populations possible in most EPR and nuclear magnetic

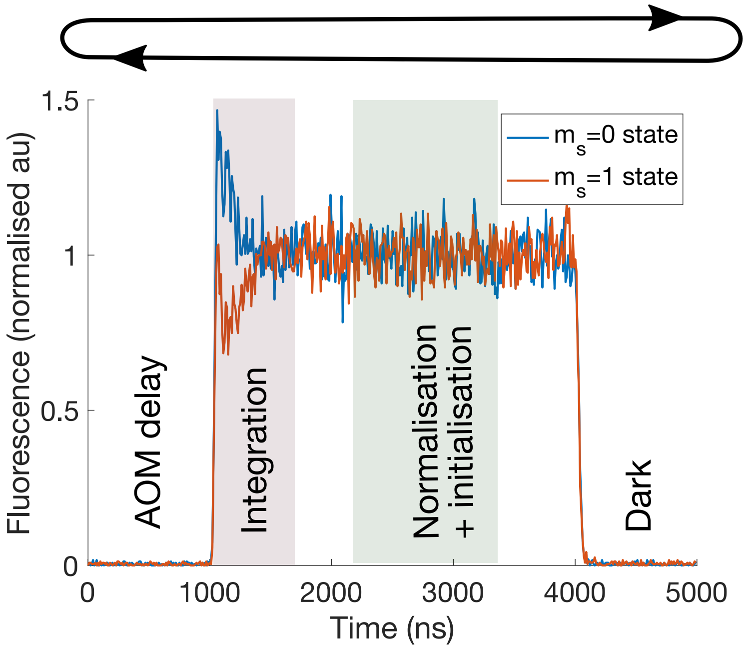

Figure 2.16: Examples of the signal data used for read out of spin state taken from data collected measuring the T_2 of a laser written NV^-.

resonance (NMR) systems. Once prepared, this spin-state will relax back towards the Boltzmann population but this classical spin relaxation rate is slow for NV^- with a lifetime (T_1) of at least milliseconds. In the dark, ample time is available to manipulate the spin state with microwave pulse sequences.

The quantum dephasing time for these spins (T_2) is shorter (∼650 µs for naturally occuring NV^- in diamond at room temperature) but refocusing pulses or isotopic purification can extend this significantly. The main limitation to the duration of these pODMR experiments is that any leakage of light whilst the excitation beam is "off" can reset the spin state. (This problem will be addressed in Section 3.4.1).

For the majority of experiments microwave power was applied to yield a Rabi frequency of 6 MHz to 8 MHz was used, however reducing the applied power by factors of 6 dB shows the period doubling as we would expect with a halving of B_1 in the rotating frame Figure 2.17. Under automated operation, these measurements were performed and fitted programmatically with the extracted parameters such as π-pulse length used to configure subsequent steps. The pulse sequences used for spin echo lifetime (T_2) measurements are shown in Figure 2.18 and Figure 2.19.

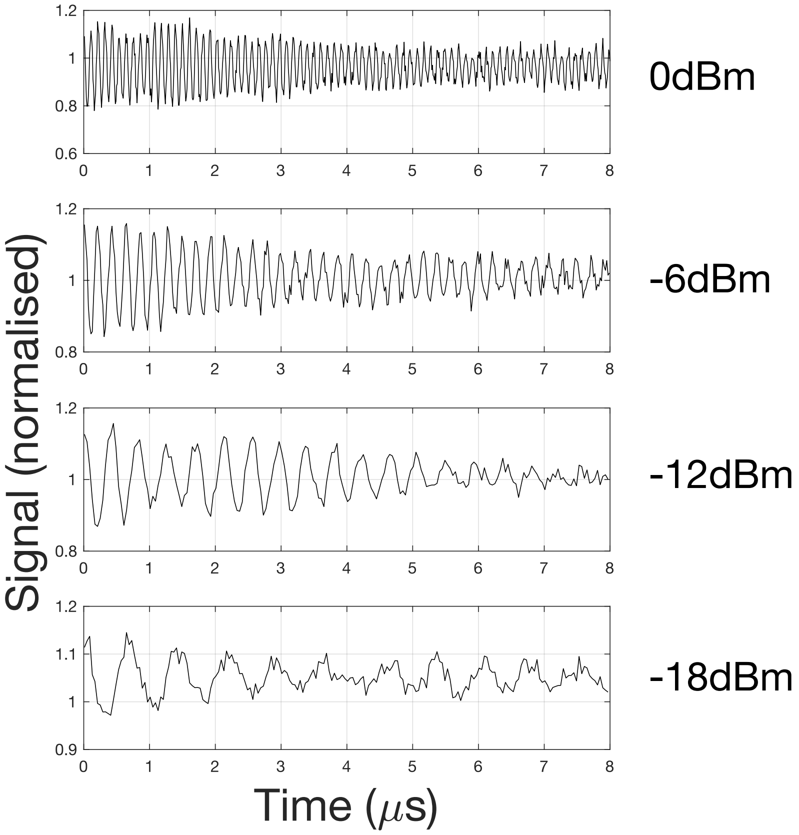

Figure 2.17: Rabi oscillations of site NV2 with microwave power. As power delivered to a single NV^- site is lowered in steps of 6 dB (i.e. quartered) the period doubles.

The Hahn echo pulsed ODMR experiment Figure 2.18 shows the difference between decoherence and classical spin relaxation. Classically, in the presence of a periodic, time varying magnetic field, such as those produced by nuclear and electron spins in the local environment precessing in an applied magnetic field, the paramagnetic spins will precess in a difficult to predict manner in the rotating frame. In an ensemble of spins, inhomegeneity in the rate of precession will cause the net magnetisation to decay with lifetime T_2* as they fall out of phase. Time evolution of a single spin system in such a field has an analogous result and a superposition state will precess in the Bloch sphere under the influence of local fields. The state can be projected into a population with a $\pi/2$ microwave pulse and optically read out as described above and averaged over many experiments. Simply waiting for various time delays before read out results in a Ramsey experiment, the envelope of which yields the lifetime T_2* from the inhomogeneity of conditions between experimental shots.

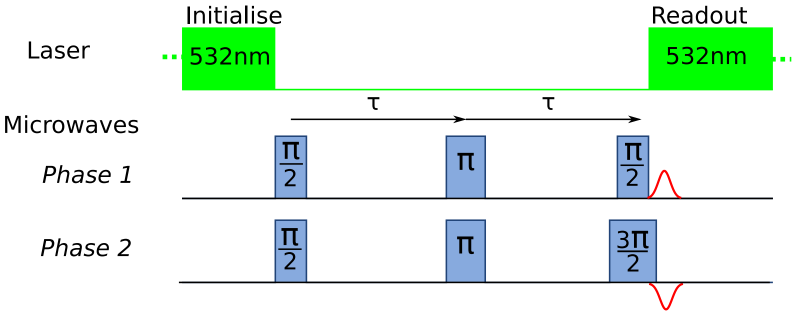

Figure 2.18: The Hahn echo pulse sequence, as used to measure spin coherence lifetime (T_2) by incrementally increasing time τ. Subtracting the two phases helps to eliminate artefacts in the readout process. The quantum information must endure to form the echo so the T_2 is given by 2τ.

Unlike classical spin relaxation T_1, or inhomogeneous broadening T_2* this dephasing is potentially reversible as long as quantum information has not been lost through interactions. If the local time varying field can be "rewound" then the original state can be recovered. This can be acomplished by inverting the spin state with a π "refocusing" pulse so that the periodic, time varying environment is seen in reverse Figure 2.18. This miraculous partial recovery of spin-polarisation is known as a Hahn echo. The decay in the amplitude of the echo gives a measurement of T$_2$, the quantum coherence lifetime.

One might suppose that this process could be repeated and this is essence of “dynamic decoupling” pulse sequences which act to preserve quantum information from the interaction with the environment with trains of refocusing pulses. XY-8 is one such sequence which reduces the effect of accumulated pulse imperfections by alternating the phase of the pulses in a palindromic unit of eight pulses. This unit can be repeated n times which is referred to as XY8-n.

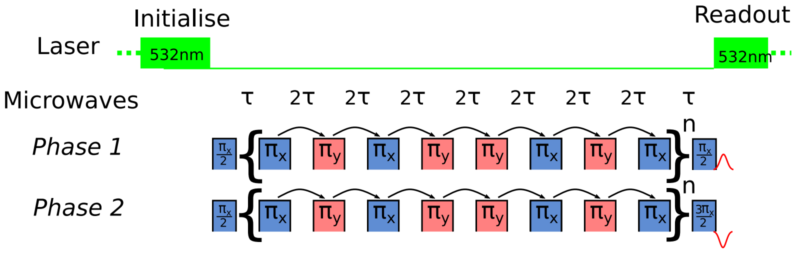

Figure 2.19: The XY8-n pulse sequence. Again, two phases of echo amplitude are measured and the difference is reported. Four of these repeated units were used in this experiment (XY8-4) and T$_2$ is the coherence lifetime after 32τ.

In addition to prolonging the lifetime of quantum information, the period of dynamic decoupling can be chosen to accumulate the influence of interactions occuring at that frequency. This is the basis of sensing with dynamic decoupling sequences and is somewhat analogous to using individual spins as a quantum “lock-in amplifier”.

2.4 Laser writing in diamond

2.4.1 Development of the technique

The laser writing process used in this work was developed by Martin Booth, Richard Simmonds and Patrick Salter[33]. They applied an adaptive optics technique developed for imaging in a biological context to correct the wavefront of 100 fs infrared pulses for the depth dependent spherical aberration introduced by the known refractive index mismatch at the surface of the high refractive index diamond. With this correction applied, the intensity in a small, localised volume is instantaneously sufficient to dislodge atoms in the diamond lattice producing vacancies and other "damage". This highly non-linear process can be controlled to create graphitized, conductive "wires" inside diamond[29, 114, 115], strain induced waveguides[116, 117] and even ensembles of vacancies at predetermined positions[28].

2.4.2 Laser writing of vacancies

Ensembles of vacancies in the diamond lattice can be generated by direct laser writing, as illustrated in Figure 2.20. A single pulse from an ultrashort laser is focused tightly beneath the surface of the diamond. The light matter interaction is highly non-linear, limiting any material modification to the focal volume and giving an inherent three-dimensional resolution to the fabrication[31]. By careful tuning of the laser pulse energy, it is possible to access a regime where Frenkel defects are generated at the focus without any further discernible disruption of the crystal lattice[28]. The dimensions of the laser focus inside the diamond are theoretically estimated to be 350 nm radially and 1.7 µm longitudinally as the full width half maximum of the intensity distribution. Given the high degree of non-linearity in the process, the expected dimensions over which the light-matter interaction is appreciable are likely to be much lower.

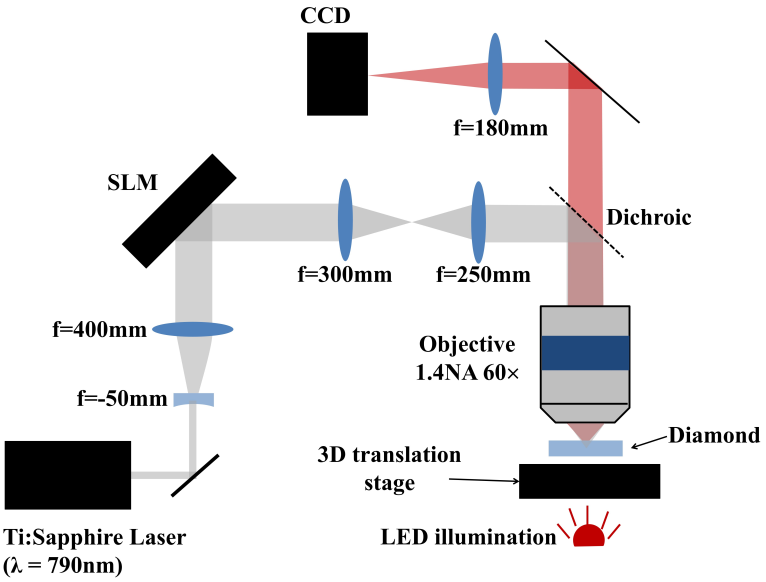

Figure 2.20: Schematic diagram of the aberration corrected laser writing system[28].

Since the laser writing process is known to be highly non-linear[34], small changes in the pulse energy can greatly change the number of vacancies produced. In order to find the fine range of pulse energies to use in these experiments, an initial calibration study was carried out on the same fabrication run inside a nominaloly identical diamond by writing arrays of points across a coarse range of pulse energies. This sample was subsequently characterised using a scanning confocal microscope, to find the pulse energy that produced vacancy ensembles with just detectable photoluminescence. Previous work has shown that write-pulse energies slightly lower than this are optimal for NV^- creation[28].

These vacancies can potentially be converted to N-V centres by annealing at 1000 °C for three hours[28]. Above 600 °C vacancies become mobile[46], diffusing at a temperature dependent rate. The activation energy for mobility and dissociation of different colour centre complexes in diamond differ so by choosing an annealing temperature that is not too hot and not too cold vacancies can be captured: by aggregation with other vacancies to form divacancies and vacancy clusters, by surfaces/dislocations or crucially by encountering an impurity such as substitutional nitrogen atom to form the N-V complex. Above ~1150 °C subsitutional nitrogen starts to aggregate[46]; above ~1300 °C N_2V starts forming and at ~1400 °C the N-V complex starts being converted to other complexes. In addition to formation of the N-V complex, it is desirable for any long vacancies to aggregate to reduce strain in the lattice and to eliminate charge traps which reduce the coherence time of NV^- by interaction with unpaired electrons. The technique has now also been applied to generating colour centres in silicon carbide[36]. This work demonstrated a remarkable method for generating single NV^- in pre-determined positions in diamond - however questions remained to be addressed in further work to better understand how to control the process, detailed in the work covered in Chapter 4.

In parallel to the work described in this thesis, a “repeat until success” process with in-situ annealing was developed to create single NV^- with near unity yield[36] (which used characterisation techniques developed in this work).

2.4.3 Other comparable techniques

Creation of determinstically placed NV^- has been sought by numerous processes. Ion implantation[48, 56, 118, 119] is perhaps the most common method of creating single NV^- [48, 87, 120–128] or coupled pairs of NV^- [129] in natural isotopic abundance and ^{12}C enhanced material (coupling ^{13}C nuclear spins is the mechanism for decoherence that limits the T_2 of “as grown” single NV^-). Large arrays of NV^- sites have been created using masks[130]. The vertical precision of this technique can be improved by δ-doping a thin nitrogen layer during growth by CVD[87, 126, 127, 131–133]. The basic method of control of the number of NV^- produced and their depth is by implantation energy and dosage[134] however typically each site has an ensemble of NV^- and the damage introduced can restrict the coherence time. NV^- colour centres have been created with high lateral precision in a thin δ-doped layer of nitrogen using transmission electron microscopy (TEM) to introduce vacancies[133], or electron beams to locally anneal[135], by accelerating ions with SEM[136] as well as with lithographic nano-masks[137, 138]. Advances in fabrication of photonic structures with direct laser writing are continuing apace[139]. Groups are also working on integrating fabrication of NV^- with photonic structures[138, 140, 141]. Charge state control of shallow NV^- [142] has been demonstrated by controlling the Fermi level with surface termination & gate electrodes[94, 143, 144] and otherwise with ensembles[145, 146].

2.5 Quantum Optics

2.5.1 Single-photon emission

Whilst NV$^-$ colour centres have applications for classical sensing context as ensembles of many emitters at large and small scales, they also give access to the non-classical quantum state of individual colour centres. A single NV$^-$ centre can only emit one photon at a time - or more specifically there is a minimum time between the emission of photons by a single NV$^-$ centre. Such systems are known as single photon emitters and NV$^-$ can be a convenient single photon source[147, 148]. Other examples include single molecules and quantum dots. Parametric downconversion can also be used to produce pairs of photons which may be used as “heralded” single photon sources.

The photons emitted by such sources are directly connected to the state of the emitting quantum system. In the context of QIP and quantum key distribution (QKD) if the colour centre state encodes a quantum analogue of a digital bit - a qubit - such photons can be considered “flying qubits”. Only photons which are emitted by the qubit are relevant and other photons constitute noise that cannot be dismissed with a longer sampling time in a non-classical experiment.

There are differences in the measurable properties of such non-classical number or Fock states (typically represented as $|n\rangle$) from classical light fields such as the coherent state (typically represented as a $|\alpha\rangle$) of a laser - even at intensities low enough to detect “single” photon arrival events with an avalanche photodiode (APD). The mean photon count rate can be the same for both however the uncertainty in the count rate for an ideal single photon source is zero (with no information on quantum phase) compared to a classical $\sqrt{n}$. In practice, there is some experimental noise from unavoidable “dark counts” in the APD and with NV$^-$ both shelving in the ISC path and photo-ionisation can interrupt emission. These processes dominate the variance of the detected count rate however the emission characteristics can be distinguished experimentally by measurement of the normalised second-order quantum coherence of the light with itself, the normalised intensity auto-correlation Eqn. 2.5[4]

$$\gamma^{(2)}(\tau) = \frac{\langle I(t)I(t+\tau)\rangle}{\langle I(t)\rangle^2} \tag{2.5}$$

more correctly expressed in terms of the quantised modes of the electromagnetic field for the non-classical behaviour [149]Eqn. 2.6

$$\begin{aligned} g^{(2)}(\tau) &= \frac{\left\langle E^{(-)}(t)E^{(-)}(t+\tau)E^{(+)}(t+\tau)E^{(+)}(t)\right\rangle}{\left\langle E^{(-)}(t)E^{(+)}(t+\tau)\right\rangle \left\langle E^{(-)}(t+\tau)E^{(+)}(t+\tau)\right\rangle} \\ &= \frac{\langle : I(t)I(t+\tau) : \rangle}{\langle I(t)\rangle^2} \end{aligned} \tag{2.6}$$

using $\langle :: \rangle$ to indicate normal ordering by application of the commutator $aa^\dagger = 1 + a^\dagger a$.

For large τ, $g^{(2)}(\tau)$ approaches 1 as for the uncorrelated photon arrival times of classical coherent light. However at $\tau = 0$, $g^{(2)}(\tau)$ drops to zero for an ideal single photon source. In reality this “dip” is not a zero-width delta function as the excited state has a finite lifetimes which can be extracted by fitting to an appropriate model. The NV$^-$ system is effectively a three level system with a short ^{3}E lifetime and a long ISC lifetime. The “dip” is evidence of photon anti-bunching - arrival of a photon at one detector precludes a photon arriving at the other detector. The variable delay introduced by the “shelving” process produces a positive correlation for slighty longer delays

---

[4] shown in its classical form for simplicity here, however the Cauchy inequality implies $\gamma^{(2)}(\tau) \leq \gamma^{(2)}(0)$

which decays exponentially to the uncorrelated norm with the lifetime of the shelving state.

The HBT experiment[150] used to measure the auto-correlation of photon arrival time, which is proportional to the probability of a photon arrival event at time $t + \tau$ given a photon arrival event at time t.

To use these photons in the difficult work of composing larger quantum systems they typically need to be indistinguishable (in the context of that experiment) and from single sources. Extraneous photons and photon losses decrease SNR which is critical for single-shot readout experiments[151] and entanglement[11, 152]. The non-classical nature of these individual measurements sets a minimum threshold which cannot be replaced by more measurements. A significant indicator of low detection noise is that, after collection of 10^6 photons, $g^{(2)}(0)$ approaches 0, showing that few uncorrelated photons are being detected.

$g^{(2)}(0)$ can also be used determine the number (N) of single NV^- emitters present for small N as $g^{(2)}(0) \leq 1/2$ indicates a "single" ($N = 1$), $1/2 < g^{(2)}(0) \leq 2/3$ a "double" ($N = 2$), $2/3 < g^{(2)}(0) \leq 3/4$ a "triple" ($N = 3$) and so on.

From a quantum optics perspective, the Mandel Q parameter[153] can be calculated from $g^{(2)}(0)$ as $Q = \langle \hat{n} \rangle \left(g^{(2)}(0) - 1 \right)$ where $-1 \leq Q < 0$ represents sub-Poissonian statistics. Losses of quantum efficiency η_i such as the numerical aperture (NA) of the objective and sensitivity of the detectors can be applied to the Mandel Q parameter simply as $\prod_i \eta_i Q$. As losses accumulate, the single-shot Mandel Q parameter approaches zero and classical Poissonian photon statistics. The accumulated $g^{(2)}(0)$ measurement can be used as a convenient test that a single photon emitter (SPE) is isolated and photo-stable (frequent charge state switching would introduce a higher "background" of uncorrelated photons).

The ideal photon emission rate of a single NV$^-$ can be estimated from the lifetime of the excited state (~10 ns). Of this 100 Mc s^{-1} only of the order of 100 kc s^{-1} are detected unless techniques such as solid immersion lenss (SILs)[154] or bullseye gratings[155] are used to ease the transition of light out of the high refractive index diamond.

2.5.2 Single-shot readout vs room temperature ODMR

No single-shot read out is used as yet in this work, however both the low-temperature confocal microscope and fabrication of high quality NV$^-$ in determinstic locations are steps towards applications in QIP so I will briefly outline what such measurements involve.

Pulsed ODMR experiments aggregated over many repetitions are effective for repeatable measurements however experiments that require single-shot readout as a quantum mechanical measurement must use higher fidelity readout techniques, such as those based on PLE, for readout at liquid helium temperatures[151] although a range of techniques have been used[156] such as introducing an optical cavity[61, 157] to restrict the density of states around the colour centre to enhance ZPL emission. By selectively exciting a single transition, on resonance at low temperature and improving collection efficiency with techniques such as SILs[158], the higher fidelities required for entanglement by observation can be achieved. The properties of the NV$^-$ such as the coherence lifetime and other spins in the local environment are the same however non-resonant excitation experiments are considerably less complex and can be performed at room temperature without fabrication of SILs.

Chapter 3

Low temperature confocal microscopy

3.1 Aims and requirements

The initial outline for the low temperature (LT) fibre coupled (FC) CFM or (LT-FC-CFM) was motivated by the idea of using sparse nanodiamonds containing single NV$^-$ to couple to and hence read out the spins of individual phosphorus donor atom electrons in phosphorus doped silicon (Si:P). Donor atom spins in silicon have been shown to have excellent coherence properties at low temperatures, particularly in isotopically purified silicon. Schemes have been proposed to build arrays of qubits by combining hydrogen lithography techniques to grow in donor atoms in controlled locations.

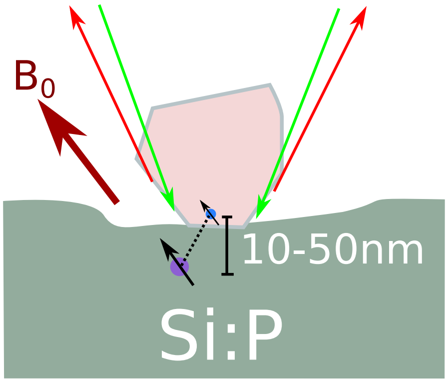

Figure 3.1: Nanodiamonds as single-spin NV$^-$ sensors on the surface of phosphorus doped silicon. An ambitious goal to entangle NV$^-$ with single dopant atom electrons, stretching the range for dipole-dipole interactions. This case motivated the capabilities the system would need.

In principle, nanodiamonds scattered on the surface could bed into any small irregularities in the silicon surface better than a membrane and possibly bring the NV$^-$ and phosophorus spins close enough together to interact Figure 3.1. However, this is an ambitious goal even supposing an NV$^-$ is brought within tens of nanometres of a donor atom - a long distance when dipole-dipole interactions drop off proportional to $^1/_{r^6}$.

In the proposal's favour, silicon and diamond can be ideal systems for the study of solid state, isolated spins with good coherence properties. Particularly in their isotopically purified forms electron spin coherence times in both systems can be exceptional[73, 89, 159]. Nuclear spins can also be used as a resource for sustained "memory". The sparsity of other miscellaneous undriven spins to cause decoherence gives the states time to be read out. In the interim, attempting to detect any other spins Figure 3.2 from a single NV$^-$ nanodiamond would be worthwhile and the platform opens possibilities for testing quantum sensing protocols, noise spectroscopy and spin relaxometry[20].

Based on this proposal, the requirements were taken to include:

- Fluorescence imaging in 2-d plane to identify nanodiamonds.
- A magnetic field of 5 mT to 20 mT along the NV$^-$'s symmetry axis (arbitrary orientation).
- A scheme to optimise the orientation of the magnet field within 1° to 2°.
- continuous wave optically detected magnetic resonance (cwODMR) to find the EPR resonances.
- Delivery of nanosecond long microwave pulses to the NV$^-$ at around (2.9 ± 0.4) GHz.
- Very low excitation light leakage to minimise decoherence by optical electron-hole pair creation in the silicon substrate.
- High collection efficient for fluoresence light from only the site of interest.
- Control of excitation light polarisation to align with NV$^-$ dipoles efficiently, ideally automated.
- Low temperature operation (4 K).

- Second frequency RF control of other "$g_e \sim 2$" spins and nuclear spins.
- Automatic focus optimisation on single colour centres, with tracking.
- Capability to upgrade to PLE and single-shot read out.
- Adapatability to also study other colour centres such as SiV^0.
- Software for manual control based on two-dimensional imaging.
- Automotation of site evaluation to find suitable candidate sites if they are rare.
- Identification of particular nanodiamonds for characterisation.

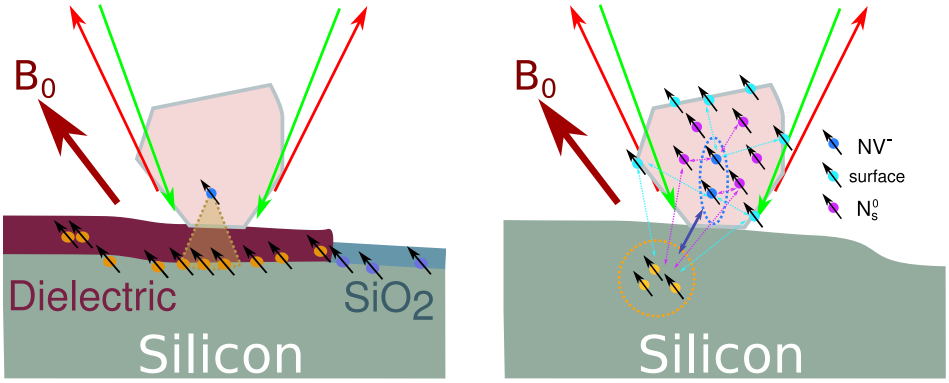

Figure 3.2: NV^- in nanodiamonds could also be used as a nanoscale single-spin sensor *(left)* for noise spectroscopy of defects at material boundaries in semiconductor oxide and dielectric layers. Investigation of photoexcitation and recombination at grain boundaries in potential solar cell materials would also be of interest. *(right)* Sensing with small ensembles of NV^- would also be of interest, as would shorter range entanglement with spins on the surface of nanodiamonds or sensing through coherent clusters of substitutional nitrogen spins[82].

3.2 Confocal fluorescence microscopy

In a CFM, light is collected from one point at a time. Conventionally, the field is restricted by focusing the image through a small pinhole which rejects light not originating from the small volume in the sample plane which is conjugate to the pinhole. In commercial confocal microscopes one of several pin holes can often be selected to adjust the trade off between light collection and spatial resolution. When a microscope is focused on a point light source, the image in the focal plane is an Airy disc - the Fourier transform of a circular aperture. The size of the image is determined by the magnification of the objective and tube lens so optical units (o.u.) or Airy units (AU) are often used as dimensionless parameters with respect to the first minimum of Airy disc. The choice of pinhole aperture with respect to the Airy disc diameter controls the restriction of light to and from the focal point of the system. Choosing a pinhole of size 1 AU will allow the central, near Gaussian peak of the Airy disc to pass with some exclusion of light from nearby sources. A modest resolution enhancement over the diffraction limit can be obtained by using a smaller pinhole, say of diameter (0.5 AU) with a commensurate reduction in the light collected as the central bright peak is clipped. As we anticipate sparse single NV^- resolution gains are secondary to light collection efficiency. An effective pinhole diameter of 1.5 AU to 2 AU wide will collect 89-91% of the light from a point source, compared to 84% from a 1 AU pinhole or 59% from a more restrictive 0.5 AU pinhole Figure 3.3. Light from nearby sources is still excluded.

The focal volume is three-dimensional and the distribution of intensity is referred to as the point spread function (PSF). Axially, this distribution is a sinc function with the central maximum extending around twice the size as

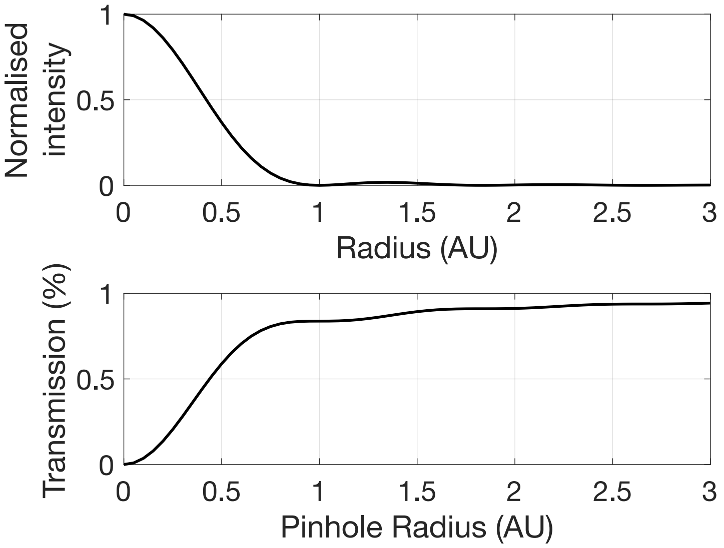

Figure 3.3: *Top*: A light beam that has passed through a circular aperture and been focused with a lens forms a radially symmetric image known as the Airy disc. The radial intensity distribution can be described with a Bessel function in form shown with the peak intensity I_0. The absolute radius of the first minimum will depend upon the magnification of the microscope as determined by the objective and tube lenses so it is common to normalise the radius relative to the first minimum. *Bottom*: The proportion of the incident light that passes through the pinhole can be calculated as the integral of intensity over the pinhole. The effective pinhole size relative to the first minimum of the Airy disc controls how much of the incident light is rejected for a given pinhole and magnification.

the radial Airy disc maximum. The volume around the central maximum is approximately ellipsoidal.

In a fluorescence confocal microscope, the signal at a point is controlled by the convolution of the excitation light PSF and the PSF of the image of the detection pinhole. Either or both can be used to restrict the volume being probed. Overlapping these two ellipsoidal volumes is the most critical step in aligning a CFM.

In lieu of a pinhole, the mode field diameter (MFD) of an optical fibre can be used effectively as both pinhole and waveguide (although care should be taken to discard light coupling into the fibre cladding). As the pinhole size cannot be varied, the tube lens can be chosen to control the magnification of the microscope and hence the fraction of the light collected.

3.2.1 Attocube fibre coupled CFM

Originally a system was purchased from Attocube as a fibre coupled confocal microscope with a single lens objective at the end of a 1.3 m long probe for insertion into a cryostat. The single lens used a specially machined casing to couple light into a bare single mode optical fibre with a MFD of approximately 3 µm which was used to be used both to supply excitation light and to collect emitted or reflected light. This would have been effective for confocal reflection imaging or excitation of some other fluoresence systems such as quantum dots but the lack of any correction for chromatic aberation has several major drawbacks when used for excitation of NV^-.

Green excitation (with wavelength around 530 nm) is commonly used for non-resonant excitation of NV^- for its efficient absorption and for charge stability. Fluorescence is also more easily isolated in a non-resonant scheme. This leads to the first problem, if the focusing optics have signficant chromatic aberation. The original Attocube fibre coupled objective lens had a chromatic shift between the green and red focal depth of $\sim$ 100 µm. For any confocal microscope, it is crucial that the PSF of the excitation and fluoresence volumes overlap - essentially rejecting the contribution from regions outside the overlap of the two PSF of the effective pinholes. For an objective with an NA of 0.82 this is approximately a depth range of no more than 5 µm. In this system the pin hole is in effect the MFD of the single mode fibre, which is a fixed point shared between both excitation and detection paths with a narrow-band fibre beam splitter outside the cryostat separating the light. There is negligible overlap between the excitation and detection focal volumes.

The chromatic aberation is also problematic with the broad emission spectrum of the NV^- even at 4 K. Emission in the phonon sideband is spread from 600 nm to 900 nm which necessitates the use of achromatic optics. An achromatic doublet may reduce the chromatic shift over this range slightly however the focal volumes still would not overlap. Apochromatic corrected optics are available - however a conventionally bonded multi-element microscope objectives will normally fail at cryogenic temperatures due to the differential expansion of the glasses.

3.2.2 Free-space & fibre coupled CFM

A low temperature apochromatic free-space microscope objective was obtained from Attocube with chromatic shift of 1 µm across the range however this necessitated adapting the probe to replace the low temperature fibre coupling with a more complex room temperature fibre coupling on top of the probe, outside of the cryostat.

In order to study samples at stable cryogenic temperatures, the sample stage and microscope objective are mounted on the end of a cryostat probe. The original probe was supplied by Attocube for a fibre coupled, single wavelength, cryogenic confocal microscope. This was modified to replace the directly fibre coupled aspheric lens with an free-space Attocube cryogenic apochromatic objective and to open a path to an optical system outside the cryostat. To minimise the optics required on the top of the probe the detection and excitation systems are implemented on an optical bench and fibre coupled to the probe once it is installed in the cryostat. Conventional confocal microscopes use pin holes to restrict the excited volume and/or the detection volume. In this fibre coupled confocal microscope, optical fibres double as the excitation and detection pin holes. A single mode fibre, polarisation maintaining (PM) fibre is used for the excitation light - delivering a single mode 532 nm, collimated beam to the back aperture of the microscope objective. A multi-mode 50 µm fibre is used as the detection pinhole with an achromatic doublet f=100 mm, producing a magnification of around ×40. The 50 µm MFD of the fibre acts as a 1.5 AU pinhole. (Similar performance was found with a low-powered "Fluor" corrected objective and a single mode fibre).

3.2.3 Dichroic optical module

Light to and from the low-temperature compatible infinity corrected objective at the bottom end of the probe passes through a system of optics in the head unit Figure 3.4 which can be affixed or modified with the sample in the cryostat. A dichroic mirror is used to separate the "red" fluorescence from the NV^- from the green excitation light.

In principle, this fibre coupled head unit could be replaced for work with other colour centres or for resonant excitation. Additional arms could also be introduced to add excitation beams. The removable camera beam splitter, which has a limited field of view of tens of microns due to the length of the probe, is invaluable for alignment. A 3-d printed light ring of Optek OVLEW1CB9 white LEDs around the back-aperture of the objective (potentially operating at cryogenic temperatures[160]) passing high-angle, out-of-focus white light through the objective to light the sample.

Working with the microscope objective in the cryostat, this module is central to the confocal microscope however as much as possible of the excitation light control and photon counting are performed on the optical bench, connected by optical fibres.

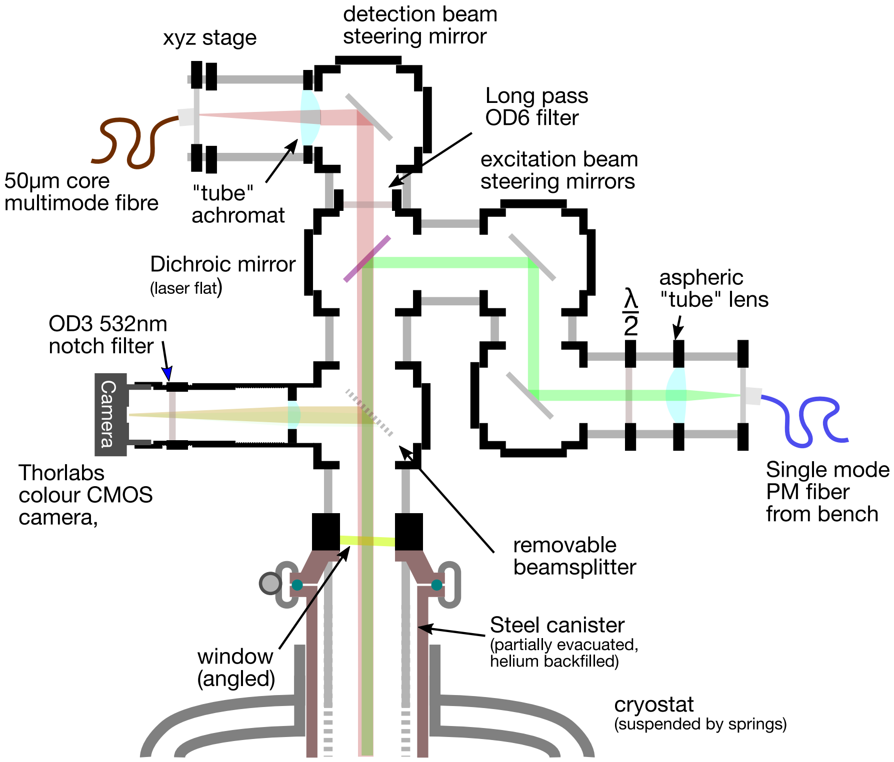

Figure 3.4: The central optics of the confocal fluorescence microscope are constructed in an extension to the 30 mm cage system atop the probe. These include a dichroic mirror to separate the green excitation and red fluorescence light, filters to eliminate any remaining scattered light not emitted from the NV^-, steering mirrors to align the two beam separately, a camera to see wide-field context and the optical fibres that act as input, output and define the confocal volume by acting as pinholes.

3.3 Detection hardware

3.3.1 Single photon counting modules

A pair of near-infrared (NIR) optimised fibre coupled Excelitas SPCM-850-13-FC photon counting modules with a dark count of $250\,\mathrm{c\,s^{-1}}$ were used for detection through a 50 µm multimode 50-50 fibre beam splitter ($(633 \pm 40)\,\mathrm{nm}$). The modules and splitter are boxed in to a compact aluminium hutch and the detected light is transmitted to the hutch with an opaque steel clad fibre (either 50 µm core multimode or single mode depending upon detection optics). Without cladding, the detection of even subdued and colour restricted room lighting contributes a significant rate of counts.

3.3.2 Attocube imaging hardware

The initial outline for the project was to use Attocube hardware and software to quickly establish a working system with minimal home-built hardware or software. Similar systems have been used successfully in work with quantum dots so purchasing a system rather than building seems reasonable.

The system included a proprietory hardware imaging scanner console (ASC400) and associated software (Daisy). This supported at least imaging operations and, on installation, reflection-mode monochromatic confocal imaging of a high-contrast test sample with at least micron scale resolution was demonstrated at cryogenic temperatures.

Regrettably, as the implementation of experiments with NV^- was developed a number of obstacles were encountered which required additional hardware development, integration work and eventually development of replacement systems. These included:

- Persistent intermittent hardware failures

- Inextensible software
- No support for low intensity fluoresence imaging
- No external hardware or software triggers
- Only analogue voltage signal input

Initially, a hybrid system with hardware and software was designed and partially built to add the required functionality. This was approached as solving problems in turn to achieve:

1. High count rate, ensemble fluoresence imaging
2. High count rate, ensemble ODMR
3. Single-emitter sensitive fluoresence imaging
4. Confirmation of single-emitter detection by HBT
5. Single-emitter ODMR
6. Pulsed ODMR on single NV^-

Detailed planning for advanced dynamic-coupling pulsed ODMR experiments[161–163], sensing protocol refinements[8, 107, 164] and to support resonant excitation experiments on single centres was deferred at this stage however an outline of their requirements was considered to support such extensions. Allowances included provision for replacing the optics unit on top of the cryostat, support for a secondary RF antenna and a capability to top up the cryostat with liquid helium during long pODMR experiments.

External software Section 3.5 was developed to control a Keysight microwave source, so that once NV^- sites were identified ODMR could be performed on them using the discrete counts provided by the photon counting hardware synchronised with the steps of a microwave frequency sweep. This path was complicated by the difficulty of triggering and sequencing events between the Attocube software, hardware and the external hardware. Coordination was slow, indirect or impossible.

To record the 20 ns single-photon counting module pulses a low-cost PicoScope 3000 series digital oscilloscope was found to be just fast enough to register the pulses of arriving photons through its digital port (with the addition of external 50 Ω termination). Software was developed to as efficiently as possible retrieve data from the large memory buffer on this device. Regrettably, insoluble problems emerged with this approach. Whilst the device could sample the input from the photon counter modules fast enough, the data could not be aggregated on the device in a suitable way and a prohibitively large amount of data - a complete 8-bit oscilloscope trace at 10 ns resolution - had to be transferred to the host computer for processing, at the data rate of USB. A multi-frame triggered capture mode would allow batches of pulsed ODMR experiment shots to be recorded and transferred back to the host - but at the cost of signficant idle time between transfers as the device could not continue to record data whilst transferring to the host. This would slow down data acquisition but did not prevent pulsed experiments inherently.

We decided not to use National Instruments data acquisition hardware with LabView based on the experience of other groups who had struggled to incorporate coordination of the complexity of these experiments in LabView and Matlab. We also had concerns of vendor lock-in, the problems that can occur over time with platform upgrades and the difficulty of change tracking. In retrospect these concerns did not necessarily apply to NI hardware - direct access to the hardware application programming interface (API) is less obscure than it seems on first inspection once some terms are understood.

To provide real-time photon count rates for imaging and cwODMR, a microcontroller based system was designed and built by David Greenshields in the departmental electronics workshop to integrate the pulses from the two photon counter modules and produce both a discrete photon count and an analogue voltage, suitable for the ASC400 analogue to digital converter (ADC) to digitise again for APD fluoresence imaging. Integrating this information into imaging with the ASC400 and Daisy was further complicated by the lack of any external trigger support to synchronise the start of a scan or of moving between pixels of the scanner image with the integration of count rates.

The locally-built microcontroller device was designed to produce count rates and not also photon arrival time information or the means to synchronise data acquisition on nanosecond timescales. The time resolution of the PicoScope based solution was potentially fast enough to perform an indicative HBT but a shared lab time-correlated single photon counting (TCSPC) system (PicoQuant PicoHarp 300) could be used with stand-alone software to confirm the presence of a single-photon emitter.

At this point, persistent hardware failures were the last straw for integrating this system on top of the Attocube ASC400 and Daisy software and the decision was taken to return the scanning electronics hardware to Attocube and implement our own system.

3.3.3 Home-built imaging hardware

A microcontroller based voltage scanner was built by David Greenshields to replace the Attocube ASC400 system and software was developed in F$^\sharp$ on the Microsoft .NET framework for scanning confocal imaging using the synchronised direct counts from the microcontroller counter to acquire images. The system was also integrated with the Keysight microwave source to perform ODMR and partially integrated with the PicoScope data acquisition. The piezo stick-slip positioner stage was co-opted as a limited range focusing stage and an improvised trigger emitted by the ANC300 using an undocumented method allowed the microcontroller photon counter to capture depth sections for focusing.

Four data acquisition systems were in use for different purposes. A microcontroller to produce a count rate for imaging and ODMR; a PicoScope for pulsed ODMR acquisition; a shared PicoQuant TimeHarp for HBT and pulsed ODMR acquisition; an Andor single-photon spectrometer.

This system broadly worked to a point but as set out in Section 3.5 practical problems abounded. The problematic pulse sequence generation using the Keysight source was replaced by a Swabian PulseStreamer controlling microwave switches. Publication of University of Ulm's relatively complete Qudi system[165] and purpose built new hardware solutions by Swabian Instruments emerging from University of Stuttgart presented a potentially less risky path to a framework which provided the capabilities required. Successful migration of another confocal microscope paved the way and, with some regret at the time and effort invested, the F$^\sharp$ based system was migrated onto the National Instruments and Python based Qudi framework.

3.3.4 National Instruments, Swabian Instruments and Qudi

The core of the Qudi software system[165] has been built around acquisition by National Instruments (NI) X-series hardware for control and data acquisition at the API level so to minimize difficulties with transitioning between the systems the two microcontroller based systems were replaced by an NI 6323 PCIe card, break out panels and a new host computer with a larger case.

Whilst the NI 6323 card is only as fast as the PicoScope 3000, it has a huge advantage in being able to write to the host computer's memory a hundred times faster than over USB. It is also somewhat programmable and capable of aggregating data binned by triggers or corresponding to changing outputs in hardware. Offloading time-critical work to a subsystem greatly simplifies the work required on the host system.

The NI 6323 card is capable of fast pulse counting on one channel but it is not able to compare photon arrival time stamps or accumulate pulsed ODMR photon arrival time histograms. After some initial work to use the PicoQuant TimeHarp for this purpose, an field programmable gate array (FPGA) based Swabian TimeTagger was acquired which greatly simplified the implementation.

Several other features are required particularly for the Attocube system such as auto-focus without a z-axis scanner (Section 3.5.4), stepped movement with piezo-positioners (Section 3.5.4) and electromagnet control (Section 3.7) but these are detailed in the relevant sections.

3.3.5 Summary

At the start of this project, much of the hardware and software we use now was not available. In the course of the last two years, accessible FPGA based hardware has become available that is ideal for controlling experiments on nanosecond timescales. As a group, we also have acquired much more experience of what is required to build a pulsed ODMR confocal fluoresence microscope. An essential part of pulsed ODMR experiment data acquisition is close coordination of pulse sequences with photon arrival time recording and aggregation of this potentially overwhelming stream of data in hardware.

3.4 Excitation laser system

Pulsed ODMR experiments with NV^- use pulses of light some microseconds long to both initialise and read out the spin state of single and ensemble NV^-. A non-resonant excitation scheme is used in this system. A 532 nm laser source is ideal for exciting the absorption maximum of the phonon side band of the NV^- colour centre. However, between light pulses, leakage of high energy optical photons is undesirable as they have sufficient energy to "reset" the target spin by exciting electrons in the excited state into the conduction band and by changing the state of charge traps in the vicinity of the target NV^-. Where NV^- are being used for sensing spins in a silicon substrate these photons also have sufficient energy to excite electrons out of the valence band, creating electron-hole pairs.

In order to maximise the sensitivity of measurements with NV^- with the longest possible coherent evolution of the sensing spin in a consistent environment, reducing the leakage of green light during each repeated experiment shot to a minimum is worthwhile.

A common arrangement for controlling the light on these time scales is to use an acousto-optical modulator (AOM) to deflected the light. Typical contrast between "on" and "off" states with an Isomet 1250C AOM as delivered is 2000:1 so with a input power of 100 mW and diffraction efficiency of 80% the leakage could be as much as 40 µW. An alternative which can reduce the "off" state power to zero is to interrupt the electrical current in a laser diode, however intensity instability of light during the initial 100 ns to 300 ns of each pulse is problematic as this will reduce the contrast between the spin states in the initial readout.

This leakage of excitation light was reduced by two methods. Firstly

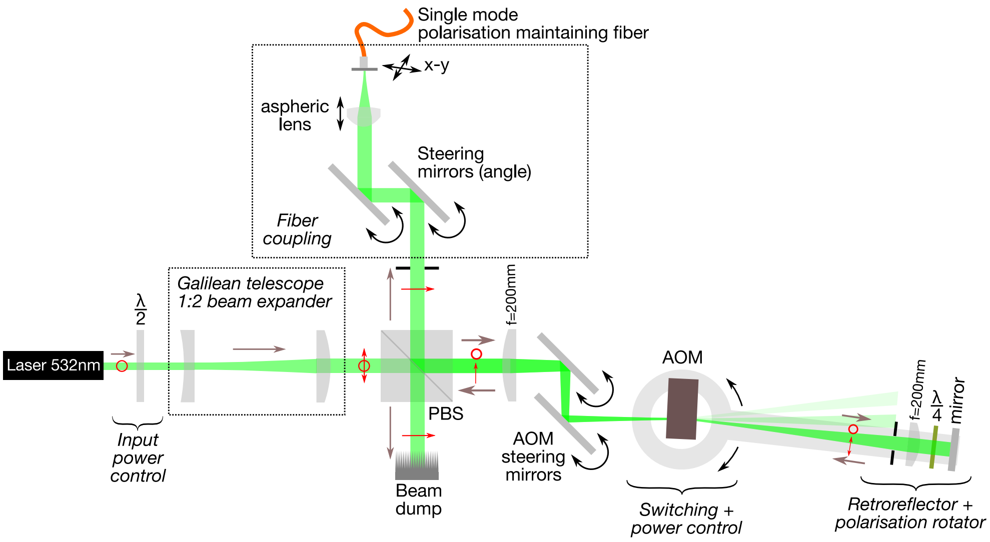

Figure 3.5: Fast rise time excitation light pulses with a high exclusion ratio and power control is implemented with a fibre coupled double-pass system.

the Isomet RF AOM driver limited the contrast and was replaced by a home-built RF driver with significantly higher contrast and dynamic power control. Secondly the light was passed twice through the AOM Figure 3.5, effectively squaring the exclusion without introducing synchronisation issues as with a second AOM Figure 3.6. Using a combination of these methods, light leakage was reduced to 40 nW. Using the home-built driver alone increased the T$_2$ coherence times that could be measured from tens of microseconds to milliseconds.

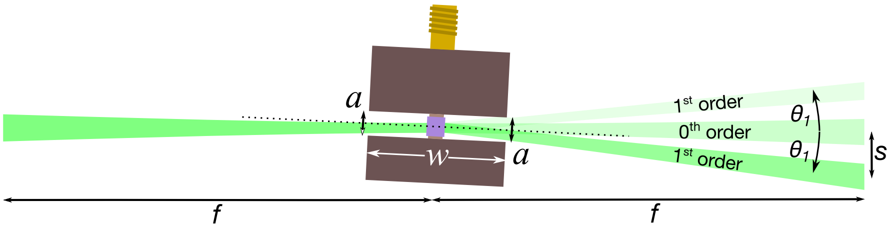

Figure 3.6: The Isomet 1250C acousto optical modulator has entry and exit apertures with diameter a=750 µm separated by w=22.34 mm. At 532 nm, the first order deflection angle marked as θ_1 is 29 mrad.

3.4.1 Home-built AOM driver

The standard Isomet AOM driver module still outputs a few milliwatts of RF in the off state (consistent with an implementation using an attenuating switch). This leakage resulted in transmission of tens of microwatts of excitation light during each shot which prematurely resets the NV^{-} spin state and can excite other unpaired electrons in the region of interest or photo-excite a silicon substrate.

To remedy this, the Isomet RF driver was replaced by a home-built RF driver with 50 dB contrast between the fully on and off states. The home-built driver Figure 3.7 was based around a fast, high-exclusion RF switch. An additional benefit was provision of fast remote power control was in the form of a variable voltage attenuator (VVA). To access the full range of diffraction efficiency of the AOM the RF signal was amplified to up to 32 dB with a cheap, generic very high frequency (30 MHz to 300 MHz) (VHF) amplifierboard. The RF output was compared to that of the Isomet driver on a fast oscilloscope.

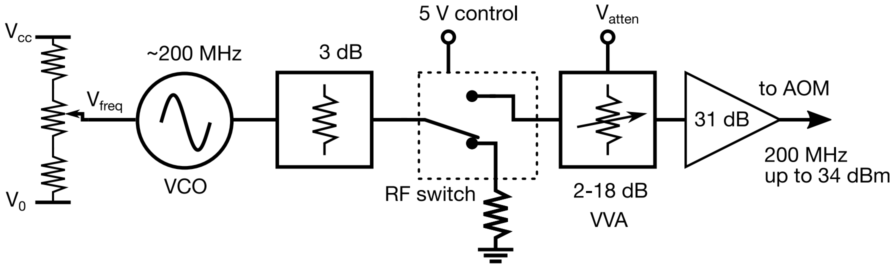

Figure 3.7: Diagram of the home-built AOM driver. This prototype was subsequently copied for all of the pulsed ODMR systems in our lab enabling long duration pulsed ODMR measurements and fast saturation measurements.

The VVA on the home-built AOM driver Figure 3.7 added the capability to control the laser power delivered into the objective immediately with a voltage and without the control oscillation and instability inherent in fine control of the laser diode current. This system was used on both the low-temperature and room-temperature microscopes for power control Figure 3.8.

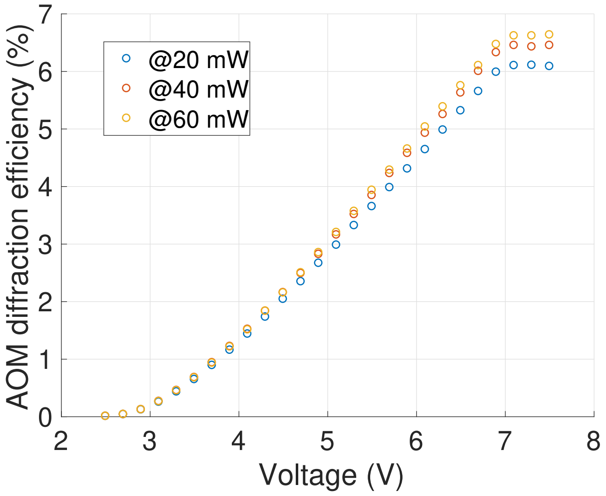

Figure 3.8: Diffraction efficiency of the AOM when moved to the room-temperature system. Efficiency was measured as the ratio of green excitation optical power into the microscope objective to the set point of the Laser Quantum GEM532 laser source. Optical power was measured with a Thorlabs PM100 power meter. By varying the control voltage, diffraction efficiency can be varied. Other losses in the optical path are included in this overall measure - in particular the losses at the pinhole used to "clean up" the beam profile after distortion by the AOM. This end-to-end calibration allowed calibrated set points to be used selected, speeding up saturation measurements from twenty minutes to seconds.

This prototype AOM driver and associated software were used very effectively in the work on laser-written single NV$^-$ to extend pODMR measurement times from less than 100 µs to milliseconds - also providing instantaneous power control and optical saturation measurements. Several replicas have been made for use on all of the pODMR experiments in our lab.

3.5 Software control

3.5.1 Requirements, planning and approach

Effective experiment control, coordination and data acquisition systems are essential in this set of experiments. Suitable candidate nanodiamonds are located by controlling position in three dimensions and measuring the rate of single photon counter pulses at each position, sampling for some milliseconds at tens of thousands of positions. In a similar way, fluoresence is measured with varying microwave frequency to find resonances and with different orientations of magnetic field to find the alignment of the NV^- axis of symmetry. Nanoscale single photon emitters must be tracked to compensate for focal drift whilst microsecond long pulsed ODMR experiments are performed millions of times. Laser, microwave and RF pulses need to be controllable on sub-microsecond timescales. Photon arrival times must be measured with nanosecond precision from two detectors and accumulated for HBT experiments and pODMR. None of these experiments can be conducted by hand and they are all essential to successfully make measurements which push the limits of cryogenic sensing with nanodiamonds.

Some aspects of all of these experiments occur over shorter time scales than can be controlled by a scheduled general purpose computer and so require dedicated embedded systems - either proprietory hardware or bespoke microcontroller based systems. Some of these sub-systems must be set programmatically to vary parameters over short time scales or to expect particular signals. In some cases coordination between sub-systems is best achieved using synchronising trigger pulses. For others, no real-time coordination is required and it is sufficient to record how a parameter is varied synchronously for post-processing. In either case, thousands to millions of data points may be generated and a user interface is required to orchestrate the experiment and to collate, record and display the results to the experimenter.

This is not a treatise on software engineering however as over 2 years of effort and tens of thousands of lines of software were committed to this end together with Anton Tcholakov, Jake Lishman and Dr Ben Green it is worth some discussion of what the considerations were behind this work, to give some review of what was achieved and to reflect briefly with hindsight on problems that were encountered.

With a multitude of approaches to this part of setting up the experiment, several salient points were considered: multiple emerging experiments in the lab had overlapping requirements for control systems; no existing software provided what was required; the closest known implementation of a more limited system elsewhere was fragile, inextensible and unmaintainable; effective handling of concurrent control and data acquisition would be essential; a few members of the group had past software engineering experience, but time was limited; complexity of software projects grows rapidly with concurrent, real-time systems; most bespoke lab experimental control software cannot be maintained after personel leave; investing time in the foundation and framework should pay off through curtailing the growth of complexity; a more loosely-coupled system would be more flexible for responding to inevitable experimental changes; some existing hardware and possibly future proprietory hardware provided only Microsoft Windows drivers.

Complexity is the major difficulty encountered in building larger software systems. Systems small enough to be well understood in isolation are often relatively straightforward to design and implement Figure 3.9. As systems grow in complexity, if changing a part causes a cascade of changes in connected parts then at some point it becomes too expensive to refactor to

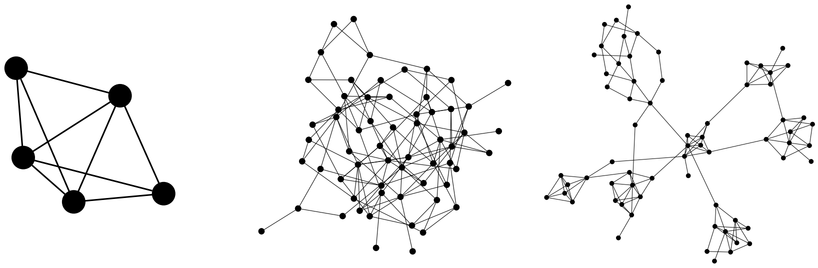

Figure 3.9: Abstract illustrations presenting the case for investing time in software architecture. A small, manageable system (left) is straightforward. When a simple system grows into a complex, monolithic, deeply interconnected system (centre) it becomes difficult to change, extend and maintain. By developing loosely coupled components within a suitable interlinking context (right), the growing interconnections can be managed so that parts remain small and can be changed when necessary with less cascading impact.

remove discovered structural problems and they start to compound leading to brittleness, unintended consequences and difficulty in fixing problems.

Ideally, subsystems should be small enough to be manageable with internal state that is entirely opaque to other components the system. If changes in the state of a part can affect other subsystems or other subsystems reach in to access internal state the parts are no longer independent and need to be maintained as a more unwieldy whole. They cannot be tested independently and the assumptions about the impact of refactoring as problems are uncovered cannot be made. Keeping components simple enough that programmers are not overloaded by their interactions is necessary to be able to work efficiently, even if some extra pieces of work are needed to link parts together. A loosely coupled network of simple systems is easier to reason about than one big system. The more difficult question is how to adequately achieve this, particularly using unfamiliar tools.

De-coupling parts of a concurrent system adds significant additional complexity. Data flow may be driven by real-time pushing of data from external hardware with rapidly filling buffers. Commands may need to be sent concurrently to several instruments and correlated with incoming streams of data. Many experiments are long running and it is not possible to wait until all work has finished to retrieve acquired data. Sequencing of commands, acknowledgements and error handling between different external systems needs to be adequately robust - losing the results of an overnight scan as helium boils off should be avoided.

To protect against regressive faults, change control was considered essential. LabView was largely discounted despite license availability due to the lack of change control, difficulty of writing large scale, maintainable, reusable software and the risk of "vendor lock in" to expensive proprietory National Instruments hardware. A high-level compiled language with strong types would guard against many of the most common faults that emerge in Python systems (such as subtle implicit conversion of data types which is only discovered at run-time). By separating the system into separately version controlled modules with common type definitions components such as drivers for instruments could be tested independently. Trouble-free concurrent operation was also essential, if only to retain a responsive user interface, so Python was set aside due to problems with the coarse global interpretter lock preventing effective multi-threading. For larger applications, Python also introduces some manageable difficulties keeping track of third party library changes and more problematically the lack of compile-time checking or strong typing defers discovery of errors until runtime. As many experiments would use combinations of the same laboratory equipment and tasks the time spent developing and maintaining the common underlying platform could be spread over multiple projects.

Concerns over the availability of cross-platform proprietory drivers for lab equipment and ongoing operating system support internally led us to base the common platform on the Microsoft Windows .NET Common Language Runtime (CLR) [166] - a virtual machine based framework for general development - despite unfamiliarity with programming in a Windows environment. In particular, the relatively new functional language F$^\sharp$ [167] - based on the venerable language ML - provided many inbuilt features for writing type checked, concurrent software without explicit, low-level concurrent threaded code. As concurrent software is typically a minefield of subtle problems, this seemed promising. The sequential steps of experiments could be declared at a high level with all the interdependencies described so that the compiler could translate that into work to be completed concurrently on a pool of threads. However, not only did this require learning new languages (F$^\sharp$ and C$^\sharp$) but also the Windows development toolchain including the Visual Studio integrated development environment (IDE)[168], the Windows Presentation Foundation (WPF)[169] GUI framework, legacy GUI frameworks, two package management systems, two build systems, socket libraries, Reactive programming techniques with Rx.NET[170] and many frequently updated third party libraries. It is difficult to make the best informed structural choices for a medium sized, flexible software system that lead to simple enough solutions whilst the whole platform is still unfamiliar. These difficulties were exacerbated by problems with incompatible, frequently changing and deprecated third party and core framework libraries and a general immaturity of the underlying platforms and documentation. These problems slowed development to a near standstill over time, negating the benefits we had sought. Despite achieving some of the original goals, later than planned, fixing the remaining problems was increasingly difficult and so when the largely complete Qudi system was released by University of Ulm serious consideration was given to switching to and adding to their software base.

3.5.2 The F$^\sharp$ /.NET implementation

A strongly typed, functional language was chosen for the benefits of providing strongly checked interfaces between parts of the implementation. Limiting the stateful parts of the implementation is particularly significant for concurrent systems. Rather than relying on locking access to a skeleton of data structures and shared resources the access, which is a frequency bottleneck or even a reason for hard to debug deadlock conditions and race conditions, the different semantics of functional programming keep the operating state of the system in the within the tree of functional calls.

Features of the F$^\sharp$ type system

Passing and returning strongly typed parameters is central to how this is implemented and even functions are typed entities which can be passed as parameters or composed through currying or operators which allow higher order functions to be composed abstractly. Whilst the language is strongly typed, functions do not necessarily need to specific types fully as inputs. As long as the type can be inferred during compilation, functions can be written to act generically on placeholder types (written in the form `a'`). This allows operations to be abstracted from the specific data they act upon. This insulates related functions which do not rely on the specific type being changed from needing to be manually updated - an error prone process - when parts are inevitably refactored. In weakly typed languages such as Python, there is no immediate development overhead for making such changes as there are no such checks or automatic run time type conversion hides problems. Errors made in such changes are only found at run time or when a particular use case is

```
type Frequency = decimal<Hz>
type ScanParameters = {
    StartFrequency  : Frequency
    EndFrequency    : Frequency
    Power           : decimal<dBm>
    Points          : int
    IntegrationTime : int<ms> }
```

Listing 1: F♯ provides strong types, including qualifiers for units of measurement, including SI units, which can help ensure parameters and data are handled correctly dimensionally. Record types can be serialised and deserialised to save complete experiment session parameters alongside the data.

encountered. With a strongly typed language with type inference, the compiler can check for nonsensical statements as the software is written. With the support of a language-aware IDE and type inference the prohibitive "book-keeping" overhead which enables basic types checks before the software is used can be productively directed to provide beneficial suggestions and refactoring assistance. The Python interpreter will allow any entry to be added to associative arrays but cannot determine if a mis-spelled entry, omitted parameter or ill-considered change is a problem until it is encountered at runtime. An F♯ record type Listing 1 or unit of measure can follow through the usage whilst the code is being written, saving time consuming and omission prone manual inspection. Invalid or incomplete statements are not permitted, which transfers development effort from patching up errant behaviour in an imperfect live system to the constraints of working within more rigid constraints whilst the code is being written.

Two other unusual features of the type system in F♯ are worth mentioning. The option type can be `None` or `Some x`, making unset parameters explicit rather than introducing null pointers, undefined values and such which eliminates a common source of errors by keeping such states within the definition of the system. The option type is an example of the more general discriminated

```
type PositionerState =
| Off
| Parked
| Floating of offset : float<V>
```

Listing 2: F$^\sharp$ discriminated union types have many uses however they are ideal for representing the state of a state machine or an experimental parameter in one entity (as opposed to a split over a flag variable and unconnected parameter fields)

union (DU) type. A DU Listing 2 is somewhat analogous to union time in C. A DU can hold one of several enumerated values or states with associated parameters, which provides flexibility. They are ideal for implementing state machines using “mailbox processors” - which are the cogs, cams, in-trays and out-trays connecting the more rigidly coupled functional parts of the system together.

Asynchronous workflows

Functions in F$^\sharp$ are analogous to straightforward mathematical functions rather than list of instructions which “do” something in a procedural language. When called with some parameters they evaluate and return a result at that point. The semantic difference is subtle but significant. Semantically a mathematical function does not “run” concurrently. It evaluates unambigiously regardless of the order of evaluation of parameters and is replaced by the value returned.

Nevertheless, particularly when waiting for the stages of an experiment, concurrency and deferred evaluation are necessary - if only to be able to monitor and stop the experiment. For a common example, consider a triggered sweep of a microwave source and detector. Once set, the system communicates with the source and triggers a sweep. At its simplest, it should then wait until that scan is complete before triggering the next. However,

```
  // Starts step operation then waits until it completes
member x.StepAndWait direction count = async {
    do! x.Step direction count
    do! x.Wait() }
```

Listing 3: This F♯ member function generates an asynchronous computation parameterised by direction (a DU) and count (a number). Although the types are not explicitly specified here, they are inferred and checked at compile time. An asynchronous workflow is chain of instructions which can be explicitly run on the current thread or on a background thread. The type of `StepAndWait` is `Async<float<V>>` as no value is returned. Both `Step` and `Wait` are themselves more complex computations of type `Async<float<V>>` which communicate with the positioner controller module and wait for a physical movement to complete. Although they do not return a value the system will wait for each to complete. If a return value was expected, this could be bound to using the `let!` keyword.

we also need to display the data as it is produced and allow the user to stop the scan. The simplest way to keep the experiment responsive is to handle these tasks concurrently - at least logically and where necessary. F♯ describes a computational process which will, at some deferred point, evaluate to give a value by an *asynchronous computation* Listing 3. These have types of the form `Async<float<V>>` which describes a "promise" to return a voltage float value "sometime" i.e. when the computation is run. These computational expressions can be assembled into more complex asynchronous workflows with asynchronous computations waiting for other asynchronous computations to complete and perhaps yield a value that they require with the `let!` keyword. This captures the dependencies between deferred and concurrent processes allowing the compiler to mechanically handle error-prone concurrency efficiently. Computational expressions can be passed as data and run on the current thread or in a background thread, optionally with continuation response for the cases where the expression completes successfully, fails or is cancelled (cleanly) using a cancellation token produced when the work was started.

Mailbox processors

Whilst functions and asynchronous workflows can be used alone, waiting until the work is finished, another element simplifies interaction of components and communication with the user through a user interface. The mailbox processor acts something like a postroom between subsystems. Messages can be fed in to a queue and a state machine is implemented to execute actions in response to the messages. Such forms of message based communication are ideal for decoupling components of a concurrent system with explicit, asynchronous communication which, hopefully, allows the concurrent and sequential subsystems smaller and simpler. They also provide an effective buffer of flexibility between whichever event model the user interface uses - which can generate requests at any time - and on-going control of a free-running experiment driven by independent hardware.

Graphical user interface (GUI)

The currently recommended user interface toolkit for new Windows applications is the WPF toolkit. User interface components can either be created by explicit function calls or, preferrably, by description in a separate, declarative, layout document in the Extensible Markup Language (XML) based Extensible Application Markup Language (XAML). Interactive operation of the experiments with display of scan results and imaging in real time is essential to locate and study sites of interest. To display imaging and of magnetic resonance charts, a tool kit which supports heat maps and charts is essential. Ideally it should also support mouse interaction to identify points of interest and generation of images - as a convenience for recording. Of the surprisingly few available charting packages, OxyPlot was chosen despite some sparsity in documentation. A particular difficulty was found in the need to use a mix of XAML driven descriptive user interfaces and creation of entities through the OxyPlot API. In addition to the choices of GUI framework, several mechanisms were available to respond to events initiated by the experimenter and to data arriving from instruments. Particularly in combination with F♯ rather than the more mature C♯ the lack of a single, reliable, well documented way to bind these elements together caused many problems.

Reactive programming elements

In addition to the asynchronous programming elements introduced in F♯ , reactive programming in the form of Rx.NET was also used to invert the handling of flows of data from instruments - allowing definition of what to do with the data to be separated from how the data is generated Listing 4. Reactive programming allows actions to be performed as sections of the data are emitted so in a sense it acts analogously to wires in a LabView implementation but with a rich, standardised set of high level operations to control the flow of data. Reactive programming can be thought of as a response to the chains of callback functions passed to be run when new data is ready.

Consumers of the data can subscribe to an “observable” stream and react as it comes in. Observables can be composed and mapped to produce new observables: integrated; aggregated; sampled and paired with the experimental parameter which are being varied. Derived observables can be as high level as a stream of the latest confocal image paired with parameters or a notification that the experiment has finished. The underlying call backs will only be invoked if the observable has subscriptions and multiple observables can be subscribed to. This provides a degree of abstraction over waiting for events

```
try
    anc300.Connect()
    photonCounter.Connect()
    timedPhotonCounts
    |> Observable.windowTimeCount (TimeSpan.FromMinutes 1.0) 1000
    |> Observable.sample (TimeSpan.FromMilliseconds 500.0)
    |> Observable.map (Observable.toEnumerable >> Seq.toArray)
    |> Observable.add updateTimeChart
with
| exn ->
    MessageBox.Show <| sprintf "Failed to connect: %A" exn |> ignore
```

Listing 4: A simple example of reactive programming with Rx.NET and F♯. After obtaining connections to the instruments, projects the count rates emitted by a Warwick built photon counter to scrolling array of the last minute's samples updated every half a second. The handler *updateTimeChart* is subscribed to this data stream. If an exception is thrown a dialogue box is shown.

and it allows the experiment and components of the experiment to emit data concurrently without foreknowledge of how that data is to be used. Implementations typically can typically handle high rates of data. However, effective use of reactive programming has numerous subtle pitfalls and it is vulnerable to problems with implementations - especially in subscribing to new streams of data starting at run-time (such as experiments), interaction with thread concurrency and the difficulty of debugging race conditions and dead-locked "logjams" at run-time.

Evaluation

Whilst learning how to use these features took more time than expected, it was felt that the benefits of enabling good engineering practices would repay the investment of time. However, tackling the learning curves of so many tools at once without an established code basse or local expertise was more risky than anticipated - particularly as several were less mature than anticipated.

The home-built F♯/.NET implementation took longer than expected however it did achieve some success, short of full experimental operation. Support was written for a number of instruments including: Keysight N5172B microwave sources [171]; PicoScope 3000 & 5000 series oscilloscopes [172]; Attocube ANC300 positioner controllers[173]; Rohde & Schwarz HMC8043 programmable power supplies. A serial and TCP/IP control abstraction for Virtual Instrument Software Architecture (VISA), Standard Commands for Programmable Instruments (SCPI) and similar line-mode instruments was written [174] which was specialised to support both the standard control port and programmable Lua[175] control port of the Attocube open-loop positioners [173] along with several other VISA and SCPI controlled instruments including the locally built PIC microcontroller family (PIC) based photon count integrators [176].

Remote control of the ANC300 console required the use of TCP/IP connections to two control ports. The standard control port provides the base functionality and is well documented. Some functions are only available on the programmable Lua console which connect to an embedded interpretter for the simple Lua[175] language. The Lua control port can be used to change mode to "voltage offset" or can be used to run simple programmes. Using these control tick-slip piezo positioning control with single steps and a range of speeds of continuous movement was implemented with a GUI to control the position. Using a method described in more detail in Section 3.5.3 the z-positioner was coopted into use as a short travel vertical scanner for focusing and a continuous oscillation mode added to aid with refining the optical alignment.

Connection status and "leases' of instruments to share their use between active experiments was implemented along with an launch menu for difference subsystems. A scrolling live count rate chart was written. Integrating continuous wave ODMR scanning was added using the locally built

PIC photon count integrator was operating with live updates and saving of data - after delays due to misattribution of an optical instability caused by back-reflection into the laser source from the FC/PC single mode optical fibre front facet. An asynchronous workflow builder for managing generic scan based experiments was developed. Two-dimensional confocal scanning was implemented and running Figure 3.10. Whilst this system could produce some data, a great deal of integration work was still needed to build a stable, trustworthy platform. Frequent, near-intractable bugs were continuing to sap time. The system was still progressing and may have been completed, however during this slow, troubled progress a larger lab released the software they had developed[165].

3.5.3 Transition to Qudi

Whilst a significant amount of time and effort had been invested in developing the layers of the F$^\sharp$ code base to be used experimentally, too much work was still required with the resources available. Ongoing changes to the many dependencies on third party libraries took time to debug and integrate. Debugging of deadlocked interactions between the concurrency handling abstractions of the Reactive programming and the asynchronous monads in F$^\sharp$ had unresolved difficulties, making concurrency as fraught with problems as hand written thread management. Problems in different subsystems where insufficiently isolated from each other - using a common thread pool in a single process to share access to the hardware in parallel. Imaging Figure 3.11 and ODMR were achieved, but with the availablity of the more complete Qudi[165] software system developed at University of Ulm, the difficult decision was made to add to Qudi instead of maintaining out own system.

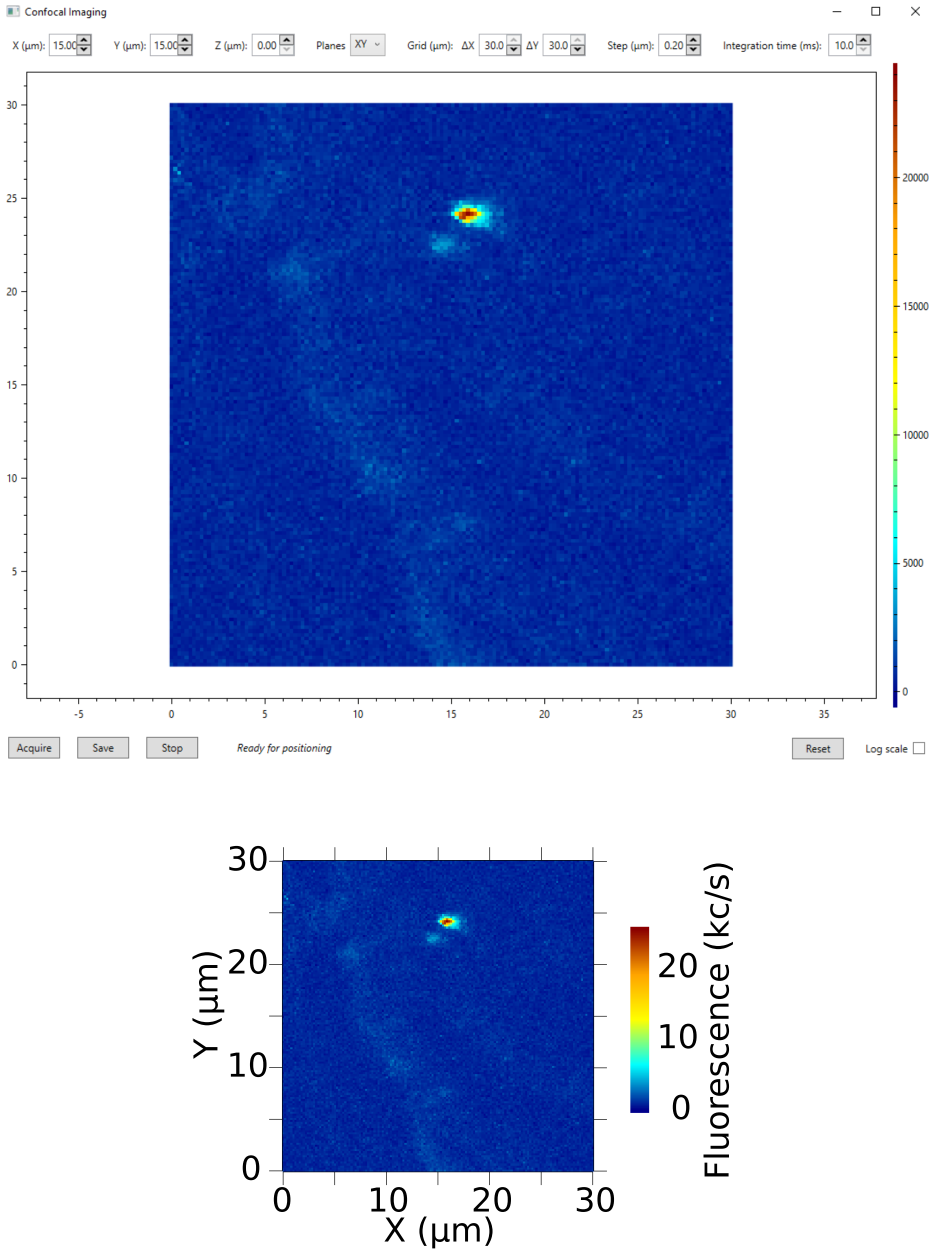

Confocal Imaging

X (µm): 15.00 Y (µm): 15.00 Z (µm): 0.00 Planes XY Grid (µm): ΔX 30.0 ΔY 30.0 Step (µm): 0.20 Integration time (ms): 10.0

Ready for positioning

Log scale ☐

Figure 3.10: (*top panel*) Screenshot demonstrating the confocal imaging capability of the home-built F$^\sharp$ code base at room temperature. The top bar provides controls to select the region to be scanned, the scan resolution and the sampling time per point. Status messages and the buttons to start, stop and save are at the bottom of the screen. The count rate per-point can be toggled between a linear and a logarithmic scale. The maximum scan region, shown in this example, is 30 µm × 30 µm. The sample in this case is nanodiamonds deposited on a silicon substrate in a mist of methanol. (*bottom panel*) The same image replotted with a legible scale.

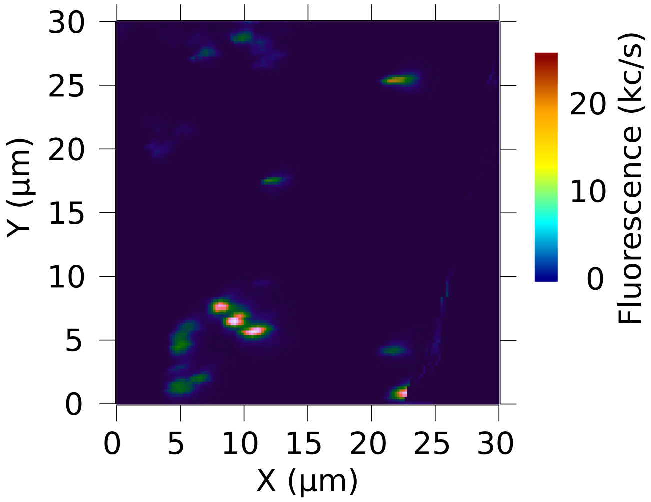

Figure 3.11: Image taken with the local F♯ code base at room temperature. The sample is nanodiamonds deposited on an unpatterned silicon substrate.

3.5.4 Additions to Qudi

Attocube positioner control

The two control channels for the Attocube ANC300 open loop stick-slip positioning controller were re-implemented as a Qudi instrument. In addition to adding low-level positioning commands for single step and continuous movement at different speeds, a GUI for manual piezo-positioning three axes was added (using the Qt toolkit and PyQT). The embedded Lua[175] control port of the Attocube ANC300 provides access to additional functions and limited programmability. Using this functionality the offset voltage mode could be accessed to implement a form of fine positioning and to allow a degree of continuous manual fine control of vertical position by using the Z-axis positioner as a short travel (<1 µm) piezo-electric scanner.

Attocube short vertical scans and focus tracking

In the absence of a vertical piezo scanning stage, the vertical stick-slip positioner was used as a make-shift, short travel piezo-electric scanner stage.

By using the Lua control port manually to run commands on controller, the rear serial port was repurposed as an improvised trigger to signal changes in position by asserting the Data Terminal Ready (DTR) pin of the unused port. With the addition of some electronics using a quad operational amplifier as a Schmitt trigger and amplifier, this made a channel for a Lua function to electrically emit a point trigger pulse. A small loop could then be defined in Lua to run a confocal scan of the vertical position with a single command in less than a second Figure 3.12. The pulses from the serial port allow for synchronised acquisition using the Warwick pulse counter, the Swabian TimeTagger or the National Instruments X-series hardware.

This was an essential development for effective focusing as a control loop driven from the host computer would cover the same range in tens of seconds. Given the short travel and expected rate of drift a slow scan rate would be likely to lose focus lock quickly - the travel available is similar to the full width half maximum (FWHM) of the vertical PSF. Fitting the scan results gives four options: the focus lies in the scanned range where it can be tracked by setting the voltage; the focus is higher or lower, so attempt to move in the appropriate direction by ~300 nm and try again; the focus is lost. If the focus is lost due to lateral drift (potentially resulting in a double crest) focus might be regained with optimisation in the X-Y plane using the main piezo-scanning stage.

It is essential that the focus optimisation is fast enough to maintain tracking in despite drift, particularly due to expansion from changes in the magnet currents. After magnetic field changes, measurements can be deferred

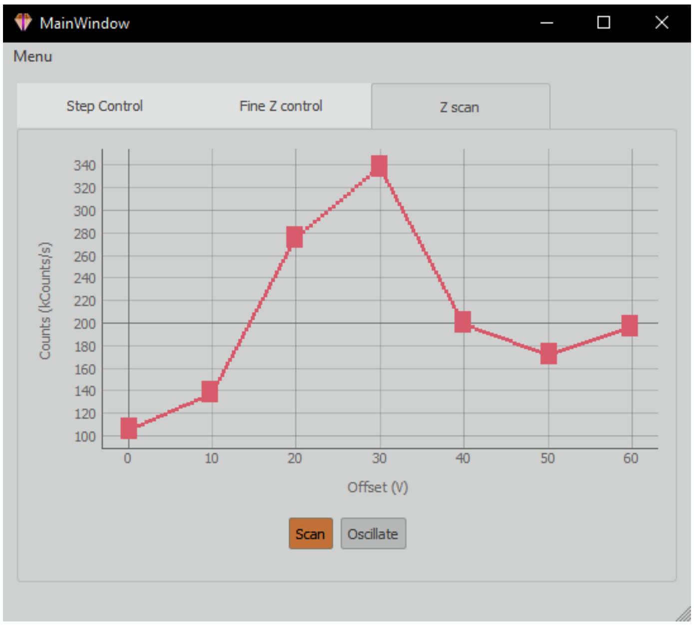

Figure 3.12: The Qudi version of the Attocube positioner control GUI. Scanning through a surface or a fluorescing point source such as a nanodiamond gives a peak which can be fitted. Given the limited scan range, fitting can be ambiguous so the focus needs to be updated frequently enough to track the focus until any movement slows after changes.

until the rate of drift has slowed.

Hanbury-Brown Twiss measurements

An HBT measurement logic module was added, using the Swabian Instruments TimeTagger for accumulation. A GUI module was also added, displaying the data as it was collected. Operations were included to start, stop and record the data controlled manually or by automation. The time period recorded should be ample as the normalisation to the uncorrelated "background" is critical to the determination of the fluorescence lifetimes, fitted to a decaying exponential, or to the fitted value of $g^{(2)}(0)$.

Calibrated AOM power control

The hardware and software of the improved AOM RF module were built for both the low-temperature and room-temperature systems, improving to the capability to measure long coherence times without leakage with or without the double-pass optical switch from ~50 µs to 2 ms. The VVA allowed instant control of the RF power applied to the AOM which could be controlled manually or via the fourth NI X-Series voltage output. The RF power controls the AOM efficiency and this was calibrated at different current-controlled laser powers. The added modules allowed the delivered power to be set based on the current laser output, as detected from the laser diode's photodetector and the AOM diffraction efficiency. No laser amplitude noise cancellation was implemented, although the possibility is there for future feedback control if required.

Saturation power measurements

An essential practical diagnostic measurement for single NV^- is the power required to saturate the colour centre P_{sat} and the maximum intensity emitted I_∞ as described in Section 4.3.2. Using the AOM power control and calibration, P_{sat} measurement times were reduced from around 30 minutes to around 1 s. This allowed rapid differentiation of single NV^- colour centres in the currently optimised orientation and to notice any degradation in the performance of the optical system.

This automation and speed of acquisition allowed P_{sat} data to be gathered and recorded as part of automated characterisation. Automated fitting of P_{sat} also allowed optimal power to be applied relative to the current P_{sat} for subsequent automated measurements.

Improvements to T_2 experiment efficiency

A significant data collection efficiency improvement on long pODMR measurements such as spin-echo decay T_2 measurements was enabled by adding the capability to change the laser power automatically during focus optimisation. The focus optimisation routine needs to run periodically frequently enough to maintain focus over hours (every few minutes is generally sufficient). The focus optimisation requires enough light for imaging collection and so the mean optical power needs to be high enough for the maximum to have sufficient visibility above the background noise. In pulsed ODMR experiments this required a long (~15 µs) initialisation pulse just to support focus optimisation, limiting the shot repetition rate. A T_2 measurement would take around 20 h, with no guarantee the site being studied would give a result.

With signal controlled power level, the focus optimisation process could pause the pulsed ODMR measurement, turn the laser on continuously, change the laser power, optimise focus faster and recommence the pulsed ODMR measurement with an initialisation pulse length of 3 µs. This allowed collection of T_2 data on many sites with long coherence times with reduced uncertainty in a fraction of the time (2 h to 4 h). This improvement also allowed longer 12 h to 24 h T_1 and dynamic decoupling experiments such as XY8-4 and XY8-8 - as described in Section 2.3 - to be run effectively.

Responsive automated, long running experiments on multiple targets

Crucial to data collection on a large number of laser-written sites with the room-temperature confocal microscope and to optimise and find good nanodiamond candidates on the low-temperature confocal microscope is the capability to automate initial evaluation of sites. This frees the, error-prone, experimentalist from labourious work but also ensures that consistent measurement conditions and recording can be applied to each site. It also enables the experiment to continue 24 hours a day making full use of contended instruments with remote monitoring.

An automation system was added to Qudi and used in the characterisation of the laser written three-dimensional arrays. A few hundred sites within manual stage range were identified and each was visited for position measurement (by focus optimisation) Section 4.4.5, P_{sat} Section 4.3.2, HBT Section 4.3.3, cwODMR with fitting to discover a suitable resonance at near to the expected microwave frequency, pulsed ODMR Rabi period measurement, Ramsay pulsed ODMR and T_2 measurements could proceed automatically for over two days. The scripting system monitored the progress of each measurement, waited for each to complete, optimised focus as required, and used parameters from each stage to configure the next experiment - only continuing if the site was suitable for the subsequent step.

Another example operation was to image the full confocal volume of arrays, referencing each slice to a single isolated site to account for small stage drifts. This allowed visualisation and assessment of full laser written NV^- stacks in three dimensions.

Whilst the low-temperature system has not yet reached the stability to automate, the room-temperature system was used extensively to consistently collect a statistically large amount of data on the laser written NV^- sites, including tens of T_2 measurements on laser written NV^- where few isolated measurements had been possible in previous work.

3.6 Imaging and alignment

A common indicator of an alignment problem can be seen in images containing point light sources. Where either the excitation arm, the detection arm or both are misaligned, the point light sources will be extended as convolutions of the point spread functions of the two focii as in Figure 3.13. Each site appears as a repeated, crescent motif formed from the overlap of the point spread functions of excitation and detection.

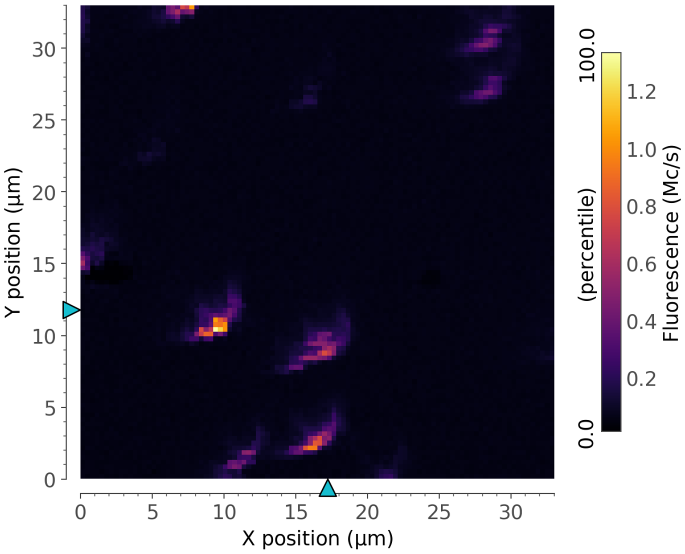

Figure 3.13: Confocal image of nanodiamonds on a silicon substrate, taken using Qudi, showing an effect of misalignment.

Once aligned, sufficiently high resolution imaging of nanodiamonds on silicon was achieved Figure 3.14, although single-emitter detection has not yet been confirmed.

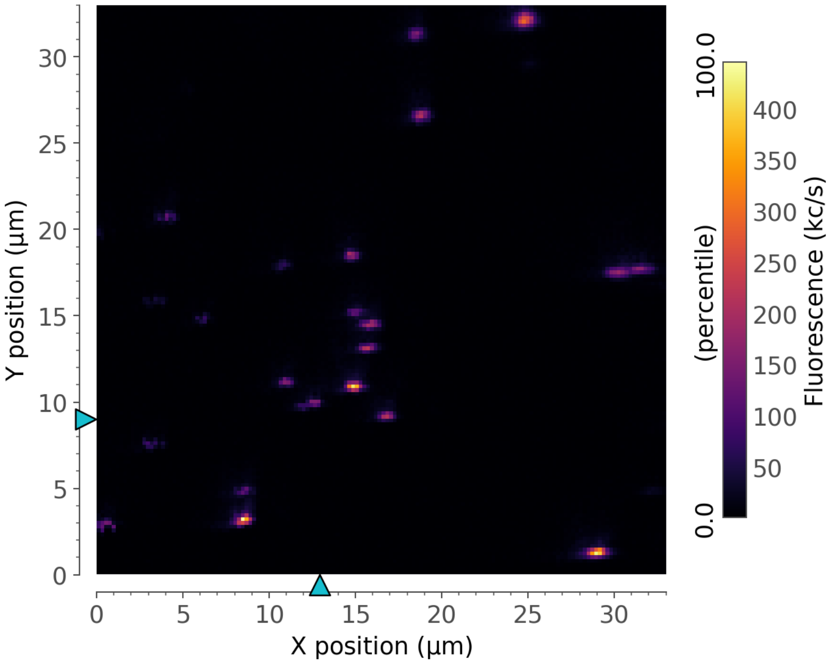

Figure 3.14: Confocal image of nanodiamonds on a silicon substrate, demonstrating the room-temperature imaging using the fibre confocal microscope with at least 1 µm resolution.

3.7 Magnet

3.7.1 Requirements

Sustaining the quantum state of the NV^- system for long durations is essential for either nanoscale sensing or quantum information processing. Sensing requires the minimisation of decoherence processes to allow enough time to accumulate phase from exposure to weak interactions. Quantum information processing requires time to complete operations. One cause of decoherence is state mixing and this can be minimised by applying a magnetic field along the C_{3v} axis of symmetry to separate the ground states of the NV^- system sufficiently that the states of the two level system being driven can be treated as good quantum numbers. If the field is misaligned with the NV^- axis of symmetry or is too weak, long quantum coherence times (T_2) cannot be achieved. To be effective the magnetic field orientation needs to be within a few degrees of the C_{3v} axis of symmetry and the field strength needs to be greater than 3 mT. Fields more than 10 mT would be preferrable[67]. A field strength of 20 mT to 30 mT would suppress revivals resulting from the ^{13}C nuclear spin bath in natural isotopic abundance diamond. As a stretching goal, a field strength of greater than 100 mT at low temperatures would have applications in quantum computing for optical readout of dopant spins in silicon (e.g. Si:P and Si:Bi) via NV^-. Whilst not essential in diamond, these higher field strengths would make accessible additional zero-crossing points with low magnetic field noise sensitivity.

With C_{3v} symmetry, this is relatively straightforward for bulk material. The crystallographic orientation of standard plates is normally [100] or [110] so that NV^- have one of four possible orientations. Once the orientation is established a permanent magnet with a solid mounting can be fixed in any of the four orientations to apply an appropriate magnetic field to the NV^- in that orientation with precision across the whole plate. All NV^- will be in one of those orientations. One major complication with scattered nanodiamonds is that the symmetry axis can be in any orientation! What is more, finding a nanodiamond with all the required properties will require study of hundreds of defects in different orientation, so the procedure for alignment has to be both relatively quick and automatable.

The necessity of determining the orientation of nanocrystals and applying a sufficient magnetic field at the tip of the cryostat probe adds additional physical, electrical and thermal constraints. Space is very limited by the 50 mm bore of the canister. Too small for a mechanical system capable of rotating arbitrarily around the sample, even if suitable cryogenic nanopositioners could be found. The presence of the microscope objective less than 0.5 mm above the sample and a nanopositioning stack beneath severely constrains the use of a conventional system of electromagnetic coils in a Helmholtz geometry. There is insufficient room for even the cylindrical saddle coils commonly used in NMR - saddle coils in the available space away from the nanopositioning stack would only be capable of applying around 1 mT. A large set of high power coils outside the canister in the cryostat would unfortunately be prohibitively expensive to retrofit.

This necessitated the design of a coil system which used space only underneath the sample, with a mass of no more 180 g but nevertheless was capable of

- Orientation of the magnetic field in any direction
- Field strengths of 3 mT to 30 mT
- Magnetic field noise that does not limit quantum coherence

- Manageable heat dissipation requirements
- Mechanical stability
- Room-temperature and cryogenic operation
- Operating at 4 K without heating the sample

The saving graces are that a) the magnetic field only needs to be homogeneous within the micron-scale confocal volume of the microscope and b) the NV^- can be used as its own vector magnetometer.

3.7.2 Design

A brass canister with thin walls for containing the coils Figure 3.15 designed to make full use of the space available was machined at University of Warwick. The canister contained the magnetic field coils and held the sample centred under the microscope objective along with the necessary microwave and RF control lines.

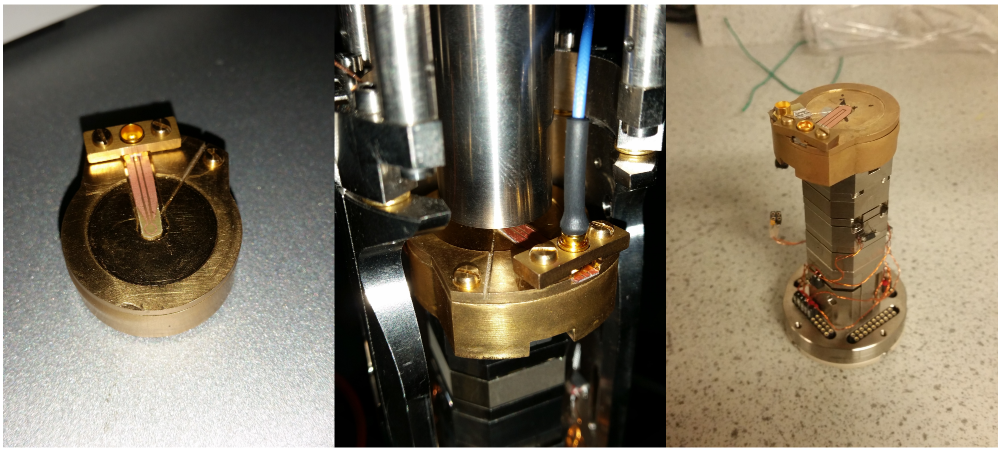

Figure 3.15: The magnet canister with a coplanar waveguide afixed, in place on the probe and mounted on the piezo-positioning stack respectively.

Inside the magnet canister, just under the sample and 0.5 mm of brass, lie four 0.5 mm thick copper coils in the shape of a four-leafed clover leafFigure 3.16. Combined with NV$^-$ magnetometry, the X-Y orientated magnetic field just over the surface of these sheets of 80 µm copper wire is sufficiently uniform to conduct experiments over the <1 mm typical working region, the tiny sub-micron optical confocal volume used in individual measurements, and the interaction range of the spins being probed. Underneath this novel magnet system, a straightforward solenoid supplies a vertical Z component of the magnetic field.

To access all quadrants, the current for each axis needs to be reversible. This is somewhat complicated as to minimise boil off only four of the wires fed through into the cryostat and down the probe are low resistance 200 µm copper (the rest are high resistance to reduce heat transport by electrons). The three circuits can share a common return path, however each channel in the HMC8043 constant current supply can only supply current in a forward direction. To reverse the current in any of the channels, the wires need to be swapped. This can be achieved with a set of double pole, double throw DPDT relays controlled by an Arduino Uno Figure 3.17. As the three channel supply cannot sink a reversed current the common wire is allowed to float and additional protection relays short circuit coils through a resistor as their polarity is switched.

By computer control of both the Arduino by commands over USB and the power supply over TCP/IP the full range of currents in both polarities can be reached on the three sets of coils. Where more rapid sequences of currents are required, the supply is programmable to allow synchronised ramps and pulsed duty cycles on the timescale of tens of ms to be set up remotely.

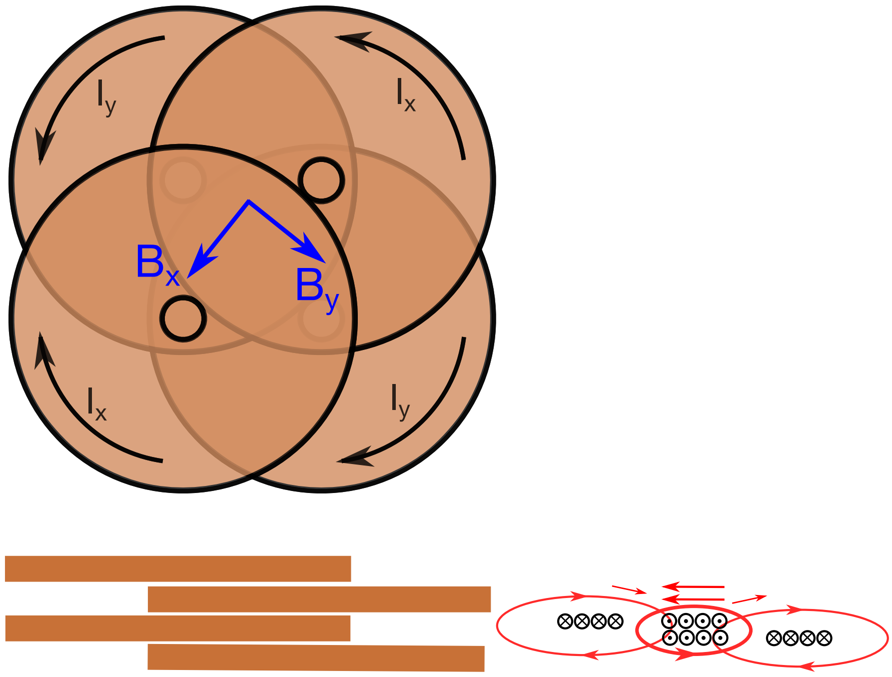

Figure 3.16: The x-y “cloverleaf” coil arrangement (*left*) uses the field just above the current running through the coils (*right*) where the sample is affixed. This would be ideal with a thin sheet of current extending to infinity however the full circuit must fit inside the canister. By pairing coils, the perpendicular component of the magnetic field from the outer part of the coil pair can be mostly cancelled out. The coils cannot go through each other (without complex interleaving) so asymmetry is introduced by the difference in height. This could be partly compensated for by adjusting the currents in the coils separately but only four reduced resistance pass through wires are available in the cryostat. Two pairs can be stacked to apply magnetic fields in any orientation in the X-Y plane.

3.7.3 Modelling

The magnetic field due to the five coils was modelled Figure 3.18 in Matlab using closed form expressions for the off-axis magnetic field of current loops[177]. Using the magnetic field of a coil single layer, the field of the assembled magnet could be simply summed as a linear combination of the field from each layer in the region of interest where the sample is placed.

As the brass canister, titanium piezo-positioning stack, diamond sam-

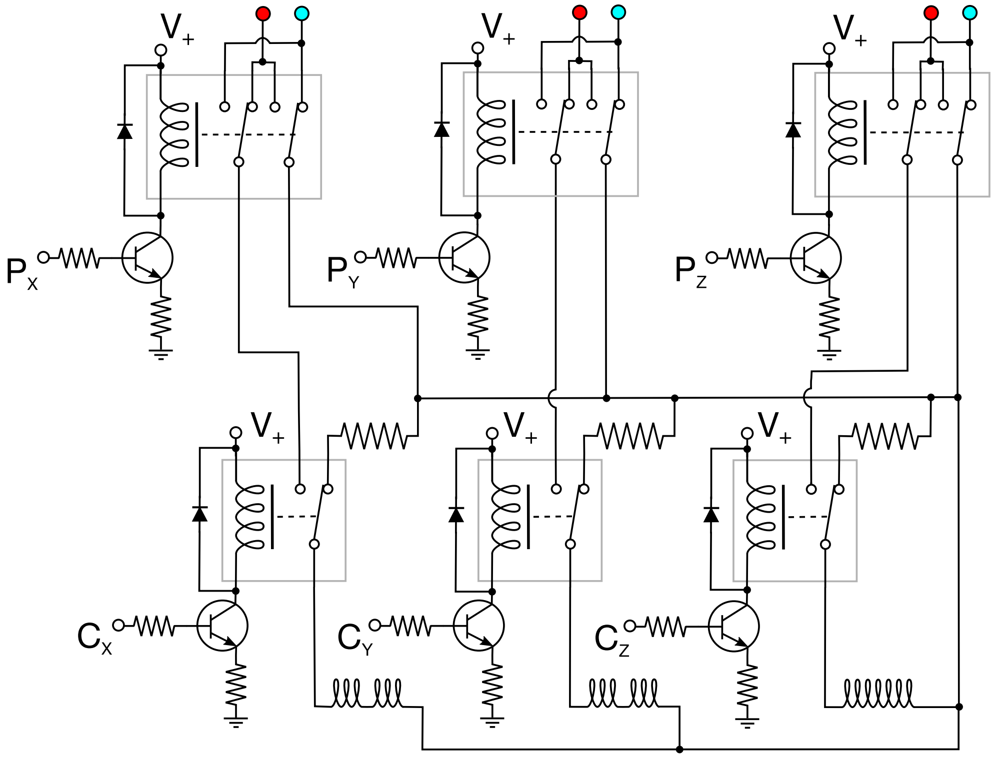

Figure 3.17: Circuit diagram for the magnet polarity switchbox. In order to access all orientations of magnetic field, double-pole double-throw relays are used to swap the polarity of current applied to each coil. The six inputs must share a common, floating voltage return path for current as only four low-resistance feed through wires into the cryostat are available to drive magnet coils.

ples, and copper have a low magnetic susceptibility magnetisation of the surrounding material is not considered here (although a ferrite flux concentrator could be added in principle).

The applied magnetic field need only be fully homogeneous within micrometre scale confocal volumes although it is convenient if the field is consistent in orientation and magnitude over imaging areas of 30 µm × 30 µm and positioning ranges of a few hundred micrometres.

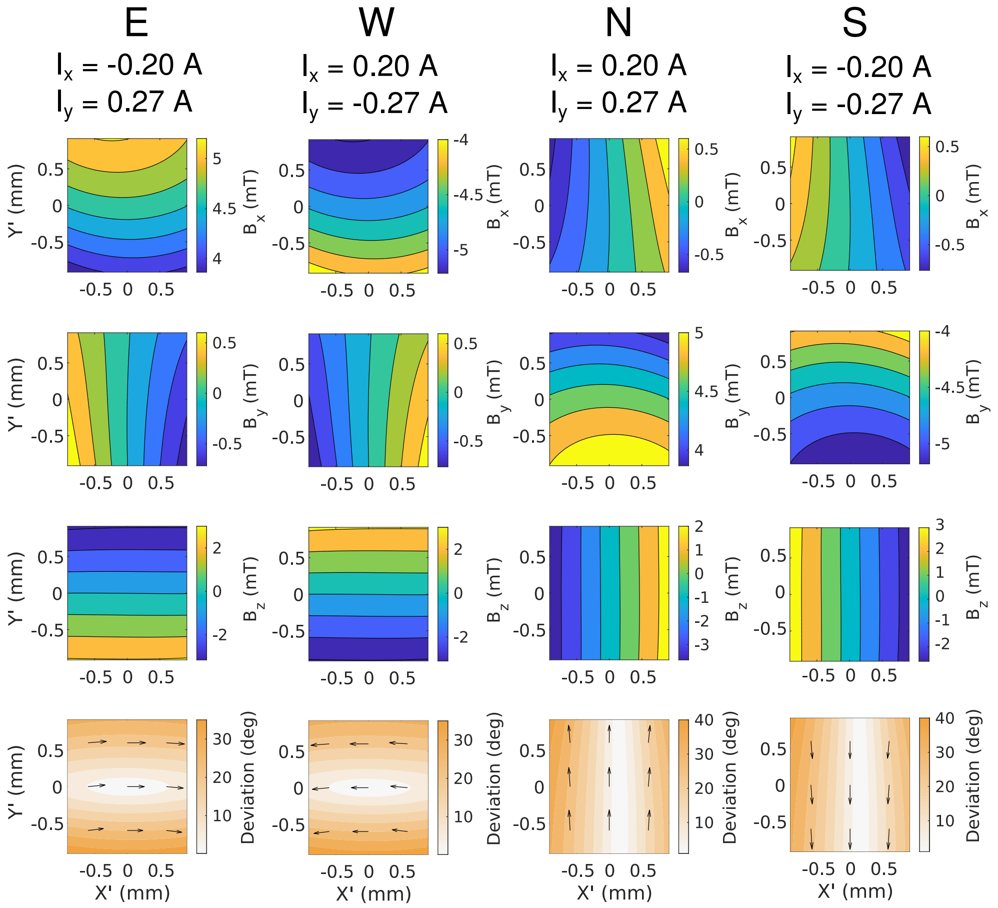

Figure 3.18: The components of magnetic field on the canister surface in the X', Y' basis at 45° to the coil orientations X, Y with equivalent currents applied to the two sets of coils, compensating for depth. The deviation of the field orientation from the planar directions (N,S,E,W) are shown in the final row. Much of the deviation is in the Z component which could either be compensated for programatically or minimised by further optimising the coil geometry.

3.7.4 Heat

Resistive heating is the limiting factor. Controlled via an ethernet interface, the current & voltage per channel can be monitored to infer the coil resistance and dissipated power and shut down if the resistance starts increasing too rapidly. Temperature changes can also be monitored by the Lakeshore temperature sensor and heating element immediately below the magnet canister. Accepting some heating, even at low temperatures where resistance is a fraction of that at room temperature, there is still the problem of thermal expansion. As the confocal microscope is sensitive to movement of the sample of under 1 µm it is inevitable that any heating will move the sample off focus and have a significant effect on the fluoresence signal. To counteract this, the sample must be automatically tracked by a fast focusing technique throughout changes in magnetic field until a steady average power has been reached and the sample drift has reduced to near zero. The essential auto-focus system is discussed in Section 3.5.4. Average heat dissipation could also be reduced for magnetic coils with such a small inductance by reducing the current duty cycle although this may further reduce the shot repetition time.

3.7.5 Higher fields with limited heating

By synchronising measurements with a reduced magnet duty cycle, the average power dissipated as heat can be reduced. For some measurements, alternating zero field and finite field measurements can be usefully exploited as long as an adequate shot repetition rate can be sustained. As the confocal microscope is designed for low-temperature work, the heating effects in resistive coils are also greatly reduced by operation at low temperatures. The cooling power of liquid nitrogen would be ideal. For liquid helium temperature experiments such as entanglement of qubits however any heating is undesirable. In this case a bi-metal niobium-copper magnet wire would provide a method of eliminating the resistive heat loss at the sample when operating at 4 K, driven in series with the same resistive drive circuitry. The limit in this case would be the critical field strength at liquid helium temperature.

3.7.6 Schema for determining orientation of magnetic field

As discussed previously in Section 3.7.1 it is necessary to align the magnetic field to the symmetry axis of each NV^-. One method would be to perform a complete continuous wave ODMR scan for several orientations of the field and deduce the orientation approximately by fitting the resonance dips and deducing the NV^- orientation by vector magnetometry. However for a single NV^- accumulating an ODMR spectrum with an adequate signal to noise ratio to reliably identify the resonance positions for one orientation will take minutes.

Using the magneto-optical dimming effect to find the orientation where no dimming occurs gives a more refined alignment and forgoes the need to additionally scan the microwave excitation frequency. Rotating the magnetic field around the sphere to map the brightness for a constant field of more than 10 mT will give some contrast, however the detected brightness is also highly sensitive to sample drift. Movements of a few hundred nanometres out of focus can halve the fluoresence signal. Unfortunately this means that thermal expansion due to the difference in heat dissipated by the coils and stage drift can prevent direct mapping of the fluoresence around the sphere. Both the heat dissipation and focal drift can be compensated for significantly by instead measuring a differential signal. As the fluoresence emission is still at single-photon counting intensity an accumulated signal is still required but by turning the magnetic field on and off the difference in brightness with and without a magnetic field can be measured for each orientation. This both reduces the average current and hence average heat dissipation and isolates the differential magneto-optical brightness from other effects. As a count rate can be determined in a fraction of a second the complete sphere can be mapped at 10° intervals in 10-20 minutes, followed by a further refinement and peak fitting over a smaller range and finally confirmation with an ODMR scan to determine the exact microwave frequency required for the resonance transition.

3.7.7 Ensemble magnetometry

The effectiveness of the magnet system was initially assessed on a bulk diamond plate with a moderately high concentration of NV^-. This removes the dependence on tracking fluoresence of a point source with the confocal volume and presents all four orientations of NV^-, showing all six resonances.

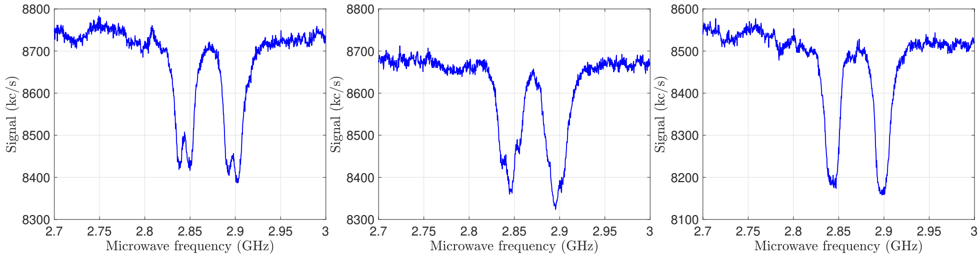

Figure 3.19: ODMR spectra of a bulk, high concentration NV^- plate with 60 mA applied to the X, Y, and Z coils respectively.

Applying 60 mA to each coil separately Figure 3.19, there is a clear difference in the spectra. With a [100] orientated plate this field would not be expected to align to the axes of any of the NV^- populations. A more likely orientation for alignment would be a field applied parallel to one of the [111] directions or possibly [110]. By applying a similar current to all three coils (I_x = 50 mA, I_y = 50 mA, I_z = 60 mA) a field of at least approximately 6 mT. The maximum Zeeman splitting with this field Figure 3.20 was 170 MHz. If the field were fully aligned to one of the NV^- orientation the gyromagnetic ratio

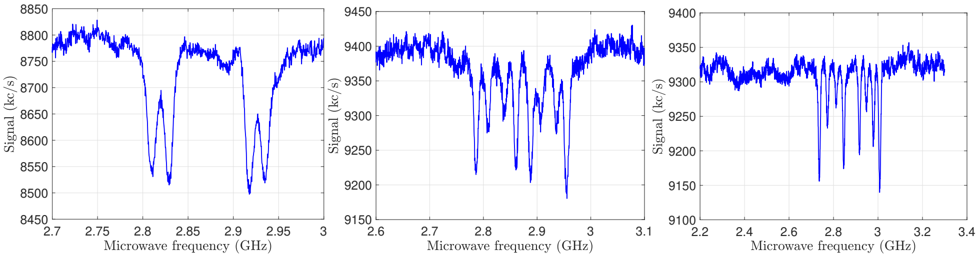

Figure 3.20: ODMR spectra of a bulk, high concentration NV$^-$ plate at room temperature showing up to eight resonances, symmetric about 2.87 GHz, corresponding to Zeeman splitting of the four crystallographic orientations of NV$^-$. The magnet coil currents being applied are respectively I_x = 60 mA, I_y = 0 mA, I_z = 60 mA; I_x = 50 mA, I_y = 50 mA, I_z = 60 mA; I_x = 100 mA, I_y = 80 mA, I_z = 80 mA.

of 28 GHz T^{-1} and broadest splitting of 170 MHz would imply a magnetic field strength of about 6 mT. This is consistent with the modelled field strength of the electromagnetic coils.

3.8 Microwave control

After initialisation, spin manipulations are performed using microwave pulses to drive the ground level spin state of NV^- using one of the available transitions. Pulse lengths are typically 10 ns to 200 ns in length so switching with a fast rise time of less than 10 ns and a high exclusion ratio is a essential. Additionally two or four orthogonal phases are needed to implement dynamic decoupling protocols such as XY8-4. To be capable of generating a strong enough spin manipulation field B_1 to allow for a $\pi/2$ rotation in 100 ns without using a resonator a high input power is required so the applied microwave field was amplified using an Amplifier Research 25S1G6 amplifier. Whilst a resonator would improve efficiency, their use is complicated by several factors. In a cryostat, the geometry will change at low temperatures - complicating tuning. The frequency required to excite transitions can also vary by at least ±300 MHz. Finally for pulsed protocols ring down of the resonator can put a lower limit on the practical pulse length that can be applied so that any resonator would in any case need a low resonator quality factor (Q), limiting any advantage.

To apply suitable pulses the output of a Keysight N5172B microwave source (used as a straightforward continuous output source without modulation or pulsing) was split into two orthogonal phases using a MiniCircuits ZX10Q-2-34-S+ 90° 2-way power splitter Figure 3.21. These phases were controlled by separate high-isolation, fast (5 ns to 10 ns) microwave switches (MiniCircuits ZASWA-2-50DR+) to provide spin rotations in the rotating frame in two orthogonal directions (+X and +Y). $\pi/2$ rotations in the -X and -Y directions were implemented as $3\pi/2$ length pulses in the +X and +Y phases respectively. The difference in bandwidth of the two pulses should not affect

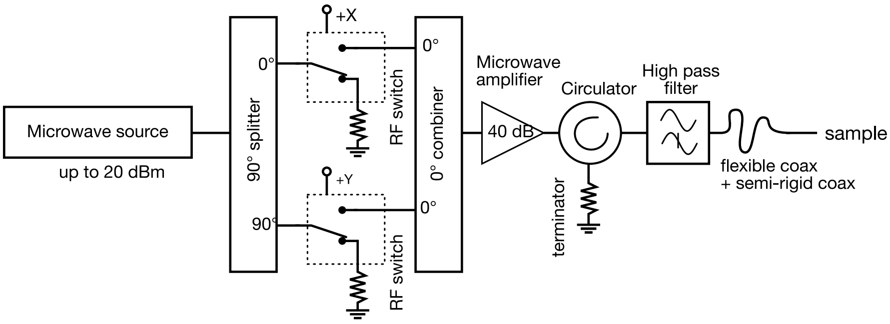

Figure 3.21: Circuit diagram of the microwave delivery subsystem. Pulsed ODMR protocols can be implemented using either one phase of pulse (+X) or in combination with an orthogonal phase of pulse (+Y). If (-X) and (-Y) rotations are required these can be adequately be implemented as a 270° rotation in the positive direction at the cost of a reduction in bandwidth of the pulse. This is not a significant problem when operating on single spins which do not require excitation of multiple spin packets.

operations on single spins (as opposed to spin packets). The two phases are then recombined with a MiniCircuits ZX10-2-42-S+ 0° power splitter before amplification with a Amplifier Research 25S1G6 25 W, 44 dBm microwave amplifier (maximum input 0 dBm). The amplified pulses are delivered through a Pasternack PE8401 circulator, so that reflections from the short-circuit microwave delivery are mostly absorbed by a 50 Ω terminator. Additionally a high-pass filter removes any RF component coupled from the RF loop antenna.

3.8.1 Microwave delivery considerations

The microwave field strength applied to the NV$^-$ of interest determines how long a microwave pulse needs to be to drive the electron spin between states (as seen in Rabi oscillations). The length of pulses not only determines the shot repetition time and hence the sampling rate of measurements. The length of these pulses also determines their bandwidth which can be important to excite all spins in an ensemble.

As many target sites will need to be visited, a sufficiently high field strength is required over an area of interest. A similar B_1 field strength across the visited sites would be preferrable, so that experiments are comparable in terms of pulse length and repetition rate.

Given the physical constraints on the sample space, several sufficiently flat options present themselves. A resonant structure such as a ring cavity, a directly driven wire stretched close to the surface or a directly driven planar structure.

A resonant structure such as a ring resonator could be an efficient way to increase B_1 field strength over a region however as the resonator quality factor (Q) of the resonant cavity increases this constrains the range of frequencies that can be applied, due to the reduced cavity bandwidth. A cavity with lower losses would also have a longer ring-down period which would limit the minimum duration of pulses. Whilst a "spoiled" cavity with a $Q < 10$ might be useful for increasing B_1 and reducing the Rabi period, the problem of choosing or tuning the resonator in-situ with different samples dielectric loads at cryogenic temperatures would add significant complexity. Achieving sufficient B_1 without a cavity would be preferrable for these reasons.

As an aside, whilst we colloquially refer to the microwave delivery structure as an "antenna" the goal is not to couple the microwave energy into free space. In effect what is required is a time-varying magnetic field at the NV^- of interest. To determine the field strength required with an non-resonant structure the time varying aspect can also be disregarded and the conductor considered as a DC system for the purposes of calculating field strength over the region.

Even if a relatively large area of a diamond or silicon sample must be searched for suitable targets for study, the region of interest is small compared to the $\sim$100 mm wavelength microwaves applied so non-resonant structures with a scale up to ~10 mm can be considered instantaneously as carrying DC current without significant variation in microwave phase across the structure. Typically, the microwave current needs to pass within 50 µm to 200 µm of the NV^- being studied to be effective.

Two main approaches were used: stretched wire and planar current loops.

Putting a printed circuit board (PCB) current loop underneath the sample was optimistic, as samples are typically 300 µm thick. Standard "thin" PCB is also too thick to look through for limited clearance under a microscope objective. Copper on 85 µm thick polyamide film current loops Figure 3.22 were made however fixing the antenna in place rigidly for cryogenic operation was another difficulty.

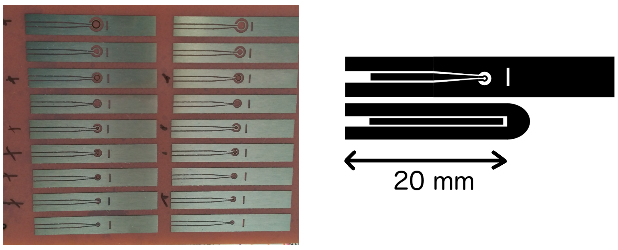

Figure 3.22: Omega loop antennas with tapered CPW feeds on polyamide film, thin enough to focus through - holes have been inscribed by Mareike Hermann using a laser machining system for this purpose. Detail of a 1 mm omega loop mask and CPW pads for stretching a wire over a sample.

3.8.2 Microwave waveguides

To deliver ~3 GHz microwaves to the NV^- being studied, the probe has an sub-miniature A (SMA) pass-through into the cryostat leading to one of two semi-rigid coaxial feeds to a few centimetres above the sample space. The sample is moved on a piezo-positioner stack and stability of the order of 100 nm is required so force applied to the sample holder from the flexible portion of the microwave feed has to be minimised. This is achieved by selecting a thin, flexible coaxial cable and having a selection of lengths varying by 5 mm. An additional difficulty is the limited volume available by the sample, which prevents the use of SMA or sub-miniature B (SMB) connectors. Instead limited-detent, miniature sub-miniature push-on (SMP) connectors were used to transition from flexible feed to a CPW on copper PCB to the sample.

The dimensions of CPW used were calculated for a $50\,\Omega$ impedance at 3 GHz using [178] however as the CPW is terminated with a short connection, the losses due to impedance mismatch across this transition are insignificant.

3.8.3 RF delivery

In addition to supporting the pulsed microwave delivery needed for single frequency AC magnetometry of nearby spins selected by controlling the period of dynamic decoupling pulse sequences, a secondary RF feed and wound loop antenna was recessed into the brass sample holder. Separating the feeds rather than mixing the two channels allowed use of appropriate frequency band components and any cross-talk could be filtered. As the instrument was designed for use at low magnetic fields, the RF antenna was added in preparation for multi-spin experiments with both electron spins in low ZFS environments such as those associated with dopant electrons in silicon, nearby trapped electron spins (using double electron–electron resonance (DEER)) or nearby nitrogen or ^{13}C nuclear spins (using electron nuclear double resonance (ENDOR)).

3.9 Silicon sample holders

Nanodiamonds are typically not directly visible under confocal microscopy as resolution is limited to around 300 nm. Clusters of relatively large, micron scale particles can be crudely imaged with confocal microscopy but spatial localisation beyond the diffraction limit depends on the concentrations of NV^- being sufficiently low such that some individual nanoparticles contain only one NV^-. Highly localised NV^- emission can be detected with confocal microscopy but to measure the size and composition of the nanodiamonds they occur in higher resolution electron microscopy is required. Techniques such as energy dispersive X-ray analysis (EDAX) can also provide confirmation of the composition of nanodiamonds and identify some contaminants. Whilst these silicon sample plates are not suitable for higher resolution TEM but they do enable 100 nm scale imaging with SEM which allows true nanodiamonds smaller than the optical wavelengths used to be differentiated from contaminants or larger particles.

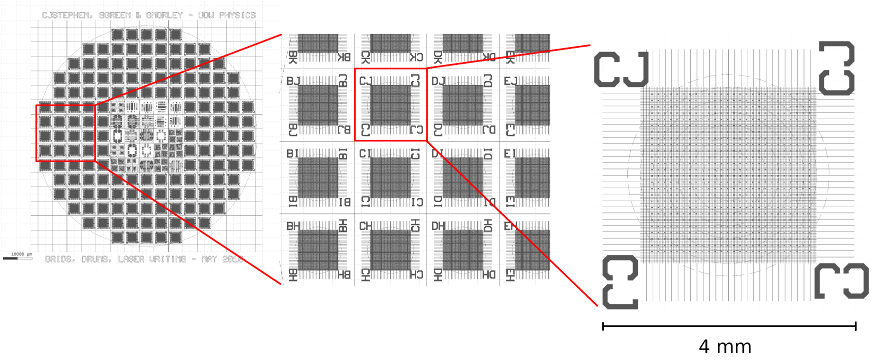

Figure 3.23: The lithographic mask used to make the sample grids. The pattern was etched into silicon to give contrast in both CFM and SEM. Each cell has a unique two letter label. The patterns in the centre of the wafer were for other projects.

These grids were etched into silicon with sufficient depth (around 2 µm) to have excellent constrast using optical confocal microscopy of reflected light without requiring deposition of any metal on the surface. The two letter labels allow individual sample substrates and nanodiamonds to be referred to by an address such as “CJMK41” in records so that the sites to be clearly identified in both CFM and SEM imaging. Over a hundred uniquely identifiable sample grids can be fabricated on a wafer Figure 3.23.

To navigate the sample repeatably in SEM and CFM imaging the grids were designed with heirarchical structure Figure 3.23 using KLayout[179] and Ruby scripts in industry standard GDS II format with 1 µm lines marking out 25 µm boxes Figure 3.24 layed out in labelled grids.

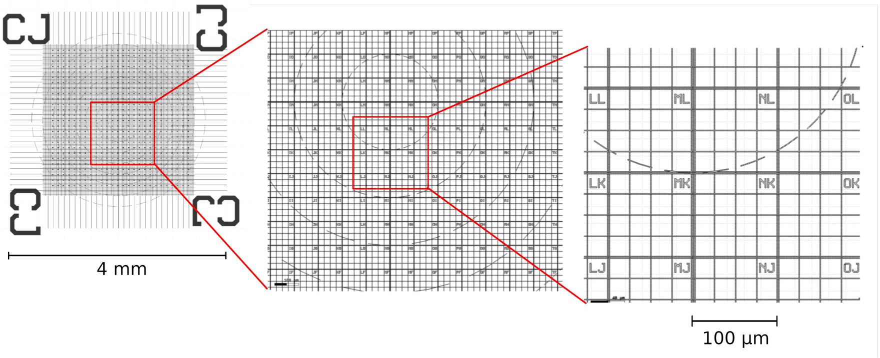

Figure 3.24: Detailed view of an individual sample grid for recording nanodiamond position. Each has a unique two letter label.

The large lettering on each 5 mm × 5 mm sample grid Figure 3.24 is cross-hatched to create contrast that is visible by eye. Concentric rings give an indication of the direction to the centre of each sample grid. A second layer of two letter code identifies each 100 µm square in lettering that is legible in confocal microscopy or SEM. Each grid is subdivided into 25 µm squares so a reference line is always visible even with the limited 30 µm scan range of the Attocube piezo scanning stage at low temperature.

A 4” quartz mask was made to this design by JD Photo Data and

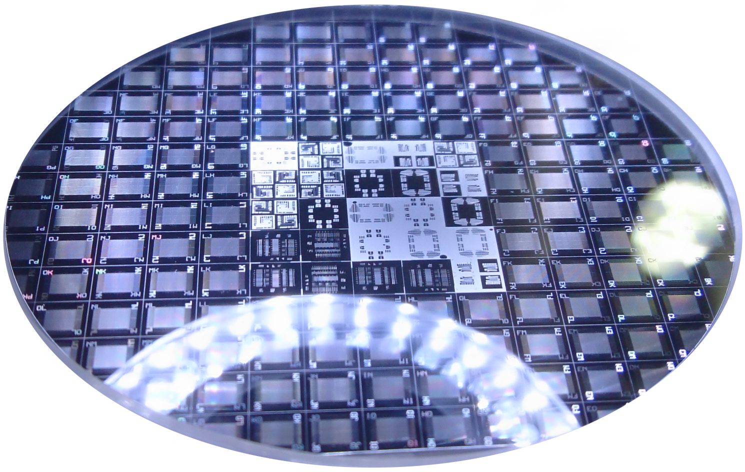

Figure 3.25: Photograph (by Yashna Lekhai) of an etched silicon wafer of sample grids.

used in the Department of Engineering clean room to transfer the design to a 3" silicon wafer lithographically and to etch the grid pattern. This produced around one hundred uniquely labelled, easily detachable sample grids with the loss of only a small fraction of the polished silicon surface area. No metallisation was required, avoiding problems with surface contamination and conduction. The two letter labels at the microscopic scale are small enough to identify 100 µm grid cells and large letters striped with diffracting wavelength-scale cross-hatched lines provide easy sample identification by eye without magnification Figure 3.25. Work using these grids to combine SEM imaging, EDAX and confocal measurements in the characterisation of nanodiamonds has subsequently been presented by Guy Stimpson.

As a test prior to fabrication, a piece of silicon was marked using a FIB to see if the depth contrast of markings at approximately the 1 µm scale available for lithography would be visible with reflection confocal microscopy without adding metallisation. Whilst the test square is barely visible under

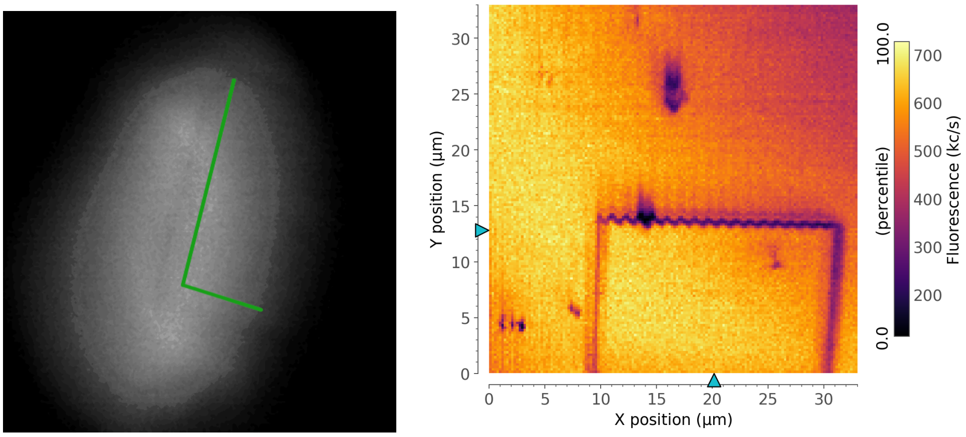

Figure 3.26: *(left)* Enhanced wide-field image of the corner of a FIB etched square captured using the orientation camera under white illumination (two faint dark lines can just be seen parallel to the green markings). *(right)* The same region imaged using scanning confocal microscopy in reflection mode.

white light illumination on the camera in Figure 3.26 (two faint dark lines and a corner can just be made out when moving), the contrast is clear using reflection confocal imaging on the fibre confocal microscope (at room temperature) using an attenuated red laser source instead of the heavily filtered green excitation source. The sawtooth anomaly seen on the confocal image was later reduced by slowing the scan rate.

Chapter 4

Laser written NV^-

4.1 Introduction

In parallel to the development of the fibre-coupled cryogenic confocal microscope for sensing within silicon, I was involved increasingly in an NQIT collaboration developing laser-writing of NV^- centres in diamond. In the first iteration of this work, I annealed the sample in our tube furnace under diamond grit in the work which led to the first paper on laser writing of single NV^-. Through my involvement in the conference calls with the NQIT collaboration I learned of Patrick Salter's other work on graphitic "wires" in diamond and it troubled me that and proposed several My contributions included planning the 3-d array experiment, planning the laser written 3-d electrode experiments, producing detailed plans for the laser writing fabrication, annealing samples, acid cleaning, producing lithographic masks, running confocal microscopy & ODMR experiments, adding automation and extending the capability of the room-temperature confocal microscope.

In this chapter I will set out what the laser writing process entailed in this work; the apparatus used to make these measurements and the results. Prior work and the laser writing system is discussed in Section 2.4. I will also briefly describe the work done on subsequent stage which was unfortunately curtailed due to loss of the sample at an advanced stage in Section 5.3.1 as this work is ongoing.

4.1.1 Background

The creation of deterministically located NV^- using the laser writing method was first studied in work with Jason Smith's group in University of Oxford[28]. The initial work in this area by Larry Chen and others[28] created arrays with a gradient of pulse energy at a depth of 50 µm to determine if the process could generate vacancies and transmute these into NV$^-$. This work was followed up with a series of work on an electronic grade CVD plate to attempt NV$^-$ creation at different depths and to see if NV$^-$ could be created between electrodes as an attempt to better understand the process Figure 4.1.

Nitrogen vacancy centres (NV$^-$) in diamond show promise for quantum computing[11–14, 92], communication[11, 93, 147] and nanoscale sensing[8, 111–113]. Demonstrated qubit fidelities[12] for a single NV$^-$ and its nearby nuclear spins are above the required thresholds for quantum computing[7]. In addition, two NV$^-$ in different cryostats have been optically entangled[8, 11]. The single NV$^-$ in that work were 5 µm to 15 µm deep to allow solid immersion lenses to be fabricated around them and they were not deliberately placed but were found after searching. This work shows that single NV$^-$ can be laser-written 6 µm to 15 µm deep inside of diamond in three-dimensional arrays with spin coherence times that are an order of magnitude longer than previous laser-written NVCs[28] and at least as long as naturally-occurring NV$^-$ [92]. This could allow over 100,000 NV$^-$ in a two-dimensional array inside a commercially available 4.5 mm × 4.5 mm × 0.5 mm diamond with five nuclear qubits per NV$^-$ [13, 14] and allow 10 µm separation of NV$^-$ to leave room for the laser-written electrical control Section 5.3.1.

The large arrays of NV$^-$ in this work are not the largest that have been made[130] however these arrays have a high yield of *single* NV$^-$ and demonstrate layering into three-dimensional stacks. The precision of depth control is compared to that achieved using a delta-doped layer[126] in Section 4.4.5. The coherence properties of the NV$^-$ created and measured in this work, presented in Section 4.4.7, are exceptionally good for NV$^-$ in diamond with a natural abundance of ^{13}C.

4.1.2 First iteration of laser writing

In the first attempt to improve our understanding of the process, 5 arrays of 420 points at 5 µm pitch were written into an electronic grade diamond at depths 4, 8, 15, 20 and 24 µm with a range of pulse energies between 13 nJ and 50 nJ with 80 nJ marker pulses in an attempt to discover if there was any pattern to the yield of single NV^-. This range of pulse energies proved to be too broad so that most sites developed many NV^- and a few rows developed none. A second fabrication series of three such arrays were written with a narrower range of pulse energies - 5.2 nJ to 33 nJ at depths of 5, 10 and 20 µm. Only a handful of these sites formed single NV^- at all and so these were also ineffectual in providing data on the process beyond the realisation that this highly non-linear, many photon process is sensitive to variations in pulse power of a few nanojoules and to fine tuning of the writing conditions. This was compensated for in the large array work by writing calibration sites on the day of fabrication to narrow the conditions required as described in Section 4.2.

Additionally on this diamond, three “ladder” structures Figure 4.2 were created by Patrick Salter to look at what happens if you laser write single NV^- between the tips of laser written probe wires. Surface contact pads were attached to these probe rails and exposed at the surface. Lithographic masks were created to pattern metal contacts onto the subcutaneous wires however extensive problems with spin-coating photosensitive resist onto an 2 mm diamond, with adhesion of titanium and gold to the surface and with gold “lift off” stymied this part of the project. This work has been carried on by Yashna Lekhai as more information on the behaviour of “graphitic” wires in diamond would be valuable.

With so few sites developing NV^- insufficient information was gained

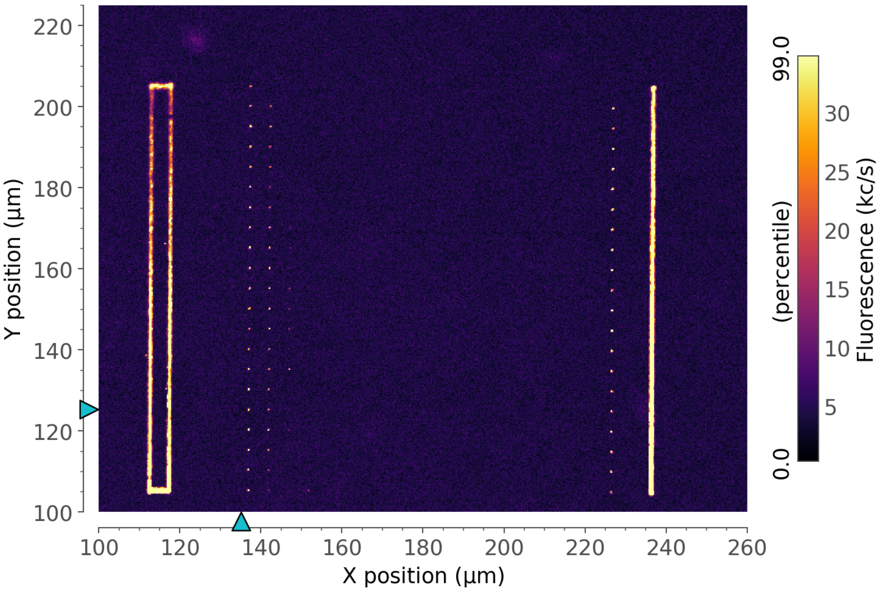

Figure 4.1: Confocal fluorescence microscopy image of array H from the second laser writing iteration with marker lines.

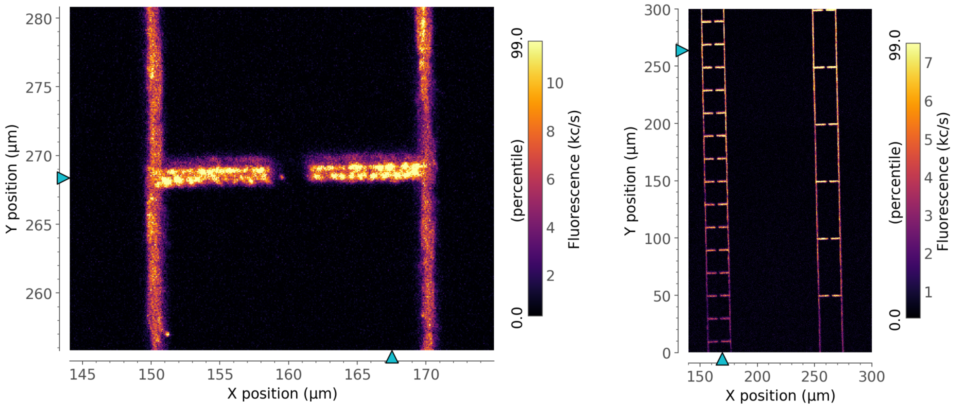

Figure 4.2: Confocal fluorescence microscopy images from the first diamond of *(left)* the electrode "ladder" structures *(right)* an NV$^-$ site between electrodes. This sample was subsequently used for testing deposition of metal contacts.

on the NV^- and vacancy creation process in these small test arrays Figure 4.1 so a further larger study was planned to answer the questions that remained: could NV^- be created reliably at other, shallower depths; what limited their coherence lifetime; was the probability of forming a single NV^- at a writing site dependent on an unseen variation in properties of electronic-grade CVD diamond at the micrometre length scale; how far away from their planned location are the created NV^- sites formed; does the proximity of other writing sites have any effect; can the laser-written NV^- be combined with laser-written wiring to start to form the basis for "integrated circuits" in diamond in two or three dimensions? A much larger sample of laser written NV^- sites would reveal more statistically significant information on their properties & the fabrication process as a basis for refinement of the technique. Additionally, the capability to produce large arrays of single NV^- at pre-determined positions is clearly a potential building block for large-scale, many-qubit arrays using NV^- in diamond. The work that follows is based on the work on the laser-written arrays such as those shown in Figure 4.3 of finely varied pulse energy and pitch over a wide region of an electronic-grade diamond Figure 4.5.

4.1.3 Second iteration of laser writing

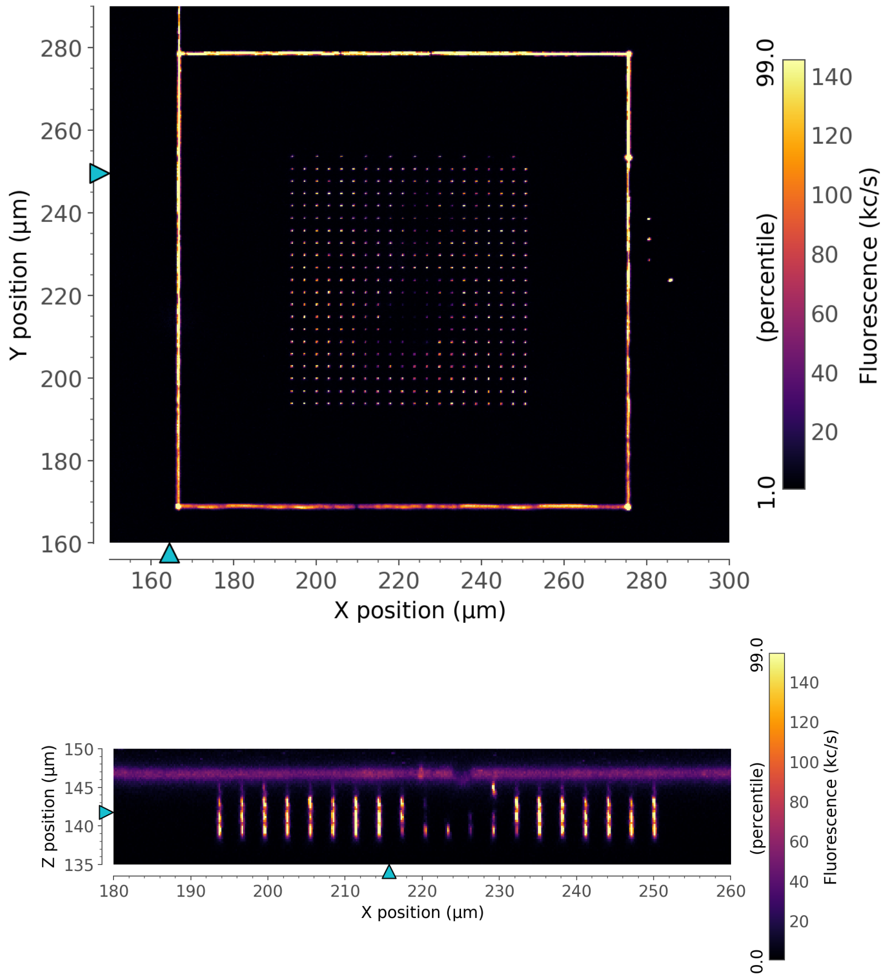

Figure 4.3: Confocal fluorescence microscopy images of *(top)* an array with marker frame *(bottom)* a depth cross section through the stack of arrays, from array H in the main work prior to annealing.

The laser writing for each iteration of this work was done by Patrick Salter. Laiyi Weng used the University of Oxford confocal microscope to assist by making calibration measurements of test writing on a matching diamond on the day of writing for this latest iteration, determining the threshold of visibility of the vacancy clusters as an approximation of the required pulse energy.

4.1.4 Laser written wires

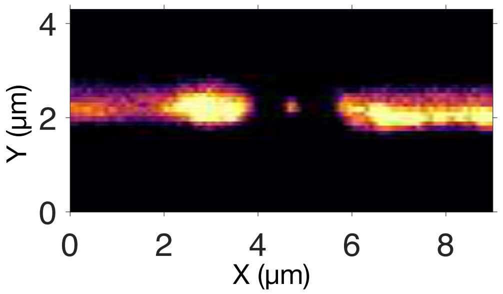

Figure 4.4: NV$^-$ between laser written electrodes in another region of the three-dimensional array diamond.

Additionally to the three dimensional arrays of NV$^-$, several forms of electrodes Figure 4.4 were created around NV$^-$ using laser writing. As this work was incomplete, some details are provided in the appendix. Previous NV$^-$ optical entanglement work has applied electric fields to Stark shift the optical fluorescence frequency so that the two NV$^-$ have indistinguishable emission[11, 92]. Figure 4.4 shows an NV$^-$ between two electrically-conducting wires that were laser-written in 3-d at the same time as the arrays. It is known that these laser-written wires in diamond are graphitic and that they conduct with a DC resistivity of around $0.1\,\Omega - \text{cm}$ at room temperature[29]. This demonstrates creation of long-lived spin qubits in a solid-state system with alignment to control structures in three dimensions inside diamond, making this a compelling approach for engineering larger quantum systems.

4.1.5 Applications

Useful fault-tolerant quantum computing will require at least 100,000 physical qubits and perhaps one billion[7]. It will not be practical to build this with one cryostat per NV$^-$ so it is important to consider how many NV$^-$ can be used inside of one diamond, inspired by previous theoretical proposals[3, 5, 7, 51]. For communications, having an array of NV^- would provide many spin-photon interfaces within one cryostat[147], increasing data rates and allowing multiplexing. Sensing with 2-d arrays of NV^- could combine the high resolution of single NV^- sensing[8] with the simultaneous imaging achieved with wide-field microscopy[111]. Stacking two 2-d arrays could increase sensitivity by subtracting the background noise measured by the array that is further from the sample of interest.

For all these technologies, a fibre array or a spatial light modulator (SLM) that sends and receives optical photons to and from a 2-d array of NV^- simultaneously, through a lens or a microlens array would be enabled by control of NV^- fabrication. A SIL array aligned to the laser-written NV^- could be fabricated to collect more of the fluorescence[11, 92]. For sensing, the NV^- need to be 10 nm from the surface (without a SIL). This technique could be used with δ-doping of nitrogen to control the depth of NV^- with a precision of 4 nm [133], followed by plasma etching to leave them at the surface.

4.1.6 Previous NV^- fabrication work

The creation of two dimensional NV^- arrays has been demonstrated previously[28, 127, 128, 133], but not below 1 µm depth and not in three dimensions. With ion implantation through a mask, high-precision placement of 10 nm[128] has been shown, and electron spin T_2 times of up to 50 µs. Longer T_2 times of up to 530 µs were achieved by using isotopically pure ^{12}C diamond but with less precise placement and again requiring ion implantation through a mask[127]. For quantum computing it is important to use diamond with natural isotopic abundance because the 1.1% ^{13}C nuclear spins provide a valuable register of around five qubits that can be used to store quantum information for longer than the electron spin. Localised electron irradiation into a diamond provided a 2-d array with T_2 of up to 1.3 ms due to the use of ^{12}C diamond, and no need for a mask[133]. This used delta doping to reach a depth precision of 4 nm, with in-plane precision of 450 nm. Laser-written optical waveguides have been made in diamond and ODMR measured on the NV^- ensembles inside[180]. 2-d arrays of NV^- ensembles have been created on the surface with nanoablation[181]. It has been shown that 2-d arrays of single/double/triple NV^- can be laser written with no mask, but the T_2 time measured was typically only 30 µs to 80 µs[28]. A new paper describes preferential orientation and near-100% yield for 5×5 2-d arrays of laser-written NV^- in diamond[36].

4.2 Fabrication of laser written arrays

4.2.1 Surface etching

An electronic grade diamond of [100] orientation was bought from Element Six and cleaned of any organic contaminants using a piranha solution. A solvent rinse was used to remove any residual piranha and the surface preparation completed using a high temperature O_2 plasma ash prior to etching. $Ar-Cl_2$ inductively coupled plasma (ICP) was used to remove the sub-surface polishing damage by etching the top 15 µm of diamond along with any sub-surface polishing damage[113]. This was followed by a 5 µm etch in pure O_2 to maintain NV^- fluorescence by removing any implanted chlorine [113, 182]. The etching work was performed by Paul Hill in Erdan Gu's group at the Institute of Photonics at University of Strathclyde as part of the NQIT collaboration.

4.2.2 Surface cleaning between steps

Before each microscopy run, the surface was cleaned for 30 minutes in a hot acid solution of concentrated sulphuric acid with potassium nitrate. Any residue of potassium nitrate was removed with a second clean in sulphuric acid alone before rinsing in Milli-Q purified water. These steps would remove most fluorescent, organic contaminants from on the surface (such as from immersion oil) and oxygen terminate the surface. Surface termination was not thought to be critical in this experiment as by design even the shallowest NV^- were created in the more stable environment a few microns inside the bulk. For shallow imaging, a slow, in-situ, high-intensity surface scan with 4 mW of laser power (with the detection arm of the confocal microscope blocked) was used to photo-bleach the surface to improve the contrast of the shallowest NV^-.

4.2.3 Laser writing

The laser writing used in this work was performed by Patrick Salter at the University of Oxford based on detailed plans I drew up after discussion with members of the NQIT collaboration. The pulses from a regeneratively amplified Ti:Sapphire laser (SpectraPhysics Solstice, wavelength 790 nm) were focused inside the diamond using an oil immersion objective lens (Olympus 60x, 1.4 NA). Adaptive optics using a liquid crystal SLM (Hamamatsu X10468-02) was used to correct for the aberration[33], ensuring that the fabrication was the same at each depth beneath the diamond surface. The diamond sample was mounted on a three-axis precision translation stage (Aerotech ABL10100, ANT95-3) and moved relative to the laser focus to fabricate discrete vacancy ensembles, each with a single pulse from the laser. All pulse energies stated are those measured prior to the objective, where in addition the laser pulse duration was measured as 250 fs.

Arrays of ensembles of vacancies were generated in the diamond lattice by single 250 fs pulses from the 790 nm laser focused tightly beneath the surface of the diamond using a 1.4 NA oil objective. The light matter interaction is highly non-linear, limiting any material modification to the centre of the focal volume and giving an inherent three-dimensional resolution to the fabrication[31]. The refractive index mismatch at the oil-diamond interface causes refraction leading to a depth dependent spherical aberration of the laser focus, which can limit three-dimensional fabrication resolution. Adaptive optics using a liquid crystal SLM were used to correct for the aberration[33], ensuring that the fabrication was the same at each depth. The full-width-half-maxima of the intensity distribution of the laser focus inside the diamond are estimated to be 350 nm radially and 1.7 µm longitudinally[28]. However, the expected dimensions over which the light matter interaction is appreciable are likely to be much lower[34]. The diamond sample was mounted on a three axis precision translation stage and moved relative to the laser focus to fabricate arrays of vacancy ensembles.

In order to find the fine range of pulse energies to use in these experiments, an initial calibration study was carried out by Laiyi Weng on the day of fabrication of the arrays. A number of sites were laser written into a nominally identical diamond with a coarse range of pulse energies and then imaged by measured by Laiyi Weng using a scanning confocal microscope. This determined the pulse energy that produced just-visible vacancy ensembles using an air objective. Previous work has shown that write-pulse energies slightly lower than this are optimal for NV^- creation[28]. Twenty-two 3-d arrays labelled A to V were laser written with different energies from 14 nJ to 19 nJ and with different pitches from 2 µm to 5 µm, with each 3-d array having 21×20 2-d arrays stacked with up to six depths for a total of over 44,000 writing sites.

4.2.4 Array creation parameters

Arrays A to G were fabricated as six layers at depths of 5, 10, 15, 20, 25 and 30 µm. Each layer was written with 410 pulses in 20 rows and 21 columns of consistent pulse energy with a pitch of 5 µm. The write pulse energies of arrays A to G were respectively: 19, 18, 17, 16, 15, 14 and 18 nJ.

Arrays H to N were fabricated as five layers at depths of 3, 6, 9, 12 and 15 µm. Each layer was written with 410 pulses in 20 rows and 21 columns of consistent pulse energy with a pitch of 3 µm. The write pulse energies of arrays H to N were respectively: 18, 17, 16, 15, 14, 17.5 and 18 nJ.

Arrays O to V were fabricated as four layers at depths of 4, 6, 8 and 10 µm. Each layer was written with 410 pulses in 20 rows and 21 columns of consistent pulse energy with a pitch of 2 µm. The write pulse energies of arrays O to V were respectively: 18, 17, 16, 15, 14, 16, 16.5 and 17 nJ.

The labelling of the arrays is shown in Figure 4.5.

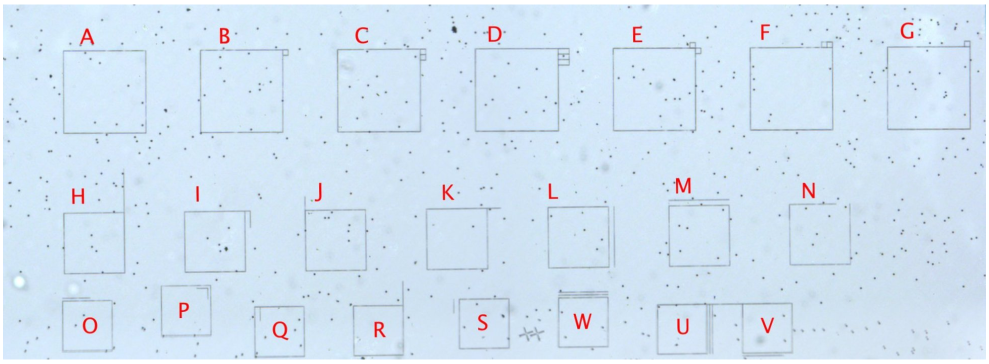

Figure 4.5: Wide field transmission microscopy of the laser-written markers surrounding the arrays, labelled A to V.

4.2.5 Annealing

Following laser writing and characterisation, the sample was buried in Element Six diamond grit and annealed for three hours at 1000 °C in a tube furnace in a nitrogen atmosphere to convert the introduced vacancies into NVCs[28], as described in Section 2.4. Above ~600 °C single vacancies become mobile by a hopping mechanism, diffusing at a temperature dependent rate until bound.

4.3 Measurement methods

4.3.1 Confocal microscopy

Imaging was performed with a home-built confocal fluorescence microscope using a Laser Quantum Gem 532 (532 nm, 100 mW) laser for excitation controlled through an Isomet 1250C acousto-optic modulator operated with a locally built driver to reduce leakage of excitation light significantly and to enable immediate power control. Unless otherwise specified, a 633 nm long pass filter was used during imaging to eliminate diamond Raman emission. Pinholes were used on both the excitation and detection paths. All imaging used a Zeiss ×100 apochromatic 1.4 NA oil objective. Fluorescence was detected with a pair of Excelitas NIR enhanced single photon avalanche photodiode (SPAD) modules with an efficiency of approximately 70% at 700 nm.

Laser power was controlled using both the control interface for the Laser Quantum Gem (for coarse control) and the home built AOM driver Section 3.4.1 was used for power saturation measurements and fast control. The power delivered to the back aperture of the objective was calibrated Figure 3.8 with a Thorlabs PM100 and configured into the new AOM module in Qudi Section 3.5.4 as an interpolated lookup table.

4.3.2 Optical saturation measurements

Saturation measurements of single colour centres[66, 183] are useful in their characterisation. By varying the excitation laser power whilst measuring the intensity of fluorescence emitted a saturation curve can be fitted Eqn. 4.1 which can tell us whether the source of fluorescence can be saturated with the available power, the maximum detected intensity being approached I_∞ and the (finite) excitation power as saturation is approached P_{sat} (with detected fluorescence $I_\infty/2$).

$$I(P) = I_\infty \frac{P/P_{sat}}{1 + P/P_{sat}} \tag{4.1}$$

Typically not more than around 1% of the total emission of the source can be collected in practice however this collection efficiency is normally constant for a given optical system so this provides useful comparative information on the efficiency of excitation, the saturation behaviour of the source and relative collection efficiency. As saturation is approached the absorption cross-section of the colour centre is limited by the reduced occupancy of the ground state

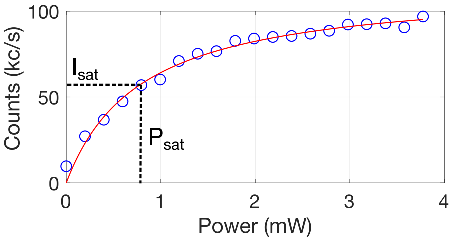

Figure 4.6: Saturation measurement of a typical single NV$^-$ in array M. Fitting to Eqn. 4.1 I_∞ is found to be (115 ± 1) kc/s and P_{sat} (0.79 ± 0.03) mW.

The improved AOM driver enabled P_{sat} measurements to be made and fitted in around 1 s in comparison to a ten minute manual process. Whilst the values of P_{sat} and I_∞ may vary somewhat with the optical efficiency of different microscopes these measurements are useful to confirm that a fluorescing site can be saturated and to allow basic comparisons of the emission of colour centres. Often a P_{sat} measurement can be sufficient to identify potential single NV$^-$ and double NV$^-$ sites if the conditions are well understood with HBT experiments providing confirmation. P_{sat} measurements of a known sample also provide a good indication that a CFM is operating optimally.

4.3.3 Hanbury-Brown Twiss measurements

Fluorescence from the NV^- being measured was split by a non-polarising beam splitter and the autocorrelation of the photon arrival events at two Excelitas NIR enhanced SPAD modules was accumulated using a Swabian Instruments TimeTagger. The data were normalised by the accumulated autocorrelation for large and fitted using the photon arrival time auto-correlation model for a three-level system, with a modification to allow the depth of the dip at $\tau = 0$ to vary as a fit parameter. Some of the internal dynamics of the NV^-, in particular the lifetime of the "shelving" state, can be extracted from the exponential decay of the post-anti-bunching "bump".

The fitted $g^{(2)}(0)$ with measurement uncertainty inferred from the standard deviation of $g^{(2)}(\tau)$ at large was binned into $g^{(2)}(0) < 0.5$ for single NVC, $0.5 \leq g^{(2)}(0) < 0.66$ for double NV^- and $0.66 \leq g^{(2)}(0) < 0.75$ for triple NV^-. Examples are shown in Figure 4.7. The variance in the autocorrelation value at large delay is used to estimate the fractional uncertainty in the fitted $g^{(2)}(0)$. Categorisation of sites by number of emitters according to the $g^{(2)}(0) < 1 - 1/n$ model takes account of this uncertainty estimate. In cases where insufficient light was detected at automatically visited sites, some sites were inspected manually and where pairs of nearby NV^- had confounded the automated focusing these were classified as optically resolved double sites, as were sites where more than one optically distinct NV^- could be seen in confocal imaging of the grid site. The full HBT statistics are shown in Figure 4.13.

4.3.4 Pulsed ODMR measurements

A 20 µm diameter, uncoated copper wire was stretched over arrays H to N Figure 4.8 and microwaves were applied via a coplanar waveguide.

Microwaves from a Keysight N5172B source were split into two phases and controlled independently through two fast, high exclusion switches and recombined using components sourced from MiniCircuits, as shown in Figure 4.9. The combined pulses were amplified by a MiniCircuits ZHL-16W-43-S+ amplifier which was used to drive a 20 µm high purity copper wire short stretched over the sample mounted on a coplanar waveguide into a 50 Ω terminator. A Swabian Instruments PulseStreamer was used to control the timing of pulse sequences.

A permanent magnet was aligned along one of the four orientations of NV^- as a bias field. Coarse alignment was by performed though ODMR followed by minimising the magneto-optical suppression of fluorescence at both low and high fields. With under 1° of misalignment the fluorescence change between low and high fields is minimal. This diamond was found to have the expected (100) surface and [110] sides. Continuous wave ODMR was used to identify sites in this orientation with a resonance at 2.17 GHz.

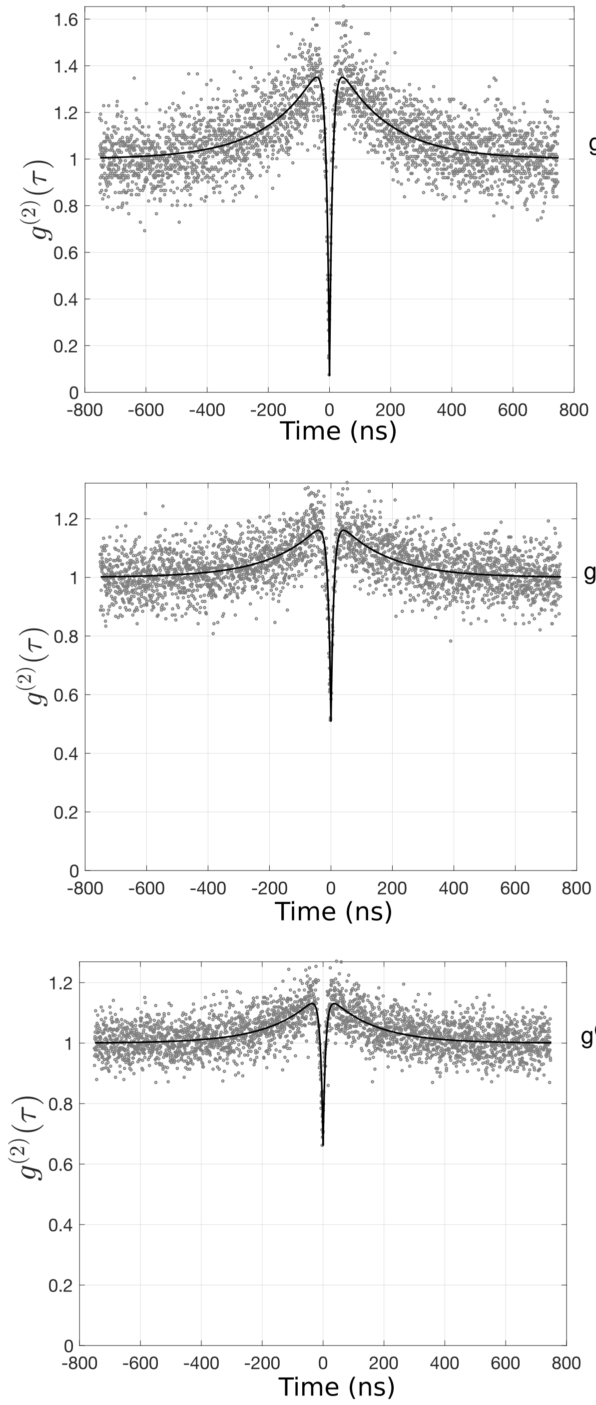

$g^{(2)}(0) = 0.07 \pm 0.01$
→ single emitter

$g^{(2)}(0) = 0.51 \pm 0.04$
→ 2 emitters

$g^{(2)}(0) = 0.66 \pm 0.04$
→ 3 emitters

Figure 4.7: HBT photon arrival time auto-correlation measurements for three NV^- sites in array H showing examples of single, double and triple NV^- classifications. The data has been normalised to the mean auto-correlation value at a delay of $(700 \pm 50)\,\mathrm{ns}$ but no ad-hoc background subtraction is required.

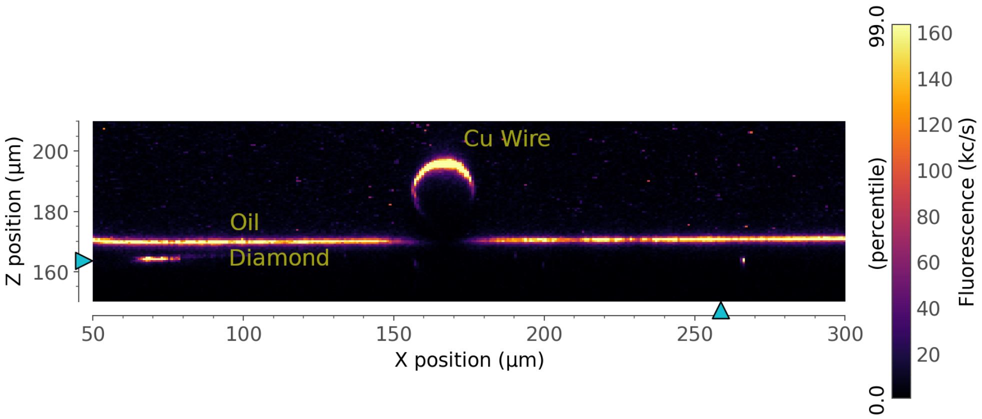

Figure 4.8: A depth section fluorescence confocal microscopy image showing a cross-section through a 20 µm diameter copper wire stretched over the boundary of array M. The bright horizontal line is the diamond surface. Just below the surface, the bright frame lines at the edges of the image and some dim NV$^-$ sites near the wire can be seen at different depths.

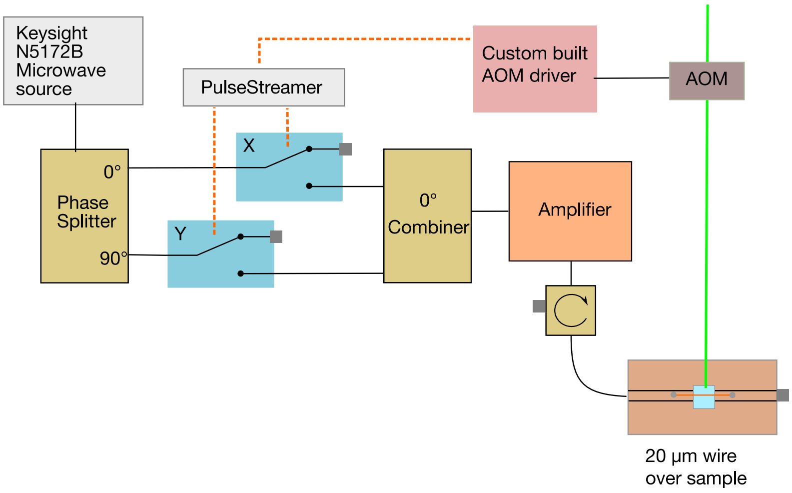

Figure 4.9: Sketch of the microwave and excitation control apparatus (optics omitted).

4.4 Results

The 3-d arrays were created by laser-writing over 2000 NV$^-$ into a diamond with natural isotopic abundance of ^{13}C as shown in Figure 4.10. The spin echo coherence time for 22 of the single NV$^-$ were measured and 15 of them had exceptionally good spin echo coherence times ($T_2 > 500\,\mu s$) at room temperature. All the measurements were made at room temperature where the electron spin coherence time is limited by the natural isotopic abundance of ^{13}C. Dynamic decoupling was used to probe the electron spin coherence without ^{13}C limitations, finding a mean coherence time of (1.7 ± 0.5) ms and apparently limited by the (3.0 ± 0.7) ms electron spin T_1 measured. This is consistent with values of T_2 of 1.6 ms reported for dynamically decoupled NV$^-$ in natural abundance diamond at room temperature[106].

4.4.1 Confocal microscopy of NV$^-$ arrays

Figure 4.10 contains images from the scanning confocal microscope of one of the 3-d arrays (array M) before and after annealing. Before annealing, laser-written spots are visible due to the fluorescence of neutrally charged vacancies (V_0) - lattice sites in the diamond where the carbon atom is missing. This is shown in the top row of Figure 4.10 The characteristic V_0 fluorescence spectrum confirms the identity of these vacancies as shown in Section 4.4.3. None of these pre-anneal spots were visible with an air objective[28] but these images were collected with an oil objective (NA=1.4). After annealing the diamond at 1000 °C for 3 hours in a nitrogen environment[28] and repeating the imaging, the results are shown in the bottom row of Figure 4.10. The spots that can be seen are NV$^-$ as confirmed by the characteristic fluorescence spectrum shown in Section 4.4.3.

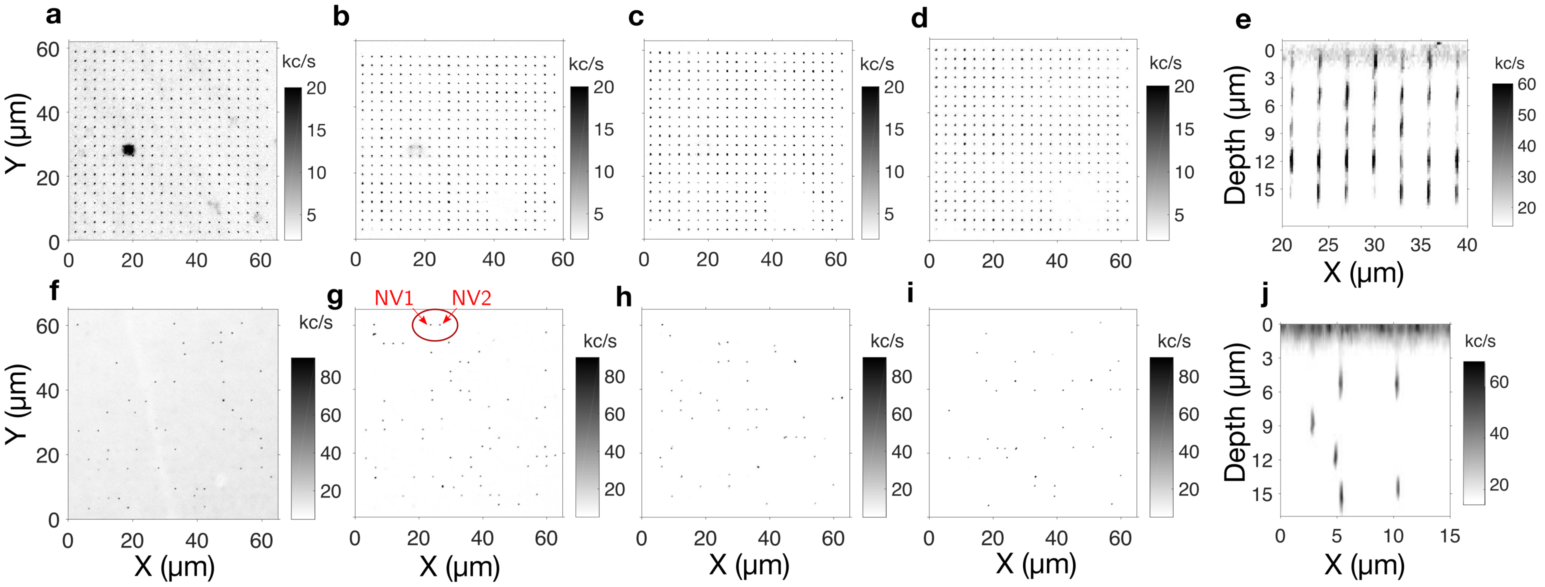

Figure 4.10: Confocal imaging of a three dimensional array of defects in diamond. Top row: a, b, c and d are in the XY plane at depths of 6, 9, 12 and 15 µm respectively before annealing: each spot is an ensemble of vacancies. e is a vertical section in the XZ plane. Bottom row: The same volume after annealing out the vacancies: the spots are NV^-. In 9% of the target sites NV^- were created, almost all as single NV^- (circled).

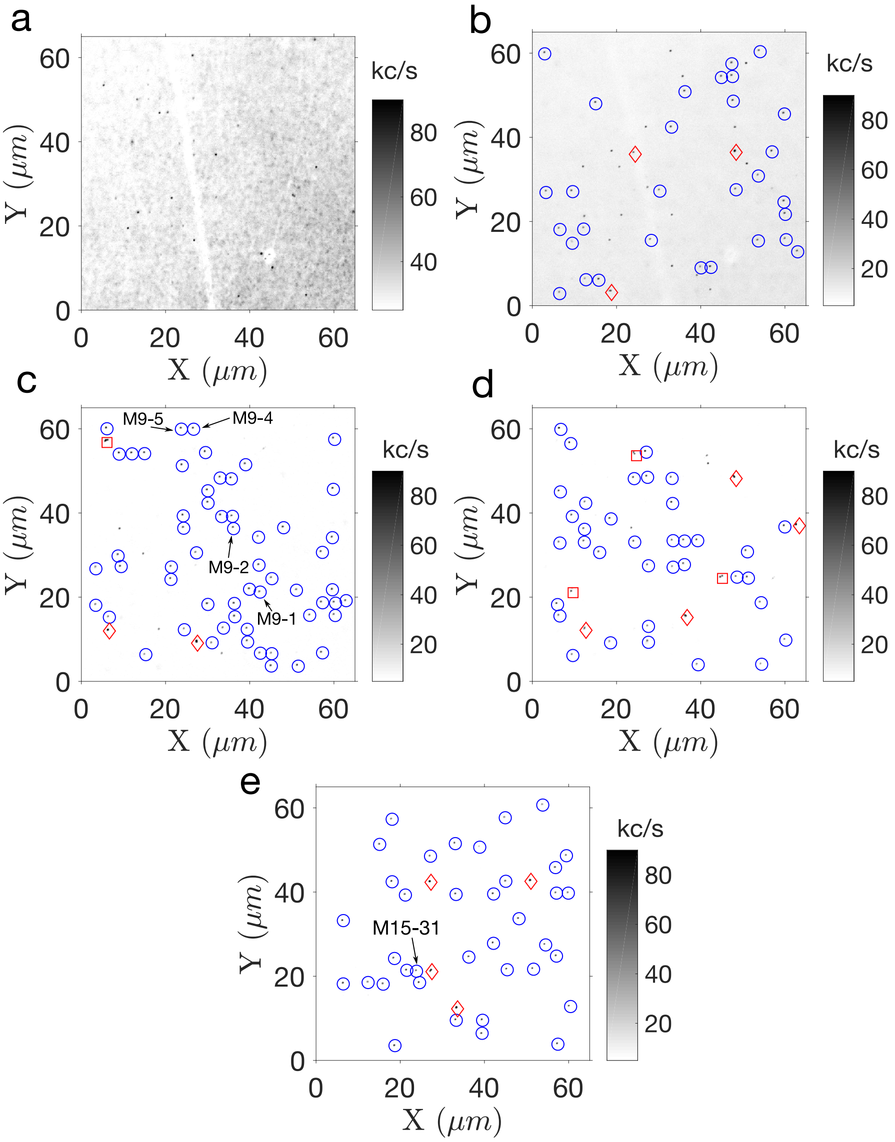

Figure 4.11: Labelled layers of array M (17.5 nJ, 3 µm with single NV^- circled and double NV^- denoted by diamonds (determined by HBT) or squares (optically resolvable). Single NV^- sites where T_2 was measured are labelled (M9-5 and M9-4 are the highlighted sites NV1 and NV2 from Figure 4.10). *a*-*e* are respectively at depths of 3, 6, 9, 12 and 15 µm below the surface.

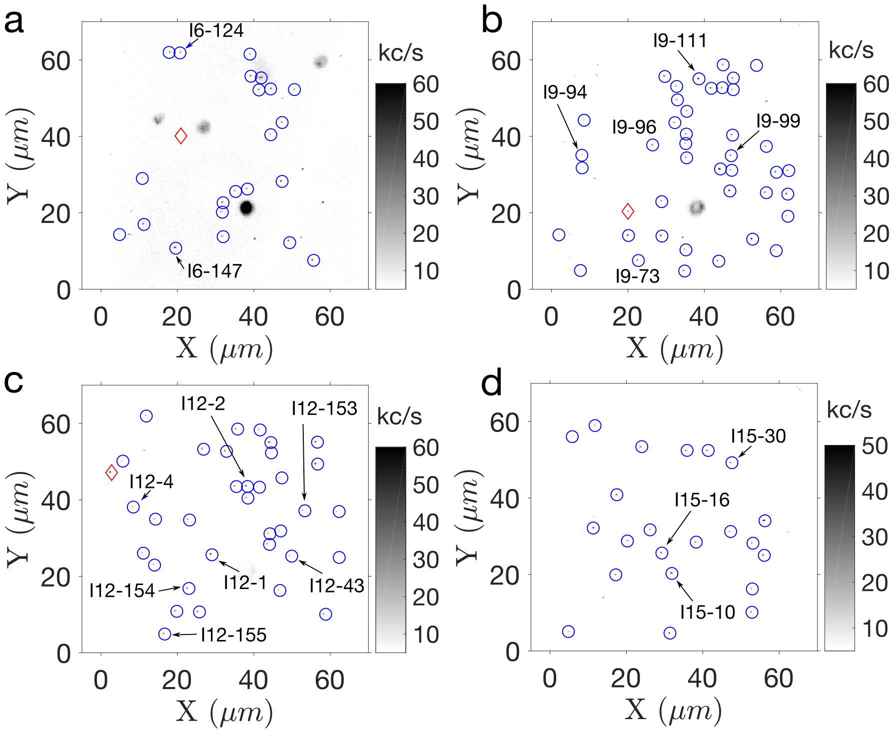

Figure 4.12: Labelled layers of array I (17 nJ, 3 µm pitch) with single NV$^-$ circled and double NV$^-$ denoted by diamonds (determined by HBT) or squares (optically resolvable). Single NV$^-$ sites where T$_2$ was measured are labelled. *a*-*d* are respectively at depths of 6, 9, 12 and 15 µm below the surface.

4.4.2 Yield of single NV$^-$

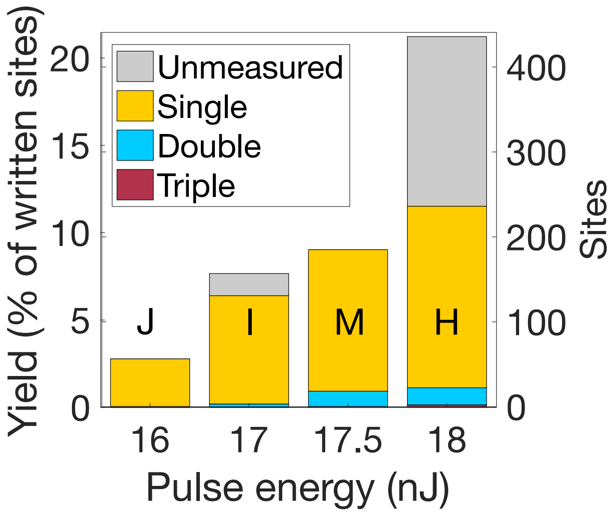

Figure 4.13: HBT statistics for all 3 µm pitch arrays which showed fluorescence, including incomplete measurement coverage of array H with approximately 20% yield of single NV$^-$, 2.5% double NV$^-$ and 0.3% triple NV$^-$, trading increased yield for a higher proportion of multiple NV$^-$ sites.

To check if the NV$^-$ were single centres, automated HBT experiments on over 600 sites were used to measure the photon arrival autocorrelation function $g^{(2)}(\tau)$ as shown in Figure 4.13. Sites were classified as a single emitter where $g^{(2)}(0) < 0.5$, a double for $0.5 \leq g^{(2)}(0) < 0.66$ and a triple for $0.66 \leq g^{(2)}(0) < 0.75$. For array M, 87% of the NV$^-$ are single centres, with 11% being doubles and 2% triples Figure 4.14. The sites with no NV$^-$ could be repeatedly re-written with another laser pulse and re-annealed until no sites are empty. The previous paper to report single NV$^-$ creation with laser writing[28] used higher pulse energies and reported a higher yield of single NV$^-$ but there were similarly more of the unwanted double and triple NV$^-$ which would lead to a lower yield of single NV$^-$ in a repeat-until-success strategy. Of the 2050 sites written in array M, 8% developed into a single NV$^-$, 0.6% produced a double NV$^-$ and $< 0.1\%$ produced a triple NV$^-$. This is consistent with Poissonian statistics (the chance of one NV$^-$ forming is 8%, two $0.08^2 = 0.6\%$ and three $0.08^3 \approx 0.05\%$) suggesting that NV$^-$ creation process may be limited by the availability of nitrogen rather than by variance in the vacancy production rate of the highly non-linear laser writing process.

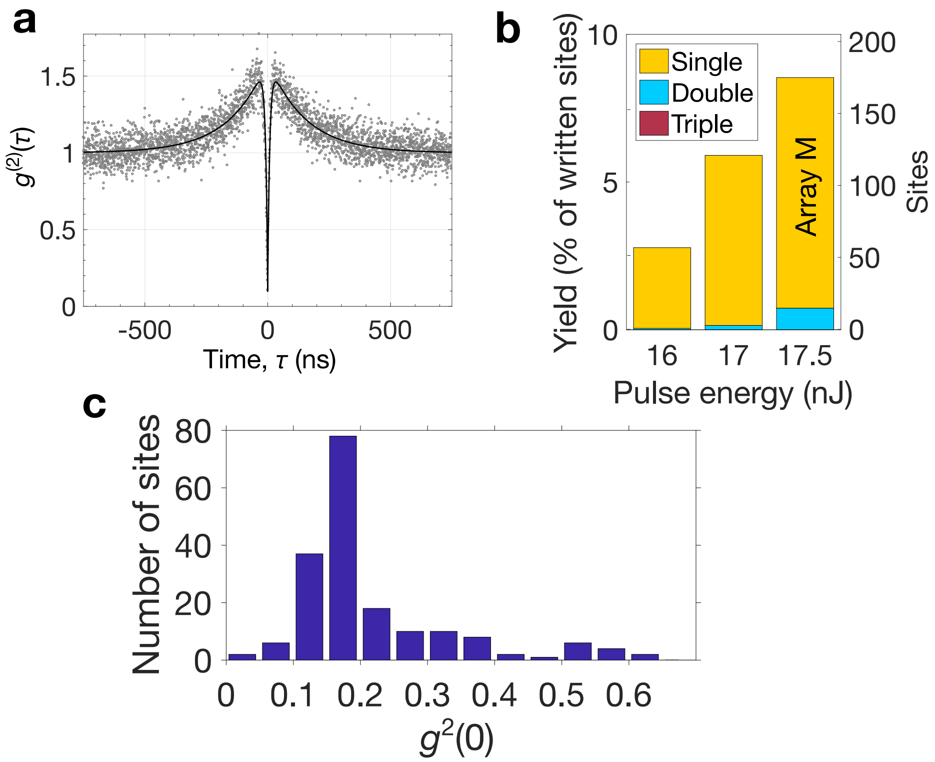

Figure 4.14: Fraction of single nitrogen vacancy centres compared to doubles and triples. a) HBT measurement of the photon arrival time for NV1. b) HBT measurements reveal the fraction of single, double and triple NV$^-$ produced in three of the 3 µm pitch arrays with different laser-write pulse energies. c) The frequency of the measured $g^{(2)}(0)$ for array M with no background subtraction.

4.4.3 Photoluminescence spectroscopy

Before and after the annealing process, photo-luminescence spectroscopy (PL) spectra under excitation with a 532 nm laser were measured using an Andor Shamrock spectrograph with an iDus series silicon charge-coupled device (CCD) through a multimode fibre.

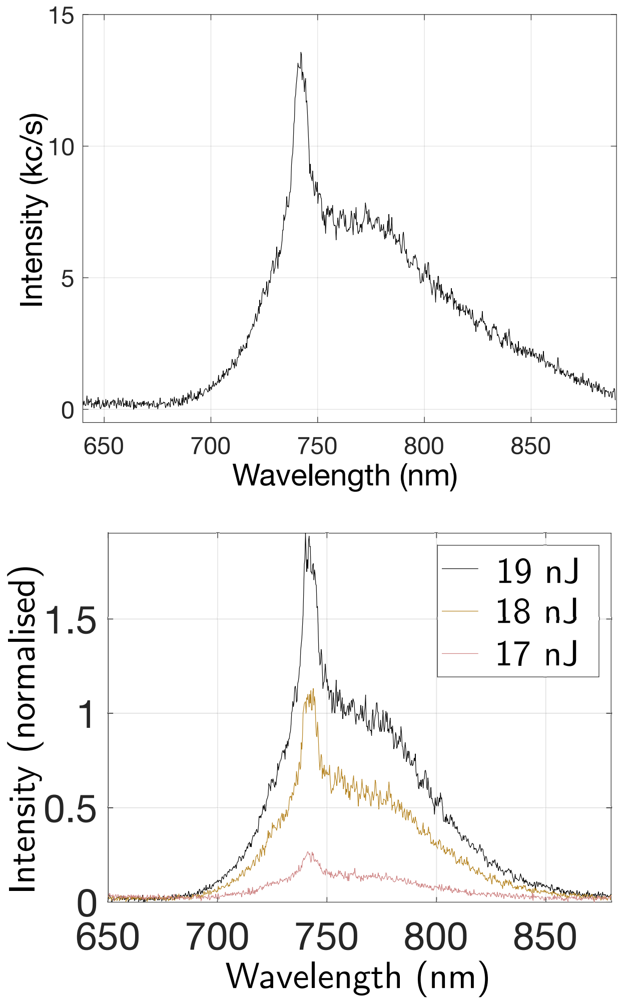

Figure 4.15: *(top panel)* PL spectrum of a single site in array A (19 nJ) before the sample was annealed at 1000 °C. *(bottom top)* PL spectra of three sites written with different pulse energies before annealing

Before the sample was annealed, PL spectra were collected such as that shown in Figure 4.15, clearly showing the characteristic GR1 emission spectrum associated with neutral vacancies in diamond[28, 42]. No sites were visible in array D (16 nJ) by confocal microscopy with a high NA oil objective before annealing.

Following the anneal, PL spectra were collected from sites including M9-4 (NV2 in Figure 4.21) which clearly show the characteristic spectrum of NV^- as in Figure 4.16. The background emission from a nearby region of diamond was collected for an equal duration and subtracted to eliminate artefacts of spectrometer response, second order Raman emission and fluorescence from the immersion oil.

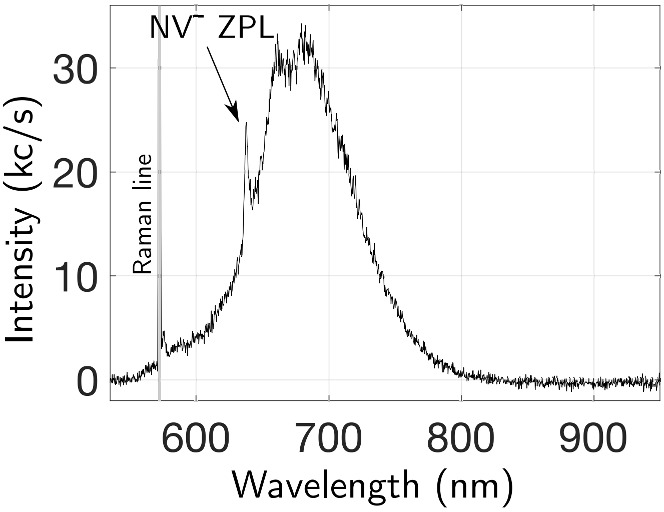

Figure 4.16: Photoluminescence emission spectrum from site M9-4 (NV2) shows the characteristic emission of NV^- with a ZPL at 637.7 nm.

4.4.4 Nitrogen vacancy colour centre yield

A narrow range of pulse energies were used to create three-dimensional arrays which each had a pitch of 2, 3 and 5 µm in the x, y and z directions. The proportion of sites which developed NV^- are shown in Figure 4.17. Whilst the yield of NV$^-$ in the 2 µm pitch arrays was high with a high proportion of single NV$^-$, the close packing of sites in depth made it more difficult to image individual sites in the z direction. The 3 µm pitch array developed a good yield of well-spaced NV$^-$ which could be characterised reliably. Despite a higher pulse energy, the 5 µm pitch array developed a lower yield of NV$^-$. This suggests that a smaller pitch leads to more damage which is reasonable given that the sites are written on top of each other in the z direction.

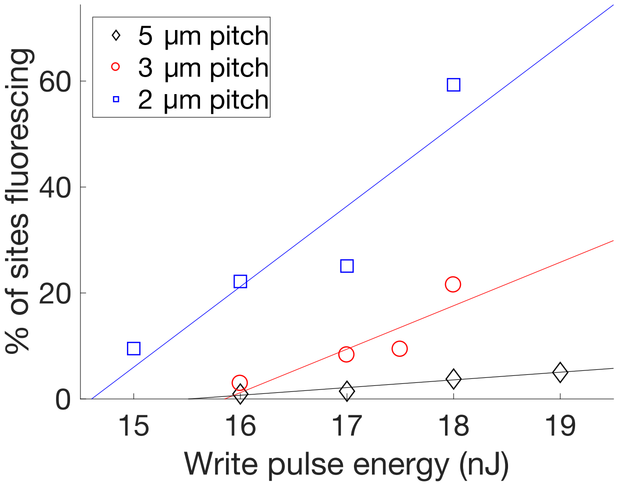

Figure 4.17: Proportion of sites fluorescing after the annealing process.

4.4.5 Position accuracy of NV$^-$ fabrication

The precision of the position for 167 single NV$^-$ in array M was analysed by three-dimensional fitting of the point spread function Figure 4.18. This reveals that the NV$^-$ are in the desired locations to within ±220 nm in the transverse (XY) plane and ±250 nm in the vertical (Z) direction. The high precision in the Z direction is due to the non-linearity of the writing. The precision is probably limited by the concentration of nitrogen in this material which is in the range from 1 ppb to 5 ppb corresponding to an average spacing between nitrogen atoms of 180 nm to 100 nm. This implies that the vacancies generally bond to one of their nearest nitrogen dopants. This suggests that positioning accuracy could be improved in diamond grown with 1 ppm of nitrogen without significantly reducing the coherence lifetime[52].

Automated measurements of position were made relative to a reference single NV^- using confocal microscopy using a PI Mars P-563 closed loop nano-positioning stage. By fitting oversampled confocal scans of single NV^- with Gaussian profiles to approximate the PSF of the optical system, the positions of single centres relative to a repeatedly measured reference point were inferred to better than the diffraction limit in three dimensions. Repeated measurements show that this technique has an accuracy of around 20 nm over a 20 minute period and remains self-consistent in the presence of slow drifts in sample position as shown in panel *(d)* of Figure 4.18.

The site positions were fitted to a grid of the design pitch and the position displacements reported are the measured displacements from the fitted orientation after rotation to compensate for sample tilt and skew as shown in Figure 4.18.

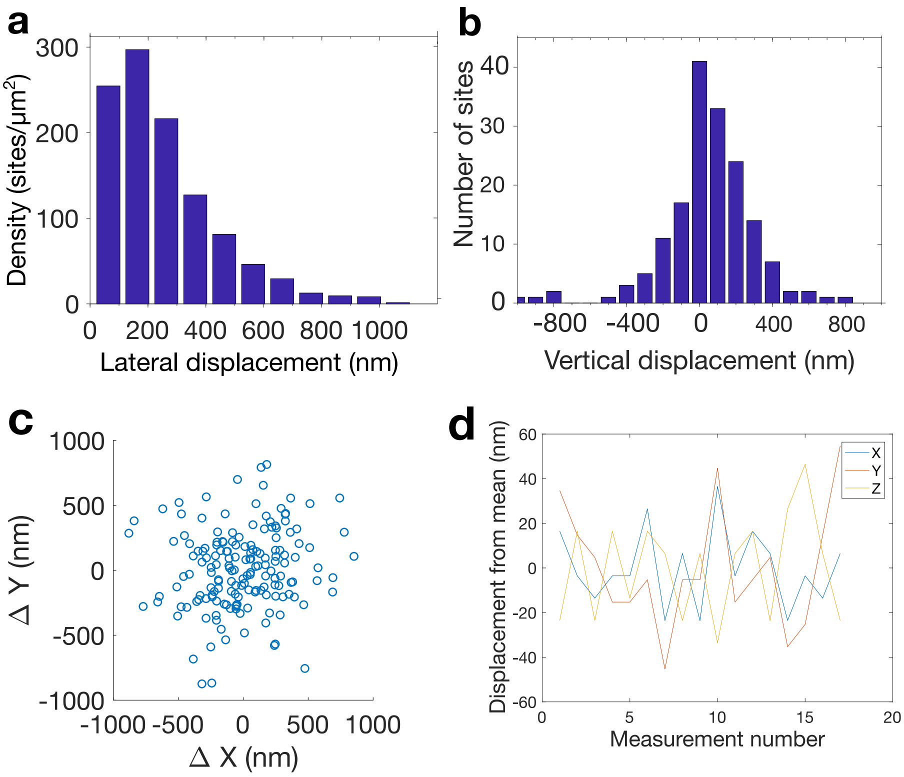

Figure 4.18: Positioning precision of single nitrogen vacancy centres in array M. *(a,c)* position displacement in the XY plane of the array. *(b)* position displacement in the vertical Z direction. Standard deviations are 220 nm and 250 nm respectively which is consistent with the mean separation of nitrogen in EL grade CVD diamond. *(d)* shows change in the relative displacement between two points over time as measured by fitting the PSF and using a third point as a reference between each measurement to estimate the error in the position measurement method. No systematic drift is apparent.

4.4.6 Birefringence and the influence of strain

Array I has the region of highest birefringence, in the upper right quadrant of these images, however throughout the arrays birefringence was low. Comparable to low birefringence optical diamond and is relatively low for electronic grade diamond. The laser writing sites which do and do not develop fluorescing NV^- do not correlate with the birefringence indicated by brightness through crossed polarisers Figure 4.19.

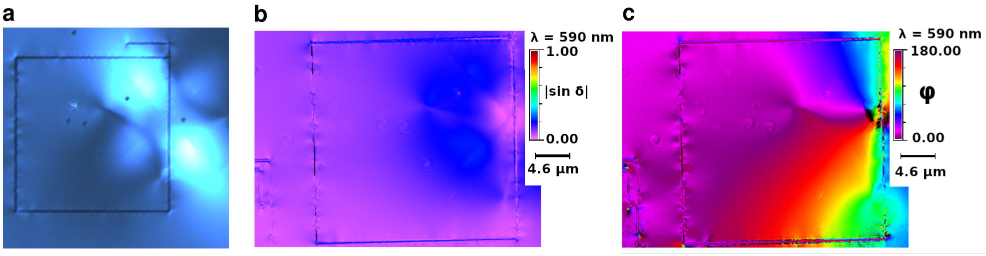

Figure 4.19: Array I had the most variation in strain as determined by crossed-polariser microscopy (a) and Metripol measurements of absolute birefringence (b,c). These images have been rotated to match orientation with the confocal microscopy.

As the sites were written in well defined locations, sites could be classified as "bright" where NV^- were present and "dark" where they were absent. No correlation was found between the birefringence at a site and the development of NV^- Figure 4.20, suggesting that local variations in strain do not significantly influence the create of N-V complexes.

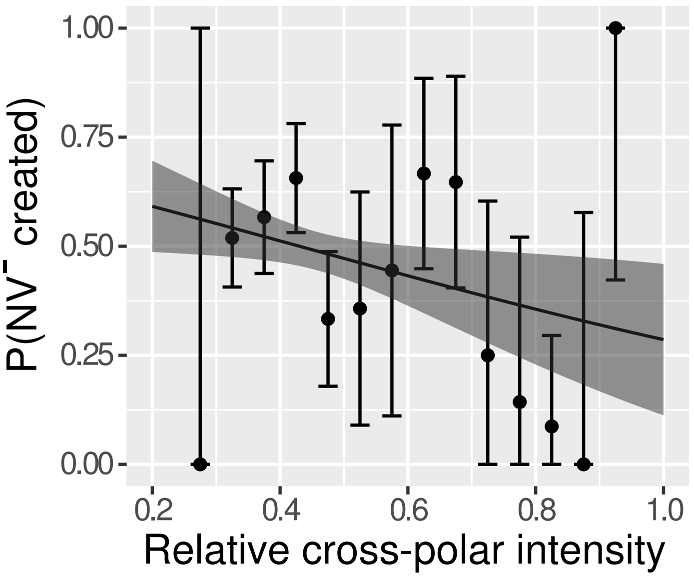

Figure 4.20: The influence of strain on NV$^-$ formation could be inferred from the probability of forming a single or double NV$^-$ in any layer of array I, binned by the relative crossed-polarizer intensity (normalized over the diamond). As the Metripol measurements Figure 4.19 show only one order of phase shift, the brightness in the cross-polar image indicates higher birefringence, and hence strain (aggregated through the full thickness of the diamond). The fit to a binary logistic regression model is shown with a 1 standard deviation confidence interval. No significant correlation is found ($p = 0.3$), suggesting NV$^-$ yield in this array is not strongly influenced by local strain. The probability of forming NV$^-$ is taken as the fraction of sites in each cross-polar brightness binning group which develop a single or double NV$^-$ (optically resolvable or not).

4.4.7 Spin-echo coherence time measurements

Spin-echo coherence times (T_2) of sites in arrays I & M were measured using the procedure described in Section 4.3.4. Two selected adjacent sites were labelled NV1 & NV2 located in the 9 µm layer of array M Figure 4.21. Although slightly longer T_2 times were measured at a few other sites, these two sites are interesting as they are both adjacent (separated by 3 µm) and have aligned dipoles. (In future work, such sites would be ideal candidates for showing that multiple NV^- sites could be operated on in the same cryostat by taking advantage of the fabrication control to place NV^- where they will couple into a fibre-bundle.)

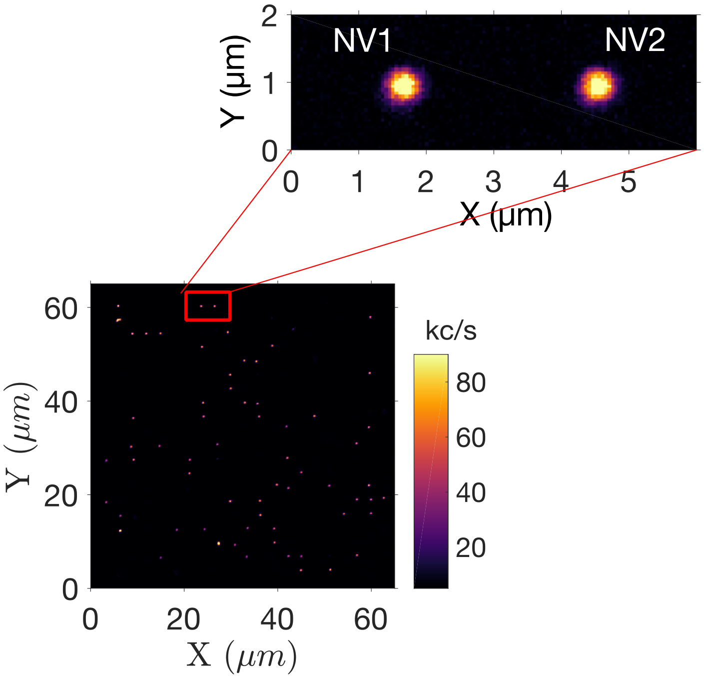

Figure 4.21: In the layer of array M 9 µm below the surface two adjacent, aligned NV^- with good spin-echo coherence properties are labelled NV1 and NV2. NV1 has $T_2 = (710 \pm 40)$ µs, while NV2 has $T_2 = (690 \pm 90)$ µs.

A ~30 mT magnetic field from a large, cylindrical permanent magnet was aligned along the axis of one of these NV^- sites. by the method described in Section 4.3.4. The echo-decay measurements for NV1 and NV2 are shown in Figure 4.22, fitted with a stretched exponential $Ae^{-\left(\frac{t}{T_2}\right)^n}$. As expected by theory if not limited by other relaxation mechanisms, $n \approx 2$ within error.

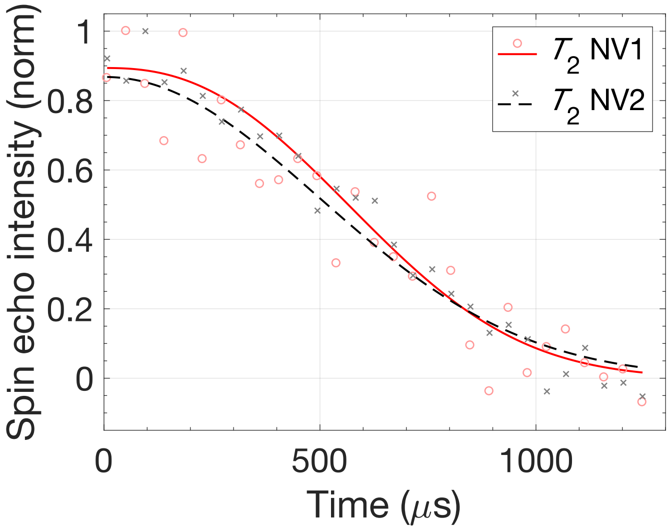

Figure 4.22: Nitrogen vacancy centre spin-echo coherence times for NV1 and NV2 Figure 4.21. Spin-echo decays measurements of the aligned, adjacent NV^- labelled NV1 and NV2 were fitted to $Ae^{-\left(\frac{t}{T_2}\right)^n}$. NV1 has $T_2 = (710 \pm 40)\,\mu s$ with $n = 2.4 \pm 0.4$, while NV2 has $T_2 = (690 \pm 90)\,\mu s$ with $n = 2.0 \pm 0.8$.

A complication in many spin-echo decay measurements is the emergence of "revivals" which modulate the echo decay envelope due to the influence of the ^{13}C spin bath. Where ^{13}C nuclei are not nearest neighbours of the NV^-, applying a large enough magnetic field along the NV^- axis is sufficient to conveniently suppress this effect[184]. Nevertheless, the time increment for echo-decay measurements was chosen to be a multiple of the ^{13}C Larmor period, predicted from the measured field strength. By sampling where the revival peaks occur - which is possible as long as there is a single, stable revival frequency - the envelope can be reconstructed accurately with fewer sampling points with a higher signal to noise ratio per point in a given measurement time.

In spin-echo decay measurements, sites with long T_2 coherence times take longer to measure as a series of measurements must include increasing delays (τ) up to around twice the T_2 of the spin being measured in order to reliably fit the baseline of the multiple exponential. Each spin-echo measurement takes 2τ for the echo to return. After the improvements detailed in Section 3.5.4, 3 h to 10 h of measurement time with ~ 13 measurement points was sufficient to unambiguously fit the stretched exponential $Ae^{-\left(\frac{t}{T_2}\right)^n}$ for most sites.

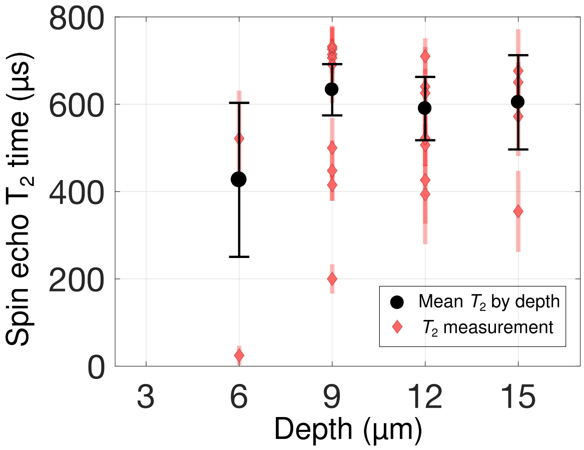

Figure 4.23: Spin echo coherence times measured for sites in arrays M (17.5 nJ) and I (17 nJ). Both arrays were written with a 3 µm pitch.

Figure 4.23 shows measurements of the spin coherence from 22 of the single NV^- in the 3 µm pitch arrays M and I. The longest room-temperature spin-echo coherence times without ^{12}C enrichment we have found in the literature are $T_2 = 687$ µs[92] and $T_2 = 650$ µs[68], which are slightly below (but within the error of) the five longest T_2 times measured in these arrays. The long times measured here demonstrate that the laser-writing technique does not introduce excess damage or impurities to the environment of the NV^-.

The calibration step to ensure we used the optimum write-pulse energy may be needed to achieve this[28].

Arrays M, I, J and H were focused upon and the single-centre statistics for these are shown in Figure 4.13. Confocal images of the layers in arrays M and I are shown in Figure 4.11 and Figure 4.12 respectively which show both the distribution of single and double centres and the location of the NV^- where the spin echo lifetime (T_2) was measured. There is no obvious clustering of the multiple NV^- sites or sites with long T_2 times. Some of the longest spin echo lifetimes measured are shown in Figure 4.25 along with a table of the fitted lifetimes Table 4.1 and a histogram of lifetimes Figure 4.24.

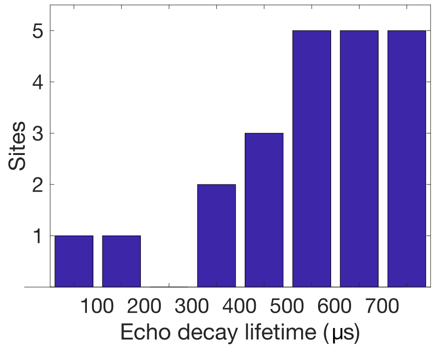

Figure 4.24: Histogram of the echo decay lifetimes, T_2.

Site	Coherence time (μs)	Exponent
I9-73	730 ± 40	2.1 ± 0.4
I9-94	730 ± 20	2.7 ± 0.3
I9-96	710 ± 60	2.1 ± 0.6
I12-1	710 ± 40	2.5 ± 0.5
M9-5 (NVC1)	706 ± 40	2.4 ± 0.4
M9-4 (NVC2)	690 ± 90	2.0 ± 0.8
I15-30	680 ± 100	2.4 ± 1.1
M15-31	650 ± 50	2.7 ± 0.7
I12-155	640 ± 40	2.2 ± 0.4
I12-2	630 ± 110	1.3 ± 0.4
I15-10	570 ± 90	1.3 ± 0.4
I12-43	520 ± 60	2.4 ± 1.0
I6-147	520 ± 110	1.6 ± 0.8
I12-154	510 ± 50	2.0 ± 0.5
I9-99	500 ± 70	2.4 ± 1.2
I9-111	448 ± 70	2.1 ± 0.9
I12-4	430 ± 150	1.3 ± 0.7
M9-2	420 ± 40	2.0 ± 0.5
I12-153	390 ± 70	2.4 ± 1.4
I15-16	360 ± 90	1.3 ± 0.6
M9-1	200 ± 30	1.3 ± 0.4
I6-124	25 ± 20	1.1 ± 1.2

Table 4.1: Coherence lifetimes (T_2) for the sites measured.

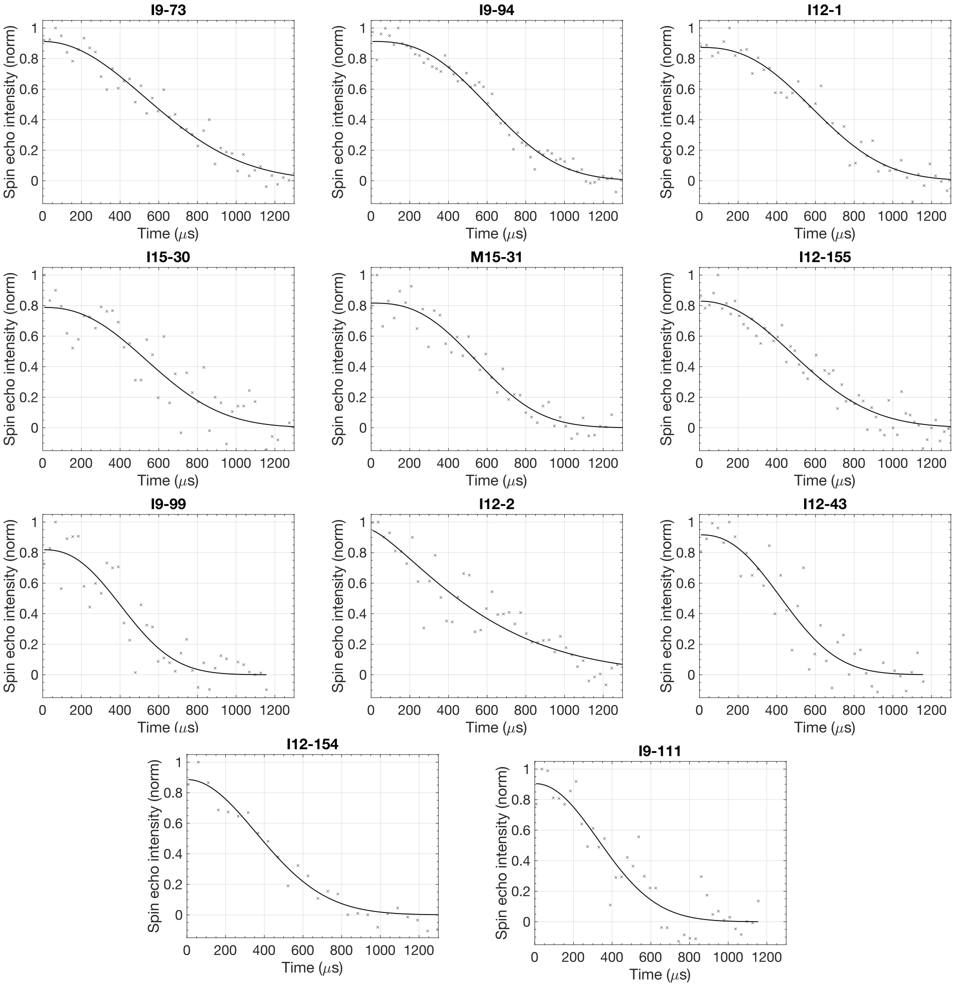

Figure 4.25: Examples of T_2 spin echo lifetime measurements from arrays M and I.

4.4.8 Dynamic decoupling and T_1 measurements

By applying a dynamic decoupling pulse sequence to cancel out the influence of the spin bath, the spin-echo can preserved for considerably longer. As shown in Figure 4.26, a T_2 of (2.4 ± 0.6) ms was measured for NV1 using the XY8-4 permuting dynamic decoupling sequence. This is comparable to the measured T_1.

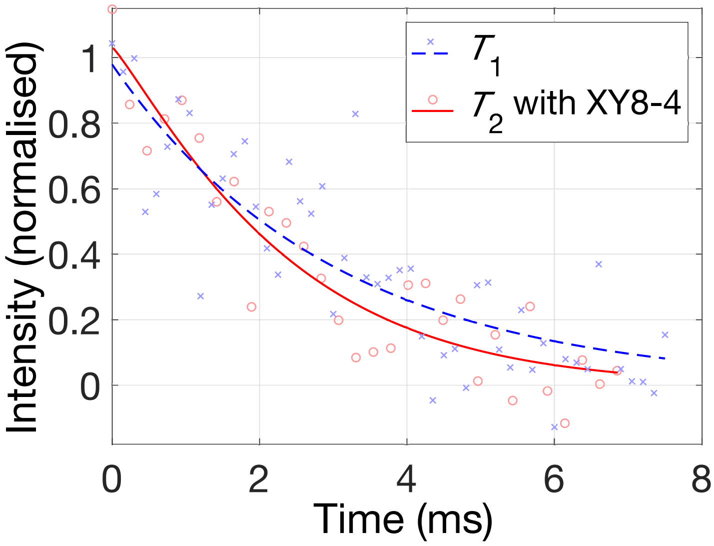

Figure 4.26: Using XY8-4 dynamic decoupling on site NV1 achieved $T_2 = (2.4 \pm 0.6)$ ms with $n = 1.1 \pm 0.4$ on NV1. For comparison, the longitudinal lifetime, T_1, of this site was (3.0 ± 0.7) ms.

Using 8 sets of XY8 units (XY8-8) was less effective despite allowing a shorter time for decoherence before a refocusing pulse is applied. This may have been due to accumulated refocusing errors from imperfect pulses.

Chapter 5

Summary & future work

5.1 Three-dimensional arrays of laser written NV$^-$

The large study of laser-written sites in electronic grade diamond presented in this work measured significantly more sites that have been created in previous work and at a range of depths. The results show that single NV$^-$ colour centres can be fabricated with calibrated femto-second laser pulses at depths of 6 nm to 30 nm is possible with a single centre yield of around 10 % after annealing for 3 h at 1000 °C. Many of the synthetic NV$^-$ were measured to have exceptionally long T$_2$ times - some in excess of 700 µs. The femto-second pulse laser writing technique for fabricating single NV$^-$ was shown to be effective in creating high quality, single NV$^-$ colour centres at depths between 6 µm and 30 µm - both deeper than ion implantation technqiues without overgrowth and considerably shallower than had been achieved in the previous laser writing work.

In the 3 µm pitch arrays, single NV$^-$ formed at up to 8 % of sites with 0.6 % of sites having two NV$^-$ and 0.1 % having three NV$^-$, suggesting that the probability distribution of NV$^-$ formation is Poissonian. No correlation was found between the limited local strain and the formation of NV$^-$, where strain was present. The more closely pitched the three dimensional arrays showed NV$^-$ formation at lower pulse energies, suggesting that vacancies are more readily induced where the lattice has already been disrupted a few microns away.

This was a significantly larger survey of the single NV$^-$ than has been attempted previous and showed how sensitive the process is to small changes in pulse energy. No evidence of correlation between the formation of NV$^-$ and localised strain was found. The quantum coherence time of a number of these centres was measured and the T$_2$ time at the majority of the generated sites was $>500\,\mu$s an order of magnitude longer than that measured in the previous work on laser written NV^-. Using XY8-4 dynamic decoupled pulses sequences, the coherence lifetime was extended to more than 2 ms.

Considerable automation capabilities were developed in order to efficiently measure a large number of sites consistently. Notably these included a procedure to robustly visit a large number of previously located sites at various depths, accurately record their position relative to a guide point, acquire an HBT measurement, decide if the site is single, acquire an ODMR spectrum, fit the ODMR spectrum to determine the site orientation, determine the π pulse duration from Rabi oscillations, perform a Ramsey pulsed measurement and perform a long-duration Hahn echo experiment over a number of days with minimal human supervision. Also developed were routines to determine the relative position of point light sources to less than the diffraction limit by fitting the point spread function, allowing the location of single femto-second laser written NV^- to be determined with 20 nm precision[30, 36]. Referencing of position to a “guide” site by Gaussian fitting was also used very effectively to register slices of three-dimensional image stacks to allow whole three-dimensional NV^- arrays to be imaged with negligble offset between layers.

The prevalance of long coherence time laser written NV^- in this work has shown that laser-writing can produce exceptionally good quality single NV^- centres however the limited yield is an outstanding problem.

5.1.1 Comparison to “repeat until success”

Parallel work on laser written NV^- using a “repeat until success” strategy has not matched the coherence times achieved in this work. The annealing step here is three hours in a tube furnace. In contrast, the initial repeat until success work has used in-situ laser annealing. The repeat until success work also uses additional, conditional write pulses to break more bonds and generate more vacancies if no NV^- has been generated at a site. However as damage is induced, the local properties of the diamond are altered. Given the sensitivity of the highly non-linear writing process to small variation in pulse energy or absorption it is perhaps unsurprising that further work is needed to obtain both 100% yield and $T_2 > 600\,\mu s$.

5.2 Cryogenic pulsed ODMR confocal microscopy of nanodiamonds

Whilst the original goal of the low-temperature confocal microscopy project was not fully achieved, many technical problems were solved and the system demonstrated fibre-coupled confocal fluorescence microscopy and confocal reflection microscopy in the confines of a cryogenic probe. The resolution of this system approached the diffraction limit.

A fast, high-exclusion (>50 dB) optical switch was developed using a retro-reflected double pass through an AOM crystal along with a home-built RF driver. As well as enabling measurement of more than an order of magnitude longer quantum coherence lifetimes, the prototype AOM driver added instantaneous power control and saturation measurements. This driver was replicated for use in other experiments and has been instrumental in data collection for other ongoing work[36].

A novel, compact, vector electromagnet was developed which allows a field of a few milliteslas to be applied in any orientation to nanodiamonds on a surface in the limited space available within the cryogenic probe. Using this electromagnet ODMR measurements demonstrated both an ODMR capability and vector control of a magnetic field with a magnitude of 6 mT.

Software was developed to control the Attocube piezo positioners via the Attocube ANC300 console with a user interface to control the stick-slip positioners and to co-opt the vertical positioner as an adhoc, limited range vertical scanning stage. This scanning capability can be used to implement automated focus optimisation, although this work has not been completed. The algorithm for autofocus is to fit a curve to the z-scan to attempt to detect and optimise a peak. In the absence of a peak, the tracking will follow the gradient - directing piezoelectric pulses to move a short distance in the approriate direction to keep the target in range. This procedure is expected to be capable of iteratively tracking shifts the position of the target during pODMR measurements.

5.3 Future work

5.3.1 Sub-surface graphitic electrodes around NV^-

In addition to the three-dimensional arrays of NV^-, several forms of electrodes with only a few microns of separation (one pair, two pairs and two pairs with a wire below to apply a vertical potential) around NV^- sites were created. Each design was replicated many times to ensure at least some would have an NV^-.

The intention of this work was to investigate the feasibility of Stark tuning with an electric potential[37], control of charge state switching and electroluminescence of NV_0 [146, 185]. The small electrode separation allows electric field strengths of hundreds of $\mathrm{kV\,m^{-1}}$ to be applied with only a few volts of potential. Longer term, arrays of qubits in diamond may well require supporting electrical and photonic structures around individual NV^- to ap-

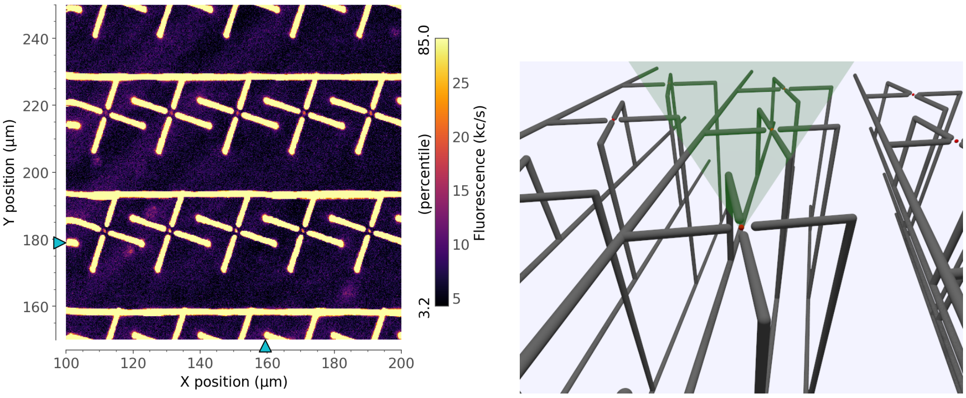

Figure 5.1: Confocal fluorescence microscopy image of a small area of laser written two-dimensional graphitic electrodes with single pulse laser written vacancy site and an illustration of electrodes.

ply compensating fields, address sites, channel light or control charge state with low capacitance. The laser writing process in diamond has previously demonstrated creation of optical wave guides [116, 141, 180] and conductive electrodes [29, 35, 115]. Other techniques for making sub-surface electrodes include ion beams [146, 185], boron doping [186, 187] however the laser-written wires have a smaller cross-section [35] and may cause little damage to the diamond lattice a few microns away - although an attempt by Laiyi Weng to measure single NV^- between electrodes with PLE was unsuccessful and no T_2 measurement has been made of these sites.

Several groups are working on constructing such integrations of wave guides or wires and synthetically created NV^- with laser writing [140, 188] but the some of the properties described in this work are signficant improvements. Work is still continuing on achieving unity yield [36], potentially with control of orientation. Integration with electrodes and microwave antenna on the surface has been achieved previously[130, 142] however there are advantages in knowing where the sites will be generated to scale these structures to control arrays of many NV^-.

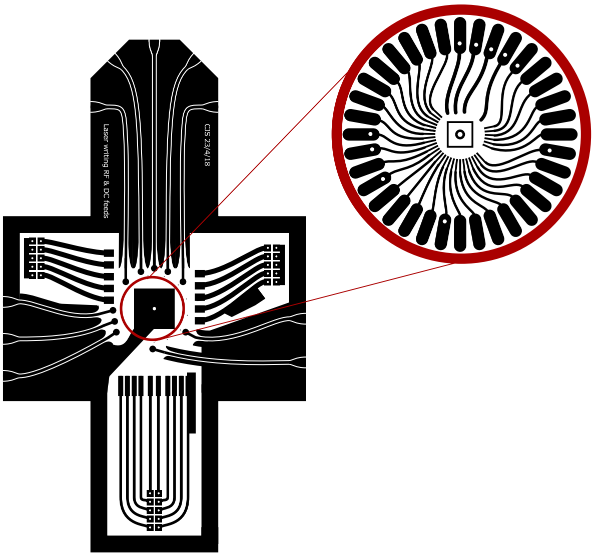

Figure 5.2: Breakout board for electrical connection of electrodes with miniature daughterboard for wire bonding to the ∼30 µm electrode contacts on the diamond.

Additionally to the electrode contacts, the lithographic metallisation also include surface microwave control lines aligned to the NV^- arrays, placed closer to the location of NV^- than would be possible with a separate wire positioned manually, decreasing the π-pulse length required.

Work was well advanced on electrically contacting the electrodes Figure 5.2 (with one, two Figure 5.1 and three pairs of probes at varying separations) in order to apply potentials in-situ on the confocal microscope to colour centres between such probes Figure 5.3, collaborating with colleagues to develop a process for high resolution lithographic metal deposition on a 2 mm × 2 mm diamond however this experiment unfortunately had to be abandoned on this sample, although it is hoped that this work will be continued by colleagues.

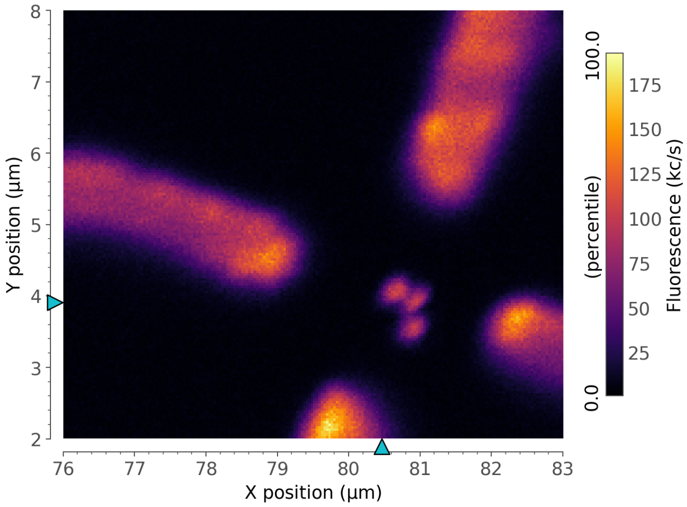

Figure 5.3: Tantalisingly, between some electrodes several optically resolvable single NV$^-$ formed - in this case three.

5.3.2 Cryogenic microscope

With a little further work this instrument will be capable of long duration pulsed ODMR at cryogenic temperatures. Completion of the auto-focusing implementation is required as well as some work on the software controlling the magnet. New, commercially wound coils for the electromagnet have been ordered to replace hand wound coils with fractured wires. Improvements to the sample holder on the top plate would make changes of sample easier and would ideally hold the sample in position at cryogenic temperatures more securely. The most difficult hardware challenges have been overcome and the majority of the remaining work is in integration and development of sensing pulse sequences.

With additional optics at the top of the probe, the system can also be extended to support PLE and to be used on other colour centres in diamond. As well as sensing individual dopant atoms, noise spectroscopy of semiconductor device structures with nanodiamonds would have practical applications. Finally this platform would be ideal for studying entanglement of NV$^-$ spins with adjacent ^{13}C nuclei or entanglement of laser written NV$^-$ sites.

5.3.3 Laser written NV$^-$

Work on laser-written single NV$^-$ is ongoing in several areas. Measurements of synthetic NV$^-$ in isotopically purified ^{12}C diamond may well show significantly longer coherence lifetimes. Work is underway to integrate single NV$^-$ with solid immersion lenses and on further attempts to combine them with laser-written electrodes. Parallel work has been conducted on different "repeat until success" strategies and further work is being planned to determine the effect of repeated laser writing and annealing. Work is also continuing within the UK Quantum Computing and Simulation (QCS) Hub to laser-write high quality NV$^-$ in thin membranes for integration into Purcell enhancement cavities. By enhancing the ZPL emission in this way, considerably higher entanglement rates are anticipated which would make laser-written NV$^-$ arrays a compelling technology for creating scalable, optically accessible ensembles of qubits.

References

[1] P. the Elder, “Historia Naturalis”, Vol. XXXVII, H.T. Riley translation, Bohn’s Classical Library (H. G. Bohn, 1855) Chap. 15.

[2] A. Gruber, A. Dräbenstedt, C. Tietz, L. Fleury, J. Wrachtrup, and C. Von Borczyskowski, “Scanning confocal optical microscopy and magnetic resonance on single defect centers”, Science **276**, 2012–2014 (1997).

[3] A. Marshall Stoneham, A. H. Harker, and G. W. Morley, “Could one make a diamond-based quantum computer?”, J. Phys. Condens. Matter **21**, 364222 (2009).

[4] M. W. Doherty, C. A. Meriles, A. Alkauskas, H. Fedder, M. J. Sellars, and N. B. Manson, “Towards a room-temperature spin quantum bus in diamond via electron photoionization, transport, and capture”, Phys. Rev. X **6**, 041035 (2016).

[5] N. Y. Yao, L. Jiang, A. V. Gorshkov, P. C. Maurer, G. Giedke, J. I. Cirac, and M. D. Lukin, “Scalable architecture for a room temperature solid-state quantum information processor”, Nat. Commun. **3**, 800 (2012).

[6] J. O’Gorman, N. H. Nickerson, P. Ross, J. J. L. Morton, and S. C. Benjamin, “A silicon-based surface code quantum computer”, Quantum Inf. **2**, 15019 (2016).

[7] J. O'Gorman and E. T. Campbell, "Quantum computation with realistic magic-state factories", Phys. Rev. A **95**, 032338 (2017).

[8] C. Bonato, M. S. Blok, H. T. Dinani, D. W. Berry, M. L. Markham, D. J. Twitchen, and R. Hanson, "Optimized quantum sensing with a single electron spin using real-time adaptive measurements", Nat. Nanotechnol. **11**, 247–252 (2016).

[9] S. R. Schofield, N. J. Curson, M. Y. Simmons, F. J. Rueß, T. Hallam, L. Oberbeck, and R. G. Clark, "Atomically precise placement of single dopants in si", Phys. Rev. Lett. **91**, 136104 (2003).

[10] T. Gaebel, M. Domhan, I. Popa, C. Wittmann, P. Neumann, F. Jelezko, J. R. Rabeau, N. Stavrias, A. D. Greentree, S. Prawer, J. Meijer, J. Twamley, P. R. Hemmer, and J. Wrachtrup, "Room-temperature coherent coupling of single spins in diamond", Nat. Phys. **2**, 408–413 (2006).

[11] P. C. Humphreys, N. Kalb, J. P. J. Morits, R. N. Schouten, R. F. L. Vermeulen, D. J. Twitchen, M. L. Markham, and R. Hanson, "Deterministic delivery of remote entanglement on a quantum network", Nature **558**, 268–273 (2018).

[12] X. Rong, J. Geng, F. Shi, Y. Liu, K. Xu, W. Ma, F. Kong, Z. Jiang, Y. Wu, and J. Du, "Experimental fault-tolerant universal quantum gates with solid-state spins under ambient conditions", Nat. Commun. **6**, 8748 (2015).

[13] A. Reiserer, N. Kalb, M. S. Blok, K. J. M. van Bemmelen, T. H. Taminiau, R. Hanson, D. J. Twitchen, and M. L. Markham, "Robust quantum-network memory using decoherence-protected subspaces of nuclear spins", Phys. Rev. X **6**, 021040 (2016).

[14] M. H. Abobeih, J. Cramer, M. A. Bakker, N. Kalb, D. J. Twitchen, M. L. Markham, and T. H. Taminiau, “One-second coherence for a single electron spin coupled to a multi-qubit nuclear-spin environment”, Nat. Commun. **9**, 2552 (2018).

[15] C. E. Bradley, J. Randall, M. H. Abobeih, R. C. Berrevoets, M. J. Degen, M. A. Bakker, M. L. Markham, D. J. Twitchen, and T. H. Taminiau, “A Ten-Qubit Solid-State Spin Register with Quantum Memory up to One Minute”, Phys. Rev. X **9**, 031045 (2019).

[16] G. W. Morley, P. Lueders, M. Hamed Mohammady, S. J. Balian, G. Aeppli, C. W. M. Kay, W. M. Witzel, G. Jeschke, and T. S. Monteiro, “Quantum control of hybrid nuclear-electronic qubits.”, Nat. Mater. **12**, 103 (2013).

[17] J. Tisler, G. Balasubramanian, B. Naydenov, R. Kolesov, B. Grotz, R. Reuter, J.-P. Boudou, P. A. Curmi, M. Sennour, A. Thorel, M. Börsch, K. Aulenbacher, R. Erdmann, P. R. Hemmer, F. Jelezko, and J. Wrachtrup, “Fluorescence and spin properties of defects in single digit nanodiamonds”, ACS Nano **3**, 1959–1965 (2009).

[18] B. R. Smith, D. Gruber, and T. Plakhotnik, “The effects of surface oxidation on luminescence of nano diamonds”, Diam. Relat. Mater. **19**, 314–318 (2010).

[19] P. G. Baranov, A. A. Soltamova, D. O. Tolmachev, N. G. Romanov, R. A. Babunts, F. M. Shakhov, S. V. Kidalov, A. Y. Vul’, G. V. Mamin, S. B. Orlinskii, and N. I. Silkin, “Enormously high concentrations of fluorescent nitrogen-vacancy centers fabricated by sintering of detonation nanodiamonds”, Small **7**, 1533–1537 (2011).

[20] J. P. Tetienne, T. Hingant, L. Rondin, A. Cavaillès, L. Mayer, G. Dantelle, T. Gacoin, J. Wrachtrup, J.-F. Roch, and V. Jacques, "Spin relaxometry of single nitrogen-vacancy defects in diamond nanocrystals for magnetic noise sensing", Phys. Rev. B **87**, 235436 (2013).

[21] R. Tsukahara, M. Fujiwara, Y. Sera, Y. Nishimura, Y. Sugai, C. Jentgens, Y. Teki, H. Hashimoto, and S. Shikata, "Removing Non-Size-Dependent Electron Spin Decoherence of Nanodiamond Quantum Sensors by Aerobic Oxidation", ACS Appl. Nano Mater. **2**, 3701–3710 (2019).

[22] M. Geiselmann, M. L. Juan, J. Renger, J. M. Say, L. J. Brown, F. Javier García De Abajo, F. Koppens, and R. Quidant, "Three-dimensional optical manipulation of a single electron spin", Nat. Nanotechnol. **8**, 175–179 (2013).

[23] P. Andrich, B. J. Alemán, J. C. Lee, K. Ohno, C. F. De Las Casas, F. J. Heremans, E. L. Hu, and D. D. Awschalom, "Engineered micro- and nanoscale diamonds as mobile probes for high-resolution sensing in fluid", Nano Lett. **14**, 4959–4964 (2014).

[24] C. Bradac, M. T. Johnsson, M. van Breugel, B. Q. Baragiola, R. Martin, M. L. Juan, G. K. Brennen, and T. Volz, "Room-temperature spontaneous superradiance from single diamond nanocrystals", Nat. Commun. **8**, 1205 (2017).

[25] L. Basso, F. Gorrini, M. Cazzanelli, N. Bazzanella, A. Bifone, and A. Miotello, "An all-optical single-step process for production of nanometric-sized fluorescent diamonds", Nanoscale **10**, 5738–5744 (2018).

[26] J. Stursa, J. Havlik, V. Petrakova, M. Gulka, J. Ralis, V. Zach, Z. Pulec, V. Stepan, S. A. Zargaleh, M. Ledvina, M. Nesladek, F. Treussart, and

P. Cigler, “Mass production of fluorescent nanodiamonds with a narrow emission intensity distribution”, Carbon **96**, 812–818 (2016).

[27] P. Reineck, L. F. Trindade, J. Havlik, J. Stursa, A. Heffernan, A. Elbourne, A. Orth, M. Capelli, P. Cigler, D. A. Simpson, and B. C. Gibson, “Not All Fluorescent Nanodiamonds Are Created Equal: A Comparative Study”, Particle **36**, 1900009 (2019).

[28] Y.-C. Chen, P. S. Salter, S. Knauer, L. Weng, A. C. Frangeskou, C. J. Stephen, S. N. Ishmael, P. R. Dolan, S. Johnson, B. L. Green, G. W. Morley, M. E. Newton, J. G. Rarity, M. J. Booth, and J. M. Smith, “Laser writing of coherent colour centres in diamond”, Nat. Photonics **11**, 77–80 (2016).

[29] B. Sun, P. S. Salter, and M. J. Booth, “High conductivity micro-wires in diamond following arbitrary paths”, Appl. Phys. Lett. **105**, 231105 (2014).

[30] C. J. Stephen, B. L. Green, Y. N. D. Lekhai, L. Weng, P. Hill, S. Johnson, A. C. Frangeskou, P. L. Diggle, Y. C. Chen, M. J. Strain, E. Gu, M. E. Newton, J. M. Smith, P. S. Salter, and G. W. Morley, “Deep Three-Dimensional Solid-State Qubit Arrays with Long-Lived Spin Coherence”, Phys. Rev. Appl. **12**, 064005 (2019).

[31] R. R. Gattass and E. Mazur, “Femtosecond laser micromachining in transparent materials”, Nat. Photonics **2**, 219–225 (2008).

[32] T. V. Kononenko, M. Meier, M. S. Komlenok, S. M. Pimenov, V. Romano, V. P. Pashinin, and V. I. Konov, “Microstructuring of diamond bulk by IR femtosecond laser pulses”, Appl. Phys. A Mater. Sci. Process. **90**, 645–651 (2008).

[33] R. D. Simmonds, P. S. Salter, A. Jesacher, and M. J. Booth, "Three dimensional laser microfabrication in diamond using a dual adaptive optics system", Opt. Express **19**, 24122 (2011).

[34] S. Lagomarsino, S. Sciortino, B. Obreshkov, T. Apostolova, C. Corsi, M. Bellini, E. Berdermann, and C. J. Schmidt, "Photoionization of monocrystalline CVD diamond irradiated with ultrashort intense laser pulse", Phys. Rev. B **93**, 085128 (2016).

[35] P. S. Salter, M. J. Booth, A. Courvoisier, D. A. J. Moran, and D. A. MacLaren, "High resolution structural characterisation of laser-induced defect clusters inside diamond", Appl. Phys. Lett. **111**, 081103 (2017).

[36] Y.-C. Chen, B. Griffiths, L. Weng, S. S. Nicley, S. N. Ishmael, Y. N. D. Lekhai, S. Johnson, C. J. Stephen, B. L. Green, G. W. Morley, M. E. Newton, M. J. Booth, P. S. Salter, and J. M. Smith, "Laser writing of individual nitrogen-vacancy defects in diamond with near-unity yield", Optica **6**, 662 (2019).

[37] E. van Oort and M. Glasbeek, "Electric-field-induced modulation of spin echoes of N-V centers in diamond", Chem. Phys. Lett. **168**, 529–532 (1990).

[38] S. Ferro, "Synthesis of diamond", J. Mater. Chem. **12**, 2843–2855 (2002).

[39] F. P. Bundy, "The P , T phase and reaction diagram for elemental carbon", J. Geophys. Res. **85**, 6930 (1980).

[40] H. H. Tracy, *Diamond synthesis*, US Patent 2,947,608, Aug. 1960.

[41] G. Davies, "Vibronic spectra in diamond", J. Phys. C Solid State Phys. **7**, 3797 (1974).

[42] A. Zaitsev, *Optical Properties of Diamond: A Data Handbook* (Springer, 2001).

[43] J. H. N. Loubser and J. A. van Wyk, "Electron spin resonance in the study of diamond", Reports Prog. Phys. **41**, 1201–1248 (1978).

[44] J. Walker, "Optical absorption and luminescence in diamond", Reports Prog. Phys. **42**, 1605–1659 (1979).

[45] D. J. Twitchen, D. C. Hunt, C. Wade, M. E. Newton, J. M. Baker, T. R. Anthony, and W. F. Banholzer, "The production and annealing stages of the self-interstitial (R2) defect in diamond", Phys. B Condens. Matter **273-274**, 644–646 (1999).

[46] M. W. Dale, "Colour centres on demand in diamond" (University of Warwick, 2015), `http://wrap.warwick.ac.uk/80044/1/WRAP_THESIS_Dale_2015.pdf`.

[47] D. J. Twitchen, M. E. Newton, J. M. Baker, T. R. Anthony, and W. F. Banholzer, "Electron-paramagnetic-resonance measurements on the divacancy defect center (R4/W6) in diamond", Phys. Rev. B **59**, 12900–12910 (1999).

[48] Y. Chu, N. P. de Leon, B. J. Shields, B. J. M. Hausmann, R. E. Evans, E. Togan, M. J. Burek, M. L. Markham, A. Stacey, A. S. Zibrov, A. Yacoby, D. J. Twitchen, M. Lončar, H. Park, P. Maletinsky, and M. D. Lukin, "Coherent optical transitions in implanted nitrogen vacancy centers", Nano Lett. **14**, 1982–1986 (2014).

[49] M. E. Newton, B. A. Campbell, D. J. Twitchen, J. M. Baker, and T. R. Anthony, "Recombination-enhanced diffusion of self-interstitial atoms and vacancy-interstitial recombination in diamond", Diam. Relat. Mater. **11**, 618–622 (2002).

[50] J. A. van Wyk and J. H. N. Loubser, “Optical spin-polarisation in a triplet state in irradiated and annealed type 1b diamonds”, Diam. Res. **9**, 11–14 (1977).

[51] M. W. Doherty, N. B. Manson, P. Delaney, F. Jelezko, J. Wrachtrup, and L. C. L. Hollenberg, “The nitrogen-vacancy colour centre in diamond”, Phys. Rep. **528**, 1–45 (2013).

[52] J. A. van Wyk, E. C. Reynhardt, G. L. High, and I. Kiflawi, “The dependences of ESR line widths and spin-spin relaxation times of single nitrogen defects on the concentration of nitrogen defects in diamond”, J. Phys. D. Appl. Phys. **30**, 1790–1793 (1997).

[53] E. van Oort, N. B. Manson, and M. Glasbeek, “Optically detected spin coherence of the diamond N-V centre in its triplet ground state”, J. Phys. C Solid State Phys. **21**, 4385–4391 (1988).

[54] E. van Oort, P. Stroomer, and M. Glasbeek, “Low-field optically detected magnetic resonance of a coupled triplet-doublet defect pair in diamond”, Phys. Rev. B **42**, 8605–8608 (1990).

[55] E. van Oort and M. Glasbeek, “Cross-relaxation dynamics of optically excited N-V centers in diamond”, Phys. Rev. B **40**, 6509–6517 (1989).

[56] A. Batalov, V. Jacques, F. Kaiser, P. Siyushev, P. Neumann, L. J. Rogers, R. L. McMurtrie, N. B. Manson, F. Jelezko, and J. Wrachtrup, “Low Temperature Studies of the Excited-State Structure of Negatively Charged Nitrogen-Vacancy Color Centers in Diamond”, Phys. Rev. Lett. **102**, 195506–195510 (2009).

[57] T. Plakhotnik, M. W. Doherty, J. H. Cole, R. Chapman, and N. B. Manson, “All-optical thermometry and thermal properties of the op-

tically detected spin resonances of the NV- center in nanodiamond", Nano Lett. **14**, 4989–4996 (2014).

[58] Z. Su, Z. Ren, Y. Bao, X. Lao, J. Zhang, J. Zhang, D. Zhu, Y. Lu, Y. Hao, and S. Xu, "Luminescence landscapes of nitrogen-vacancy centers in diamond: Quasi-localized vibrational resonances and selective coupling", J. Mater. Chem. C **7**, 8086–8091 (2019).

[59] H.-Q. Zhao, M. Fujiwara, and S. Takeuchi, "Effect of substrates on the temperature dependence of fluorescence spectra of nitrogen vacancy centers in diamond nanocrystals", Jpn. J. Appl. Phys. **51**, 090110 (2012).

[60] S. Johnson, P. R. Dolan, T. Grange, A. A. Trichet, G. Hornecker, Y. C. Chen, L. Weng, G. M. Hughes, A. A. Watt, A. Auffèves, and J. M. Smith, "Tunable cavity coupling of the zero phonon line of a nitrogen-vacancy defect in diamond", New J. Phys. **17**, 122003 (2015).

[61] D. Riedel, I. Söllner, B. J. Shields, S. Starosielec, P. Appel, E. Neu, P. Maletinsky, and R. J. Warburton, "Deterministic enhancement of coherent photon generation from a nitrogen-vacancy center in ultrapure diamond", Phys. Rev. X **7**, 031040 (2017).

[62] F. Jelezko, C. Tietz, A. Gruber, I. Popa, A. Nizovtsev, S. Kilin, and J. Wrachtrup, "Spectroscopy of single N-V centers in diamond", Single Mol. **2**, 255–260 (2001).

[63] F. Jelezko, I. Popa, A. Gruber, C. Tietz, J. Wrachtrup, A. Nizovtsev, and S. Kilin, "Single spin states in a defect center resolved by optical spectroscopy", Appl. Phys. Lett. **81**, 2160 (2002).

[64] F. Jelezko, T. Gaebel, I. Popa, A. Gruber, and J. Wrachtrup, "Observation of Coherent Oscillations in a Single Electron Spin", Phys. Rev. Lett. **92**, 076401 (2004).

[65] T. A. Kennedy, J. S. Colton, J. E. Butler, R. C. Linares, and P. J. Doering, "Long coherence times at 300 K for nitrogen-vacancy center spins in diamond grown by chemical vapor deposition", Appl. Phys. Lett. **83**, 4190–4192 (2003).

[66] F. Jelezko and J. Wrachtrup, "Single defect centres in diamond: A review", Phys. Status Solidi Appl. Mater. Sci. **203**, 3207–3225 (2006).

[67] J. R. Maze, J. M. Taylor, and M. D. Lukin, "Electron spin decoherence of single nitrogen-vacancy defects in diamond", Phys. Rev. B **78**, 094303 (2008).

[68] N. Mizuochi, P. Neumann, F. Rempp, J. Beck, V. Jacques, P. Siyushev, K. Nakamura, D. J. Twitchen, H. Watanabe, S. Yamasaki, F. Jelezko, and J. Wrachtrup, "Coherence of single spins coupled to a nuclear spin bath of varying density", Phys. Rev. B **80**, 5–8 (2009).

[69] L. Childress, M. V. Gurudev Dutt, J. M. Taylor, A. S. Zibrov, F. Jelezko, J. Wrachtrup, P. R. Hemmer, and M. D. Lukin, "Coherent dynamics of coupled electron and nuclear spin qubits in diamond", Science **314**, 281–285 (2006).

[70] P. Neumann, J. Beck, M. Steiner, F. Rempp, H. Fedder, P. R. Hemmer, J. Wrachtrup, and F. Jelezko, "Single-shot readout of a single nuclear spin", Science **329**, 542–544 (2010).

[71] P. Neumann, N. Mizuochi, F. Rempp, P. R. Hemmer, H. Watanabe, S. Yamasaki, V. Jacques, T. Gaebel, F. Jelezko, and J. Wrachtrup,

"Multipartite entanglement among single spins in diamond", Science **320**, 1326–1329 (2008).

[72] L. Jiang, J. S. Hodges, J. R. Maze, P. C. Maurer, J. M. Taylor, D. G. Cory, P. R. Hemmer, R. L. Walsworth, A. Yacoby, A. S. Zibrov, and M. D. Lukin, "Repetitive readout of a single electronic spin via quantum logic with nuclear spin ancillae", Science **326**, 267–272 (2009).

[73] P. C. Maurer, G. Kucsko, C. Latta, L. Jiang, N. Y. Yao, S. D. Bennett, F. Pastawski, D. Hunger, N. Chisholm, M. L. Markham, D. J. Twitchen, J. I. Cirac, and M. D. Lukin, "Room-temperature quantum bit memory exceeding one second", Science **336**, 1283–1286 (2012).

[74] P. Tamarat, N. B. Manson, J. P. Harrison, R. L. McMurtrie, A. Nizovtsev, C. Santori, R. G. Beausoleil, P. Neumann, T. Gaebel, F. Jelezko, P. R. Hemmer, and J. Wrachtrup, "Spin-flip and spin-conserving optical transitions of the nitrogen-vacancy centre in diamond", New J. Phys. **10**, 045004 (2008).

[75] P. Maletinsky, S. Hong, M. S. Grinolds, B. J. M. Hausmann, M. D. Lukin, R. L. Walsworth, M. Lončar, and A. Yacoby, "A robust scanning diamond sensor for nanoscale imaging with single nitrogen-vacancy centres.", Nat. Nanotechnol. **7**, 320–324 (2012).

[76] F. Dolde, I. Jakobi, B. Naydenov, N. Zhao, S. Pezzagna, C. Trautmann, J. Meijer, P. Neumann, F. Jelezko, and J. Wrachtrup, "Room-temperature entanglement between single defect spins in diamond", Nat. Phys. **9**, 139–143 (2013).

[77] F. A. Inam, M. D. Grogan, M. Rollings, T. Gaebel, J. M. Say, C. Bradac, T. A. Birks, W. J. Wadsworth, S. Castelletto, J. R. Rabeau, and M. J. Steel, "Emission and nonradiative decay of nanodiamond NV

centers in a low refractive index environment", ACS Nano **7**, 3833–3843 (2013).

[78] H.-Q. Zhao, M. Fujiwara, and S. Takeuchi, "Suppression of fluorescence phonon sideband from nitrogen vacancy centers in diamond nanocrystals by substrate effect", Opt. Express **20**, 15628 (2012).

[79] R. Tsukahara, M. Fujiwara, Y. Sera, Y. Nishimura, Y. Sugai, C. Jentgens, Y. Teki, H. Hashimoto, and S. Shikata, "Removing Non-Size-Dependent Electron Spin Decoherence of Nanodiamond Quantum Sensors by Aerobic Oxidation", ACS Appl. Nano Mater. **2**, 3701–3710 (2019).

[80] A. C. Frangeskou, A. T. Rahman, L. Gines, S. Mandal, O. A. Williams, P. F. Barker, and G. W. Morley, "Pure nanodiamonds for levitated optomechanics in vacuum", New J. Phys. **20**, 043016 (2018).

[81] A. C. Frangeskou, A. T. M. Rahman, L. Gines, S. Mandal, O. A. Williams, P. F. Barker, and G. W. Morley, "Pure nanodiamonds for levitated optomechanics in vacuum (Conference Presentation)", Optical trapping and optical micromanipulation xv, Vol. 10723, edited by K. Dholakia and G. C. Spalding (International Society for Optics and Photonics, 2018), `https://doi.org/10.1117/12.2324867`.

[82] H. S. Knowles, D. M. Kara, and M. Atatüre, "Demonstration of a Coherent Electronic Spin Cluster in Diamond", Phys. Rev. Lett. **117**, 100802 (2016).

[83] S. C. Benjamin, "Comment on "Efficient high-fidelity quantum computation using matter qubits and linear optics"", Phys. Rev. A **72**, 056302 (2005).

[84] J. Wrachtrup and F. Jelezko, "Processing quantum information in diamond", J. Phys. Condens. Matter **18**, S807–S824 (2006).

[85] S. C. Benjamin, D. E. Browne, J. Fitzsimons, and J. J. L. Morton, "Brokered graph-state quantum computation", New J. Phys. **8**, 141 (2006).

[86] G. Balasubramanian, P. Neumann, D. J. Twitchen, M. L. Markham, R. Kolesov, N. Mizuochi, J. Isoya, J. Achard, J. Beck, J. Tissler, V. Jacques, P. R. Hemmer, F. Jelezko, and J. Wrachtrup, "Ultralong spin coherence time in isotopically engineered diamond", Nat. Mater. **8**, 383 (2009).

[87] T. Ishikawa, K.-M. C. Fu, C. Santori, V. M. Acosta, R. G. Beausoleil, H. Watanabe, S. Shikata, and K. M. Itoh, "Optical and Spin Coherence Properties of Nitrogen-Vacancy Centers Placed in a 100 nm Thick Isotopically Purified Diamond Layer", Nano Lett. **12**, 2083–2087 (2012).

[88] G. de Lange, Z. H. Wang, D. Ristè, V. V. Dobrovitski, and R. Hanson, "Universal dynamical decoupling of a single solid-state spin from a spin bath", Science **330**, 60 (2010).

[89] N. Bar-Gill, L. M. Pham, A. Jarmola, D. Budker, and R. L. Walsworth, "Solid-state electronic spin coherence time approaching one second.", Nat. Commun. **4**, 1743 (2013).

[90] W. Pfaff, T. H. Taminiau, L. Robledo, H. Bernien, M. L. Markham, D. J. Twitchen, and R. Hanson, "Demonstration of entanglement-by-measurement of solid-state qubits", Nat. Phys. **9**, 29–33 (2012).

[91] W. Pfaff, B. J. Hensen, H. Bernien, S. B. van Dam, M. S. Blok, T. H. Taminiau, M. J. Tiggelman, R. N. Schouten, M. L. Markham, D. J. Twitchen, and R. Hanson, "Quantum information. Unconditional quan-

tum teleportation between distant solid-state quantum bits.", Science **345**, 532 (2014).

[92] H. Bernien, B. J. Hensen, W. Pfaff, G. Koolstra, M. S. Blok, L. Robledo, T. H. Taminiau, M. L. Markham, D. J. Twitchen, L. Childress, and R. Hanson, "Heralded entanglement between solid-state qubits separated by three metres", Nature **497**, 86–90 (2013).

[93] S. Yang, Y. Wang, D. D. Rao, T. H. Tran, A. S. Momenzadeh, M. L. Markham, D. J. Twitchen, P. Wang, W. Yang, R. Stöhr, P. Neumann, H. Kosaka, and J. Wrachtrup, "High-fidelity transfer and storage of photon states in a single nuclear spin", Nat. Photonics **10**, 507–511 (2016).

[94] B. Grotz, M. V. Hauf, M. Dankerl, B. Naydenov, S. Pezzagna, J. Meijer, F. Jelezko, J. Wrachtrup, M. Stutzmann, F. Reinhard, and J. A. Garrido, "Charge state manipulation of qubits in diamond", Nat. Commun. **3**, 729 (2012).

[95] W. Gerlach and O. Stern, "Der experimentelle Nachweis der Richtungsquantelung im Magnetfeld", Zeitschrift für Phys. **9**, 349–352 (1922).

[96] G. Breit and I. I. Rabi, "Measurement of Nuclear Spin", Phys. Rev. **38**, 2082–2083 (1931).

[97] I. I. Rabi, J. R. Zacharias, S. Millman, and P. Kusch, "A New Method of Measuring Nuclear Magnetic Moment", Phys. Rev. **53**, 318–318 (1938).

[98] E. Zavoisky, "Paramagnetic Relaxation of Liquid Solutions for Perpendicular Fields", J. Phys U.S.S.R **9**, 211–245 (1945).

[99] J. Frenkel, "On the Theory of Relaxation Losses, Connected with Magnetic Resonance in Solid Bodies", J. Phys U.S.S.R **9**, 299–304 (1945).

[100] R. L. Cummerow and D. Halliday, “Paramagnetic Losses in Two Manganous Salts”, Phys. Rev. **70**, 433–433 (1946).

[101] D. M. S. Badduley and J. H. E. Griffiths, “Paramagnetic Resonance and Magnetic Energy Levels in Chrome Alum”, Nature **160**, 532–533 (1947).

[102] A. Schweiger and G. Jeschke, *Principles of Pulse Electron Paramagnetic Resonance. Oxford University Press* (2001), p. 578.

[103] S. Stoll and A. Schweiger, “EasySpin, a comprehensive software package for spectral simulation and analysis in EPR”, J. Magn. Reson. **178**, 42–55 (2006).

[104] R. S. Mulliken, “Report on notation for the spectra of polyatomic molecules”, J. Chem. Phys. **23**, 1997–2011 (1955).

[105] R. Shankar, *Principles of Quantum Mechanics* (Springer, 1994).

[106] C. A. Ryan, J. S. Hodges, and D. G. Cory, “Robust decoupling techniques to extend quantum coherence in diamond”, Phys. Rev. Lett. **105**, 200402 (2010).

[107] J. M. Boss, K. S. Cujia, J. Zopes, and C. L. Degen, “Quantum sensing with arbitrary frequency resolution”, Science **356**, 837–840 (2017).

[108] H. S. Knowles, D. M. Kara, and M. Atatüre, “Observing bulk diamond spin coherence in high-purity nanodiamonds”, Nat. Mater. **13**, 21–25 (2014).

[109] V. M. Acosta, D. Budker, P. R. Hemmer, J. R. Maze, and R. L. Walsworth, “Optical magnetometry with nitrogen-vacancy centers in diamond”, PhD thesis (2011), p. 142.

[110] L. Rondin, J. P. Tetienne, T. Hingant, J. F. Roch, P. Maletinsky, and V. Jacques, “Magnetometry with nitrogen-vacancy defects in diamond”, Reports Prog. Phys. **77**, 056503 (2014).

[111] D. Le Sage, K. Arai, D. R. Glenn, S. J. DeVience, L. M. Pham, L. Rahn-Lee, M. D. Lukin, A. Yacoby, A. Komeili, and R. L. Walsworth, “Optical magnetic imaging of living cells”, Nature **496**, 486–489 (2014).

[112] I. Gross, W. Akhtar, V. Garcia, L. J. Martínez, S. Chouaieb, K. Garcia, C. Carrétéro, A. Barthélémy, P. Appel, P. Maletinsky, J. V. Kim, J. Y. Chauleau, N. Jaouen, M. Viret, M. Bibes, S. Fusil, and V. Jacques, “Real-space imaging of non-collinear antiferromagnetic order with a single-spin magnetometer”, Nature **549**, 252–256 (2017).

[113] P. Appel, E. Neu, M. Ganzhorn, A. Barfuss, M. Batzer, M. Gratz, A. Tschöpe, and P. Maletinsky, “Fabrication of all diamond scanning probes for nanoscale magnetometry”, Rev. Sci. Instrum. **87**, 063703 (2016).

[114] S. Lagomarsino, M. Bellini, C. Corsi, S. Fanetti, F. Gorelli, I. Liontos, G. Parrini, M. Santoro, and S. Sciortino, “Electrical and Raman-imaging characterization of laser-made electrodes for 3D diamond detectors”, Diam. Relat. Mater. **43**, 23–28 (2014).

[115] S. A. Murphy, M. J. Booth, L. Li, A. Oh, P. S. Salter, B. Sun, D. Whitehead, and A. Zadoroshnyj, “Laser processing in 3D diamond detectors”, Nucl. Instruments Methods Phys. Res. Sect. A Accel. Spectrometers, Detect. Assoc. Equip. **845**, 136–138 (2017).

[116] A. Courvoisier, M. J. Booth, and P. S. Salter, “Inscription of 3D waveguides in diamond using an ultrafast laser”, Appl. Phys. Lett. **109**, 031109 (2016).

[117] L. Huang, P. S. Salter, F. Payne, and M. J. Booth, "Aberration correction for direct laser written waveguides in a transverse geometry", Opt. Express **24**, 10565 (2016).

[118] B. Naydenov, V. Richter, J. Beck, M. Steiner, P. Neumann, G. Balasubramanian, J. Achard, F. Jelezko, J. Wrachtrup, and R. Kalish, "Enhanced generation of single optically active spins in diamond by ion implantation", Appl. Phys. Lett. **96**, 163108 (2010).

[119] T. Staudacher, F. Ziem, L. Häussler, R. Stöhr, S. Steinert, F. Reinhard, J. Scharpf, A. Denisenko, and J. Wrachtrup, "Enhancing the spin properties of shallow implanted nitrogen vacancy centers in diamond by epitaxial overgrowth", Appl. Phys. Lett. **101**, 212401 (2012).

[120] J. Meijer, B. Burchard, M. Domhan, C. Wittmann, T. Gaebel, I. Popa, F. Jelezko, and J. Wrachtrup, "Generation of single color centers by focused nitrogen implantation", Appl. Phys. Lett. **87**, 261909 (2005).

[121] M. Lesik, P. Spinicelli, S. Pezzagna, P. Happel, V. Jacques, O. Salord, B. Rasser, A. Delobbe, P. Sudraud, A. Tallaire, J. Meijer, and J. F. Roch, "Maskless and targeted creation of arrays of colour centres in diamond using focused ion beam technology", Phys. Status Solidi Appl. Mater. Sci. **210**, 2055–2059 (2013).

[122] S. Pezzagna, B. Naydenov, F. Jelezko, J. Wrachtrup, and J. Meijer, "Creation efficiency of nitrogen-vacancy centres in diamond", New J. Phys. **12**, 065017 (2010).

[123] P. Spinicelli, A. Dréau, L. Rondin, F. Silva, J. Achard, S. Xavier, S. Bansropun, T. Debuisschert, S. Pezzagna, J. Meijer, V. Jacques, and J. F. Roch, "Engineered arrays of nitrogen-vacancy color centers in di-

amond based on implantation of cn Molecules through nanoapertures", New J. Phys. **13**, 025014 (2011).

[124] S. Sangtawesin, T. O. Brundage, Z. J. Atkins, and J. R. Petta, "Highly tunable formation of nitrogen-vacancy centers via ion implantation", Appl. Phys. Lett. **105**, 063107 (2014).

[125] S. Pezzagna, D. Wildanger, P. Mazarov, A. D. Wieck, Y. Sarov, I. Rangelow, B. Naydenov, F. Jelezko, S. W. Hell, and J. Meijer, "Nanoscale engineering and optical addressing of single spins in diamond", Small **6**, 2117–2121 (2010).

[126] K. Ohno, F. Joseph Heremans, L. C. Bassett, B. A. Myers, D. M. Toyli, A. C. Bleszynski Jayich, C. J. Palmstrøm, and D. D. Awschalom, "Engineering shallow spins in diamond with nitrogen delta-doping", Appl. Phys. Lett. **101**, 082413 (2012).

[127] K. Ohno, F. Joseph Heremans, C. F. De Las Casas, B. A. Myers, B. J. Alemán, A. C. Bleszynski Jayich, and D. D. Awschalom, "Three-dimensional localization of spins in diamond using ^{12}C implantation", Appl. Phys. Lett. **105**, 052406 (2014).

[128] D. Scarabelli, M. E. Trusheim, O. Gaathon, D. Englund, and S. J. Wind, "Nanoscale Engineering of Closely-Spaced Electronic Spins in Diamond", Nano Lett. **16**, 4982–4990 (2016).

[129] T. Yamamoto, C. Müller, L. P. McGuinness, T. Teraji, B. Naydenov, S. Onoda, T. Ohshima, J. Wrachtrup, F. Jelezko, and J. Isoya, "Strongly coupled diamond spin qubits by molecular nitrogen implantation", Phys. Rev. B **88**, 201201 (2013).

[130] D. M. Toyli, C. D. Weis, G. D. Fuchs, T. Schenkel, and D. D. Awschalom, “Chip-scale nanofabrication of single spins and spin arrays in diamond”, Nano Lett. **10**, 3168–3172 (2010).

[131] K. Ohashi, T. Rosskopf, H. Watanabe, M. Loretz, Y. Tao, R. Hauert, S. Tomizawa, T. Ishikawa, J. Ishi-Hayase, S. Shikata, C. L. Degen, and K. M. Itoh, “Negatively charged nitrogen-vacancy centers in a 5 nm Thin ^{12}C diamond film”, Nano Lett. **13**, 4733–4738 (2013).

[132] M. Chandran, S. Michaelson, C. Saguy, and A. Hoffman, “Fabrication of a nanometer thick nitrogen delta doped layer at the sub-surface region of (100) diamond”, Appl. Phys. Lett. **109**, 221602 (2016).

[133] C. A. McLellan, B. A. Myers, S. Kraemer, K. Ohno, D. D. Awschalom, and A. C. Bleszynski Jayich, “Patterned Formation of Highly Coherent Nitrogen-Vacancy Centers Using a Focused Electron Irradiation Technique”, Nano Lett. **16**, 2450–2454 (2016).

[134] D. Antonov, T. Häußermann, A. Aird, J. Roth, H.-R. Trebin, C. Müller, F. Jelezko, T. Yamamoto, J. Isoya, S. Pezzagna, J. Meijer, J. Wrachtrup, L. P. McGuinness, F. Jelezko, T. Yamamoto, J. Isoya, S. Pezzagna, J. Meijer, and J. Wrachtrup, “Statistical investigations on nitrogen-vacancy centre creation”, Appl. Phys. Lett. **104**, 012105 (2014).

[135] J. Schwartz, S. Aloni, D. F. Ogletree, and T. Schenkel, “Effects of low-energy electron irradiation on formation of nitrogen-vacancy centers in single-crystal diamond”, New J. Phys. **14**, 043024 (2012).

[136] S. Becker, N. Raatz, S. Jankuhn, R. John, and J. Meijer, “Nitrogen implantation with a scanning electron microscope”, Sci. Rep. **8**, 32 (2018).

[137] R. Fukuda, P. Balasubramanian, I. Higashimata, G. Koike, T. Okada, R. Kagami, T. Teraji, S. Onoda, M. Haruyama, K. Yamada, M. Inaba,

H. Yamano, F. M. Stürner, S. Schmitt, L. P. McGuinness, F. Jelezko, T. Ohshima, T. Shinada, H. Kawarada, W. Kada, O. Hanaizumi, T. Tanii, and J. Isoya, “Lithographically engineered shallow nitrogen-vacancy centers in diamond for external nuclear spin sensing”, New J. Phys. **20**, 083029 (2018).

[138] M. Schukraft, J. Zheng, T. Schröder, S. L. Mouradian, M. Walsh, M. E. Trusheim, H. Bakhru, and D. Englund, “Invited Article: Precision nanoimplantation of nitrogen vacancy centers into diamond photonic crystal cavities and waveguides”, APL Photonics **1**, 020801 (2016).

[139] A. Ródenas, M. Gu, G. Corrielli, P. Paiè, S. John, A. K. Kar, and R. Osellame, “Three-dimensional femtosecond laser nanolithography of crystals”, Nat. Photonics **13**, 105–109 (2019).

[140] B. Sotillo, V. Bharadwaj, T. T. Fernandez, M. Ramos, J. P. Hadden, A. Chiappini, M. Ferrari, R. Osellame, G. Galzerano, P. E. Barclay, R. Ramponi, P. S. Salter, and S. M. Eaton, “Femtosecond laser written diamond photonics”, Adv. photonics 2018, edited by OSA (July 2018).

[141] J. P. Hadden, V. Bharadwaj, B. Sotillo, S. Rampini, R. Osellame, J. D. Witmer, H. Jayakumar, T. T. Fernandez, A. Chiappini, C. Armellini, M. Ferrari, R. Ramponi, P. E. Barclay, and S. M. Eaton, “Integrated waveguides and deterministically positioned nitrogen vacancy centers in diamond created by femtosecond laser writing”, Opt. Lett. **43**, 3586 (2018).

[142] M. V. Hauf, B. Grotz, B. Naydenov, M. Dankerl, S. Pezzagna, J. Meijer, F. Jelezko, J. Wrachtrup, M. Stutzmann, F. Reinhard, and J. A. Garrido, “Chemical control of the charge state of nitrogen-vacancy centers in diamond”, Phys. Rev. B **83**, 081304 (2011).

[143] C. Schreyvogel, V. Polyakov, R. Wunderlich, J. Meijer, and C. E. Nebel, "Active charge state control of single NV centres in diamond by in-plane Al-Schottky junctions", Sci. Rep. **5**, 12160 (2015).

[144] M. Pfender, N. Aslam, P. Simon, D. Antonov, G. Thiering, S. Burk, F. Fávaro de Oliveira, A. Denisenko, H. Fedder, J. Meijer, J. A. Garrido, Á. Gali, T. Teraji, J. Isoya, M. W. Doherty, A. Alkauskas, A. Gallo, A. Grüneis, P. Neumann, and J. Wrachtrup, "Protecting a Diamond Quantum Memory by Charge State Control", Nano Lett. **17**, 5931–5937 (2017).

[145] M. Shimizu, T. Makino, T. Iwasaki, K. Tahara, H. Kato, N. Mizuochi, S. Yamasaki, and M. Hatano, "Charge-state control of ensemble of nitrogen vacancy centers by n-i-n diamond junctions", Appl. Phys. Express **11**, 033004 (2018).

[146] J. Forneris, S. Ditalia Tchernij, A. Tengattini, E. Enrico, V. Grilj, N. Skukan, G. Amato, L. Boarino, M. Jakšić, and P. Olivero, "Electrical control of deep NV centers in diamond by means of sub-superficial graphitic micro-electrodes", Carbon **113**, 76–86 (2017).

[147] T. M. Babinec, B. J. M. Hausmann, M. Khan, Y. Zhang, J. R. Maze, P. R. Hemmer, and M. Lončar, "A diamond nanowire single-photon source", Nat. Nanotechnol. **5**, 195–199 (2010).

[148] N. Mizuochi, T. Makino, H. Kato, D. Takeuchi, M. Ogura, H. Okushi, M. Nothaft, P. Neumann, Á. Gali, F. Jelezko, J. Wrachtrup, and S. Yamasaki, "Electrically driven single-photon source at room temperature in diamond", Nat. Photonics **6**, 299–303 (2012).

[149] C. C. Gerry and P. L. Knight, *Introductory quantum optics* (2005), p. 317.

[150] R. Hanbury Brown and R. Q. Twiss, “Correlation between photons in two coherent beams of light”, J. Astrophys. Astron. **15**, 13–19 (1994).

[151] L. Robledo, L. Childress, H. Bernien, B. Hensen, P. F. A. Alkemade, and R. Hanson, “High-fidelity projective read-out of a solid-state spin quantum register”, Nature **477**, 574–578 (2011).

[152] B. J. Hensen, H. Bernien, A. E. Dreaú, A. Reiserer, N. Kalb, M. S. Blok, J. Ruitenberg, R. F. L. Vermeulen, R. N. Schouten, C. Abellán, W. Amaya, V. Pruneri, M. W. Mitchell, M. L. Markham, D. J. Twitchen, D. Elkouss, S. Wehner, T. H. Taminiau, and R. Hanson, “Loophole-free Bell inequality violation using electron spins separated by 1.3 kilometres”, Nature **526**, 682–686 (2015).

[153] R. J. Glauber, “The quantum theory of optical coherence”, Phys. Rev. **130**, 2529–2539 (1963).

[154] M. Jamali, I. Gerhardt, M. Rezai, K. Frenner, H. Fedder, and J. Wrachtrup, “Microscopic diamond solid-immersion-lenses fabricated around single defect centers by focused ion beam milling”, Rev. Sci. Instrum. **85**, 123703 (2014).

[155] L. Li, T. Schröder, E. H. Chen, M. Walsh, I. Bayn, J. Goldstein, O. Gaathon, M. E. Trusheim, M. Lu, J. Mower, M. Cotlet, M. L. Markham, D. J. Twitchen, and D. Englund, “Coherent spin control of a nanocavity-enhanced qubit in diamond”, Nat. Commun. **6**, 6173 (2015).

[156] D. A. Hopper, H. Shulevitz, L. C. Bassett, D. A. Hopper, H. J. Shulevitz, and L. C. Bassett, “Spin Readout Techniques of the Nitrogen-Vacancy Center in Diamond”, Micromachines **9**, 437 (2018).

[157] G. Wachter, S. Kuhn, S. Minniberger, C. Salter, P. Asenbaum, J. Millen, M. Schneider, J. Schalko, U. Schmid, A. Felgner, D. Hüser, M. Arndt, and M. Trupke, "Silicon microcavity arrays with open access and a finesse of half a million", Light Sci. Appl. **8**, 37 (2019).

[158] J. P. Hadden, J. P. Harrison, A. C. Stanley-Clarke, L. Marseglia, Y. L. D. Ho, B. R. Patton, J. L. O'Brien, and J. G. Rarity, "Strongly enhanced photon collection from diamond defect centers under microfabricated integrated solid immersion lenses", Appl. Phys. Lett. **97**, 241901 (2010).

[159] G. W. Morley, *Electron Paramagnetic Resonance*, edited by V. Chechik, D. M. Murphy, and B. Gilbert, Vol. 24, Electron Paramagnetic Resonance (July 2014), p. 13.

[160] J. C. Forgues and C. Lupien, "Characterization of white LEDs at cryogenic (4K) temperatures", J. Low Temp. Phys. **166**, 101–106 (2012).

[161] N. Zhao, J. Wrachtrup, and R. B. Liu, "Dynamical decoupling design for identifying weakly coupled nuclear spins in a bath", Phys. Rev. A **90**, 032319 (2014).

[162] T. Staudacher, F. Shi, S. Pezzagna, J. Meijer, J. Du, C. A. Meriles, F. Reinhard, and J. Wrachtrup, "Nuclear magnetic resonance spectroscopy on a (5 nm)^3 sample volume.", Science **339**, 561 (2013).

[163] T. Staudacher, N. Raatz, S. Pezzagna, J. Meijer, F. Reinhard, C. A. Meriles, and J. Wrachtrup, "Probing molecular dynamics at the nanoscale via an individual paramagnetic centre", Nat. Commun. **6**, 8527 (2015).

[164] S. Schmitt, T. Gefen, F. M. Stürner, T. Unden, G. Wolff, C. Müller, J. Scheuer, B. Naydenov, M. L. Markham, S. Pezzagna, J. Meijer, I. Schwarz, M. B. Plenio, A. Retzker, L. P. McGuinness, and F. Jelezko,

"Submillihertz magnetic spectroscopy performed with a nanoscale quantum sensor", Science **837**, 832–837 (2017).

[165] J. M. Binder, A. Stark, N. Tomek, J. Scheuer, F. Frank, K. D. Jahnke, C. Müller, S. Schmitt, M. H. Metsch, T. Unden, T. Gehring, A. Huck, U. L. Andersen, L. J. Rogers, and F. Jelezko, "Qudi: A modular python suite for experiment control and data processing", SoftwareX **6**, 85–90 (2017).

[166] *The .NET framework*, 2018, `https://docs.microsoft.com/en-us/dotnet/framework/`.

[167] *The F♯ programming language*, 2018, `https://fsharp.org/`.

[168] *The Visual Studio IDE*, 2018, `https://visualstudio.microsoft.com/vs/`.

[169] *The WPF framework*, 2018, `https://docs.microsoft.com/en-us/dotnet/framework/wpf/`.

[170] *Reactive X asynchronous programming API*, 2018, `http://reactivex.io/`.

[171] *University of Warwick - Keysight N5172B driver*, 2018, `https://github.com/WarwickEPR/Endorphin.Instrument.Keysight.N5172B`.

[172] *University of Warwick - PicoScope drivers*, 2018, `https://github.com/WarwickEPR/Endorphin.Instrument.PicoScope`.

[173] *University of Warwick - Attocube ANC300 driver*, 2018, `https://github.com/WarwickEPR/Endorphin.Instrument.Attocube`.

[174] *University of Warwick - Endorphin.IO*, 2018, `https://github.com/WarwickEPR/Endorphin.IO`.

[175] *The Lua programming language*, 2019, `https://www.lua.org/`.

[176] *University of Warwick - FPGA photon counter instrument driver*, 2018, `https://github.com/WarwickEPR/Endorphin.Instrument.Warwick`.

[177] J. C. Simpson, J. E. Lane, C. D. Immer, and R. C. Youngquist, *Simple analytic expressions for the magnetic field of a circular current loop*, tech. rep. (NASA STI, 2001).

[178] R. N. Simons, *Coplanar Waveguide Circuits, Components, and Systems*, Wiley Series in Microwave and Optical Engineering (Mar. 2004).

[179] *Klayout*, 2019, `https://www.klayout.de/intro.html`.

[180] B. Sotillo, V. Bharadwaj, J. P. Hadden, M. Sakakura, A. Chiappini, T. T. Fernandez, S. Longhi, O. Jedrkiewicz, Y. Shimotsuma, L. Criante, R. Osellame, G. Galzerano, M. Ferrari, K. Miura, R. Ramponi, P. E. Barclay, and S. M. Eaton, "Diamond photonics platform enabled by femtosecond laser writing", Sci. Rep. **6**, 35566 (2016).

[181] V. V. Kononenko, I. I. Vlasov, E. V. Zavedeev, A. A. Khomich, and V. I. Konov, "Correlation between surface etching and NV centre generation in laser-irradiated diamond", Appl. Phys. A **124**, 226 (2018).

[182] C. L. Lee, E. Gu, M. D. Dawson, I. Friel, and G. A. Scarsbrook, "Etching and micro-optics fabrication in diamond using chlorine-based inductively-coupled plasma", Diam. Relat. Mater. **17**, 1292–1296 (2008).

[183] W. E. Moerner and D. P. Fromm, "Methods of single-molecule fluorescence spectroscopy and microscopy", Rev. Sci. Instrum. **74**, 3597–3619 (2003).

[184] E. Van Oort and M. Glasbeek, "Optically detected low field electron spin echo envelope modulations of fluorescent N-V centers in diamond", Chem. Phys. **143**, 131–140 (1990).

[185] J. Forneris, A. Battiato, D. Gatto Monticone, F. Picollo, G. Amato, L. Boarino, G. Brida, I. P. Degiovanni, E. Enrico, M. Genovese, E. Moreva, P. Traina, C. Verona, G. Verona Rinati, and P. Olivero, "Electroluminescence from a diamond device with ion-beam-micromachined buried graphitic electrodes", Nucl. Instruments Methods Phys. Res. Sect. B Beam Interact. with Mater. Atoms **348**, 187–190 (2015).

[186] S. J. Cobb, Z. J. Ayres, and J. V. Macpherson, "Boron Doped Diamond: A Designer Electrode Material for the Twenty-First Century", Annu. Rev. Anal. Chem. **11**, 463–484 (2018).

[187] J. V. Macpherson, "A practical guide to using boron doped diamond in electrochemical research", Phys. Chem. Chem. Phys. **17**, 2935–2949 (2015).

[188] V. Bharadwaj, O. Jedrkiewicz, J. P. Hadden, B. Sotillo, M. R. Vázquez, P. Dentella, T. T. Fernandez, A. Chiappini, A. N. Giakoumaki, T. Le Phu, M. Bollani, M. Ferrari, R. Ramponi, P. E. Barclay, and S. M. Eaton, "Femtosecond laser written photonic and microfluidic circuits in diamond", J. Phys. Photonics **1**, 022001 (2019).